THERMOPOWER AND MAGNETORESISTANCE STUDIES IN A TWO-DIMENSIONAL ELECTRON GAS

by

Jian Zhang

A dissertation submitted to the faculty of
The University of Utah
in partial fulfillment of the requirements for the degree of

Doctor of Philosophy

Department of Physics

The University of Utah

August 2004

THE UNIVERSITY OF UTAH GRADUATE SCHOOL

SUPERVISORY COMMITTEE APPROVAL

of a dissertation submitted by

Jian Zhang

This dissertation has been read by each member of the following supervisory committee and by majority vote has been found to be satisfactory.

_____	Chair: Rui-Rui Du
_____	Yong-Shi Wu
_____	John Worlock
_____	Alexei L. Efros
_____	Mark Miller

FINAL READING APPROVAL

ABSTRACT

An experimental study for thermo-electric power (TEP) in a two-dimensional (2D) electron gas at low temperatures (T) has been completed. At zero magnetic field (B) and at $T > 300$ mK, the TEP of high-mobility samples has shown a temperature dependence in the form of a power law (T^{3-4}), which indicates that the phonon-drag TEP is dominant and the diffusive TEP is negligible. Under this condition, TEP measurement can be applied to directly investigate electron-phonon interaction because impurity scattering is not directly relevant. In a small magnetic field ($B < 0.3$ T) and at $T < 1$ K, a new type of TEP oscillations has been observed. These oscillations result from the inter-Landau-Level (LL) resonance of electrons by acoustic phonons carrying a momentum equal to twice the Fermi wave number (k_F) at $B = 0$. For the first time, the inter-LL scattering is observed in TEP measurement. Numerical calculations show that both three-dimensional (3D) and two-dimensional (2D) interface phonons can contribute to this effect.

The TEP in the lowest LL has shown remarkable structure at fractional LL filling factors $\nu = 2/3$ and 3/5. At both 2/3 and 3/5, the TEP evolve from a steep minimum at low T into a strong maximum at high T. Between 300 mK and 1.5 K the TEP at these filling factors are thermally activated.

Besides TEP measurement, magnetoresistance (MR) measurement is employed to study one-half state ($\nu = 1/2$) at low temperatures (down to 50 mK) and ultrahigh magnetic fields (up to 42 T) in a square quantum well sample. Diagonal resistance (R_{xx}) exhibits a sharp, strongly temperature-dependent minimum centered at $\nu = 1/2$, whereas concomitant Hall resistance (R_{xy}) does not develop into quantized plateau. The first derivative of Hall resistance with respect to magnetic field shows a sharp temperature-dependent minimum at $\nu = 1/2$. These

data deviate significantly from the characteristic transport features of composite Fermions (CFs) in single heterojunction samples.

To my Mom and my Dad

CONTENTS

LIST OF FIGURES

LIST OF TABLES

ACKNOWLEDGMENTS

CHAPTER 1

INTRODUCTION

A two-dimensional electron gas, when subject to an intense perpendicular magnetic field and low temperature, has exhibited a multitude of new phenomena and novel effects, discovered during the last 24 years. In 1980, the integer quantum Hall effect (IQHE) was discovered by Klause Von Klitzing in a 2DEG in Silicon MOSFETs [1]. In the 2DEG in GaAs-AlGaAs heterostructures, D. C. Tsui and H. Stormer soon discovered in 1982 that Hall resistance was also quantized at fractional LL filling factor of $\nu = 1/3$ [2]. A series of fractional quantized states have been observed at rational filling factors with the odd-denominators, such as 2/3, 3/5, ..., and 2/5, 3/7, ..., etc. Later on, Laughlin's theory [3] gave an excellent explanation for those fractional quantized states. A question arose: is it possible that those quantized states also occur at the fractional filling factors with even-denominators? Fractional quantum Hall Effect (FQHE) state at $\nu = 5/2$ was first observed by R. L. Willet *et al.* [4]. A FQHE state $\nu = 1/2$ was also observed in a double quantum well [5] and in a wide single quantum well (70 nm) with double-layers characteristics [6]. Beyond Laughlin's theory, these FQHE states at 5/2 and 1/2 were explained by considering extra freedom of electrons, such as spin and layer index (psuedo-spin) [7, 8, 9]. In the composite Fermion (CF) picture [10, 11, 12, 13], and without considering extra degrees of freedom, Moore and Read proposed that 5/2 FQHE state was a ground state of p-wave paired CFs [14]. In the composite Fermion model, at one-half filling factor, CFs experience effective zero magnetic field and have a well defined Fermi surface [15]. At very low temperature, it is possible that CFs at $\nu = 5/2$ be paired to form a lower energy state. Then an energy gap appears and FQHE at 5/2 is developed. Furthermore, Park *et al.* suggested

[16] that even at one-half filling factor, if the ratio of 2DEG thickness to magnetic length is greater than 5, CFs could form a p-wave pair and one-half FQHE state would appear in single layer and spin-polarized 2DEG, since the Coulomb repulsive interaction would be greatly softened. So far, without extra degrees of freedom, no one-half FQHE state was observed. Experimentally, it is interesting to study the one-half state in a new regime — a single wide quantum well (30-40 nm) with a single layer in a ultra high magnetic field (30T - 42T).

The beginning of this thesis work is focused on the MR measurement of one-half state in a thick, single quantum well. It is shown that ρ_{xx} of the sample exhibits a sharp, strong temperature-dependent minimum centered at $\nu = 1/2$, while concomitant ρ_{xy} does not develop into quantized plateau. The first derivative of Hall resistance with respect to magnetic field shows sharp temperature-dependent minimum at $\nu = 1/2$. These data deviate significantly from the characteristic transport features of composite Fermions in single heterojunction samples.

Besides the conventional MR measurement, a TEP measurement setup has been developed to detect the one-half state in the new experimental regime. The diffusive TEP directly measures the density of states (DOS) of electrons. Therefore it is useful to detect any change of DOS at one-half state in a new experimental regime. It is shown that phonon-drag TEP is dominant, and diffusive TEP is negligible in temperature range ($T > 300$ mK). Phonon-drag TEP is a powerful tool to detect the electron-phonon interaction at low temperature, since impurity scattering effect (dominant at low temperatures in a high-mobility 2DEG) is cancelled in phonon-drag TEP measurement. Extensive experimental study on the phonon-drag TEP has been performed in both low and high magnetic field.

A new type of low-field ($B < 0.3$ T) oscillations in TEP at low temperatures has been observed. These oscillations result from the inter-LL resonance of acoustic phonons carrying a momentum equal to twice the Fermi wave number (k_F) at $B = 0$. For the first time, the inter-LL scattering is observed in TEP measurement. Numerical calculations show that both three-dimensional (3D) and two-dimensional (2D) interface phonons can contribute to this effect.

In a high magnetic field (Lowest LL regime), two abnormal peaks are observed in TEP measurement in a temperature range (1 K-2 K) at $\nu = 2/3, 3/5$, while at lower temperature there are dip features at these fractional filling factors, indicating incompressible quantum liquid states at $\nu = 2/3, 3/5$. The TEP at $\nu = 2/3, 3/5$ show activation behavior in the temperature range of 250 mK - 1.6 K. The underlying physics for this new phenomenon is a subject for future experimental and theoretical work.

The thesis is organized as follows:

In Chapter 1, motivation and contents of thesis work are given. Thesis work is divided into three parts: MR study at one-half state ($\nu = 1/2$) in an ultrahigh magnetic field; TEP study at low and high magnetic fields.

In Chapter 2, general transport properties of 2DEG in a magnetic field at low temperature are reviewed.

In Chapter 3, results of TEP measurement in a low magnetic field are presented.

In Chapter 4, TEP data in a high magnetic filed are presented and discussed.

In Chapter 5, MR measurement of one-half state is presented.

Conclusions are given at the end.

CHAPTER 2

TRANSPORT PROPERTIES OF 2DEG

2.1 2DEG in *GaAs-AlGaAs* a heterostructure

A 2DEG can be realized in many different systems. Electrons can be trapped on
the surface of liquid helium by an external field and an image potential. Electrons
move freely along the surface but cannot get away or into the surface, thereby
forming an almost ideal 2DEG . The density of 2DEG (n_e) in this system is rather
low ($10^5 - 10^9 \mathrm{cm}^{-2}$), and 2DEG behaves classically. A 2DEG can also be realized
in a Si-MOSFET (Metal-Oxide-Semiconductor-Field-Effect-Transistor), in which
the IQHE was discovered. Under large enough negative gate voltage, the bottom
of conduction band of p-Si can be bent down below the Fermi energy (E_F) level.
Electrons are then accumulated in the inversion layer of p-Si and trapped in the
quasi-triangle potential well along the perpendicular direction. Electron motion
perpendicular to the interface between SiO_2 and p-type Si is quantized and confined,
but it is still free to move along the interface. n_e in a Si-MOSFET system can be
varied easily from $0 - 10^{13} cm^{-2}$. Since the fabrication of Si-MOSFET involves
several processes (Si crystal growth, SiO_2 chemical deposition, and metal thermal
deposition or ions sputtering), the mobility of 2DEG is not very high compared
with another typical 2DEG system: GaAs-$Al_x Ga_{1-x}$ heterojunction, which can be
fabricated in single process-MBE (Molecular-Beam Epitaxy) crystal growth. Since
the discovery of the FQHE in GaAs-$Al_x Ga_{1-x}$ heterojunction, the mobility (μ) of
2DEG has been pushed up to 30×10^6 cm^2/Vs from 10^5 cm^2/Vs. A host of new
phenomena and novel physics have been discovered and studied using primarily the

GaAs-Al$_x$Ga$_{1-x}$As heterojunction. All samples in this thesis work come from this system.

The GaAs crystal is composed of two sublattices, each a face centered cubic (fcc) lattice with an offset of one-quarter of the diagonal length along the diagonal direction. This crystal configuration is known as cubic sphalerite or zinc blende. Table 2.1 provides a list of relevant parameters for it [17].

Al atoms supplant some Ga atoms of GaAs, and Al$_{0.3}$Ga$_{0.7}$As crystal can be obtained. Al$_{0.3}$Ga$_{0.7}$As crystal has the same structure and a band diagram similar to GaAs crystal. The lattice constant of Al$_{0.3}$Ga$_{0.7}$As crystal can be calculated by Vegard's law[17]: $0.3 \times 0.5660 + 0.7 \times 0.5653 = 0.5655$ nm, which has a negligible mismatch with the lattice constant (0.5653 nm) of GaAs. This feature makes it possible for Al$_{0.3}$Ga$_{0.7}$As crystal to grow on GaAs without significant stress. The interface between them is almost ideal. Al$_{0.3}$Ga$_{0.7}$As crystal still has a direct gap and the gap energy is 1.80 eV at $T = 300$ K, higher than 1.42 eV (at $T = 300$ K) of GaAs energy gap. $\Delta E_C = 0.33$ eV is derived according to Anderson's rule [17] from the difference of electron affinity χ. This discontinuity at the bottom of conduction band makes confinement of 2DEG possible at the interface. Electrons come from doping. In order to reduce impurity-scattering, modulation doping technique is employed. Si doping (only several atom layers) is isolated from the interface by the spacer Al$_{0.3}$Ga$_{0.7}$As. Electrons migrate from dopant and across the spacer to GaAs, which has lower energy of the conduction band. The migrated electrons bend the conduction band to form a quasi-triangle potential well due to the electric field produced by these electrons. This triangle potential well confines electron motion in the direction perpendicular to the interface; however 2DEG are free to move along the interface on the GaAs side.

Molecular-Beam Epitaxy (MBE) technique is employed to fabricate the GaAs-Al$_{0.3}$Ga$_{0.7}$As heterojunction. MBE grows crystal layer by layer. MBE can produce very high quality samples with designed structures. Two of the samples (EA100 and EA 467) are fabricated by MBE in the Sandia National Lab. EA100 is a

single heterojunction and EA467 is a quantum well sample, which is equivalent to a double-heterojunction.

The energy quantization in a triangle potential can be understood by quantum mechanics. In a typical heterojunction, the energy difference between the first and second subband is around 200 K. The extension perpendicular to the interface is usually about 10 nm. At low temperature ($< 10K$), all trapped electrons will be frozen into the first subband but free to move in the plane of the GaAs layer. The dynamics of the electrons is therefore effectively 2D, in spite of their finite extension perpendicular to the plane.

Figure 2.1 shows the structure of GaAs-Al$_{0.3}$Ga$_{0.7}$As heterojunction and the band diagram.

DOS of 2DEG is a constant: $m^*/\pi\hbar^2$. The Fermi wave vector (k_F) and the Fermi energy (ε_F) can be obtained as follows:

$$k_F = \sqrt{2\pi n_e} \quad , \tag{2.1}$$

$$\varepsilon_F = \frac{\hbar^2 k_F^2}{2m^*} \quad . \tag{2.2}$$

EA100 has an electron density of 1.3×10^{11}cm^{-2} and a mobility of 3×10^6 cm^2/Vs; EA467 has density of 3.3×10^{11}cm^{-2} and mobility of 3×10^6 cm^2/Vs. Since a density of 1×10^{11}cm^{-2} is equivalent to 40 K in energy, the Fermi energy is as high as 132 K for EA467. That is why the second subband is occupied for EA467 sample. There are two ways to change the density of 2DEG: illumination by LED and application of gate voltage at low temperatures.

2.2 Classical transport in 2DEG

Basically 2D electrons in the GaAs crystal are quantum waves that consist of a confined wave along the z direction and an extended Bloch wave along the xy plane. It is possible to construct a wave packet with lots of Bloch waves having

Table 2.1. Parameters of GaAs and AlGaAs

Parameter	GaAs	$Al_{0.3}Ga_{0.7}As$
a	0.5653 nm	0.5655 nm
E_g at 300 K	1.42 eV	1.80 eV
E_g at 0 K	1.52 eV	-
E_g minimum	Γ	Γ
χ	4.07 eV	3.74 eV
m^*	0.067	0.092
m_{lh}	0.082	0.103
m_{hh}	0.5	0.5
ϵ_b	13.18	12.24
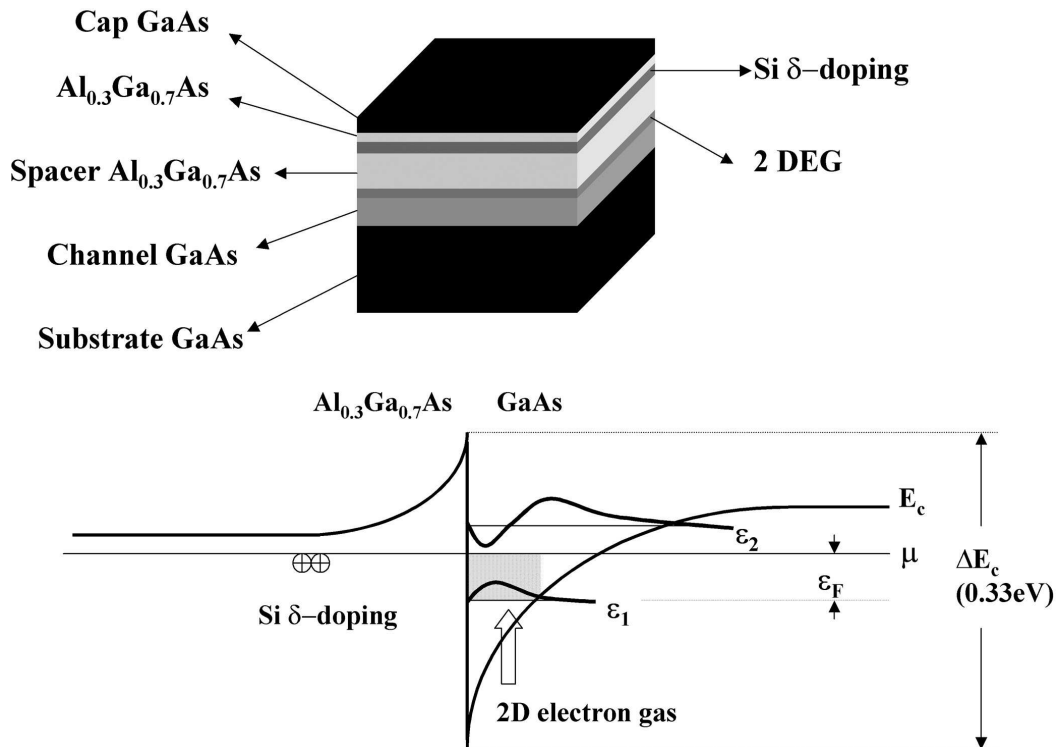
Figure 2.1. The layer structure and band diagram of GaAs-$Al_{0.3}Ga_{0.7}As$

different k-wave vectors. If the mean free path (l) is much larger than the size of the wave packet, *i.e.*,

$$l \times k_F >> 1 \quad , \tag{2.3}$$

this wave packet can be considered as a quasi-particle with defined position (the center of the wave packet), momentum (mean momentum - also called lattice momentum $\hbar k$), and effective mass m^* (different from the free electron bare mass m_0). Later it will be called a quasi-particle electron with effective mass and lattice momentum. This quasi-particle can move freely in the xy plane and can be treated as a classical particle.

Classical transport problems are handled by the Drude model, relaxation time (τ) approximation, and a classical nonequilibrium Boltzmann distribution equation. The Boltzmann equation considers the statistic distribution nature of electrons and phonons and has the same physics background as the Drude model in all other aspects. Under a weak external electric field (E), equation of motion in steady state is:

$$-eE = \frac{m^* V_d}{\tau} \quad ; \qquad \mu \equiv -\frac{V_d}{E} = \frac{e\tau}{m^*} \quad , \tag{2.4}$$

V_d is the drift velocity, which contributes to the electric current ($j = -n_e e V_d$). The Drude formula for resistivity and conductivity can be expressed as follows:

$$\sigma_0 = \frac{n_e e^2 \tau}{m^*} = n_e e \mu \quad , \tag{2.5}$$

$$\rho_0 = \frac{1}{\sigma_0} \quad . \tag{2.6}$$

In the presence of a static magnetic field (B), equation of motion is:

$$\frac{m^*V_d}{\tau} = -eE - eV_d \times B \quad . \tag{2.7}$$

We have assumed that electrons are confined to the xy plane and the magnetic field is applied along the z direction. Then the resistivity tensor can be written as follows:

$$\widehat{\rho} = \begin{pmatrix} \rho_0 & B/n_e e \\ -B/n_e e & \rho_0 \end{pmatrix} \quad . \tag{2.8}$$

Conductivity tensor $\widehat{\sigma}$ is a matrix inverse of $\widehat{\rho}$:

$$\widehat{\sigma} = \widehat{\rho}^{-1} = \begin{pmatrix} \sigma_{xx} & \sigma_{xy} \\ \sigma_{yx} & \sigma_{yy} \end{pmatrix} \quad , \tag{2.9}$$

where

$$\sigma_{xx} = \sigma_{yy} = \frac{\sigma_0}{1 + \omega_c^2 \tau^2} \quad ; \qquad \sigma_{xy} = -\sigma_{yx} = \frac{\sigma_0 \omega_c \tau}{1 + \omega_c^2 \tau^2} \quad . \tag{2.10}$$

Here ω_c is the angular frequency of cyclotron motion. In this classical case, Hall resistivity is just a straight line, and the diagonal resistivity is a constant when sweeping the magnetic field. The situation will be completely different when the cyclotron motion is quantized in a magnetic field. For example, ρ_{xx} will then oscillate with the magnetic field, an effect which is called Shubnikov-de Haas (SdH) oscillation.

2.3   Landau quantization in a magnetic field

Electron cyclotron motion will be quantized in a magnetic field. This problem can be exactly solved by the Schrödinger equation. Before dealing with Hamiltonian, a gauge needs to be chosen for the vector potential (A). The Landau gauge is a convenient one:

$$A_x = 0 \quad , \qquad A_y = xB \quad , \tag{2.11}$$

which satisfies $\nabla \times A = B$, with B along the z direction. The Hamiltonian can be written as:

$$H = \frac{1}{2m^*}(p_x^2 + (p_y + eBx)^2) \quad . \tag{2.12}$$

Because vector potential is only concerned with the variable x, the Hamiltonian has a translation symmetry in the y direction; electrons move freely along the y direction and have plane wave solution. The total wave function can be written as:

$$\psi_k(x, y) = e^{iky} f_k(x) \quad , \tag{2.13}$$

with the eigenvalue of momentum in the y direction being $-\hbar k$. After separating variables in the Schrödinger equation, a 1D energy eigen equation can be obtained as follows:

$$(\frac{1}{2m^*}p_x^2 + \frac{1}{2m^*}\omega_c^2(x + kl_B^2)^2)f_k(x) = \varepsilon_k f_k(x) \quad . \tag{2.14}$$

This is simply a 1D displaced harmonic oscillator with energy eigenvalues:

$$\varepsilon_{kn} = \hbar\omega_c \left(n + \frac{1}{2}\right) \quad , \tag{2.15}$$

and eigen wave functions:

$$f_{kn}(x) = H_n(x + kl_B^2)e^{-\frac{1}{2l_B^2}(x+kl_B^2)^2} \quad , \tag{2.16}$$

here H_n is the nth Hermite polynomial. The harmonic oscillator center is shifted to $-kl_B^2$, with l_B the magnetic length, which is defined as:

$$l_B = \sqrt{\frac{\hbar}{eB}} = 25.7nm/\sqrt{B(tesla)} \quad . \tag{2.17}$$

The solution tells us that electrons move freely in the y direction and have harmonic oscillation in x direction. The extension along the x direction is finite, which determines the maximum size of orbit as $\sqrt{2n+1}l_B$. The center of each harmonic oscillation depends on the wave vector k along the y direction.

When considering electron spin, each energy level is split into two by Zeeman energy, so the total energy is:

$$\varepsilon_{kn,\uparrow\downarrow} = \hbar\omega_c\left(n + \frac{1}{2}\right) \mp \frac{1}{2}\mu_B gB = ((n + \frac{1}{2})20K \mp \frac{1}{2}0.3K)/tesla \quad . \tag{2.18}$$

The most important fact here is that the eigen energy (ε_{kn}) does not depend on k, which means kinetic energy is quenched. These harmonic oscillator energy levels are called Landau levels (LLs), which are highly degenerate with k. The degeneracy of each Landau level, taking into account of spin split, is written as:

$$n_B = \frac{1}{2\pi l_B^2} = \frac{eB}{h} = \frac{B}{\Phi_0} \quad , \tag{2.19}$$

Φ_0 is the flux quanta. Filling factor (ν) is defined as:

$$\nu = \frac{n_e}{n_B} \quad . \tag{2.20}$$

n and ν are different due to spin degeneracy. The constant and continuous DOS

of 2DEG is quantized into a series of discrete δ functions. Taking into account temperature effect and scattering mechanism, LL will be expanded, and DOS at each LL has a Gaussian distribution form with a full-width Γ at half-height, which is shown in Figure 2.2.

When sweeping the magnetic field, ε_F passes alternatively the maximum and the minimum of DOS, giving rise an oscillatory contribution to the transport properties. For example, diagonal resistivity is not constant anymore. Instead it oscillates with the inverse magnetic field $(1/B)$. The effect is shown in the experimental data at low magnetic field in Figure 2.3.

This oscillations are called Shubnikov-de Haas (SdH) oscillations, due to the modulation of DOS. The SdH oscillation is periodic in $1/B$ and its frequency is proportional to n_e. Each oscillation minimum corresponds to the minimum of DOS, while the Fermi energy stays in the middle of Landau levels. There are ν Landau levels being occupied. From the definition of ν, it is easy to understand these two oscillation features, and the density of electrons can be readily obtained from the oscillation period. The amplitude of oscillation can be derived from the quantum transport equation, using the Green function method [18]:

$$\frac{\Delta R}{4R_0} = \frac{A_T}{\sinh(A_T)} e^{-\pi/\omega_c \tau_0} \quad , \tag{2.21}$$

$$A_T = \frac{2\pi^2 kT}{\hbar \omega_c} \quad , \tag{2.22}$$

R_0 is the resistance at zero field and ΔR is the difference between R at oscillation peak and R_0. τ_0 is the quantum life time of an electron, which is quite different from the transport relaxation time τ. A_T is the temperature damping factor, which is rather small at low temperatures. τ_0 can be extracted from the exponential part by plotting a logarithmic normalized amplitude against inverse magnetic field. This plot is called a Dingle plot. From τ_0, the energy width (Γ) of expanded LL is derived by the formula:
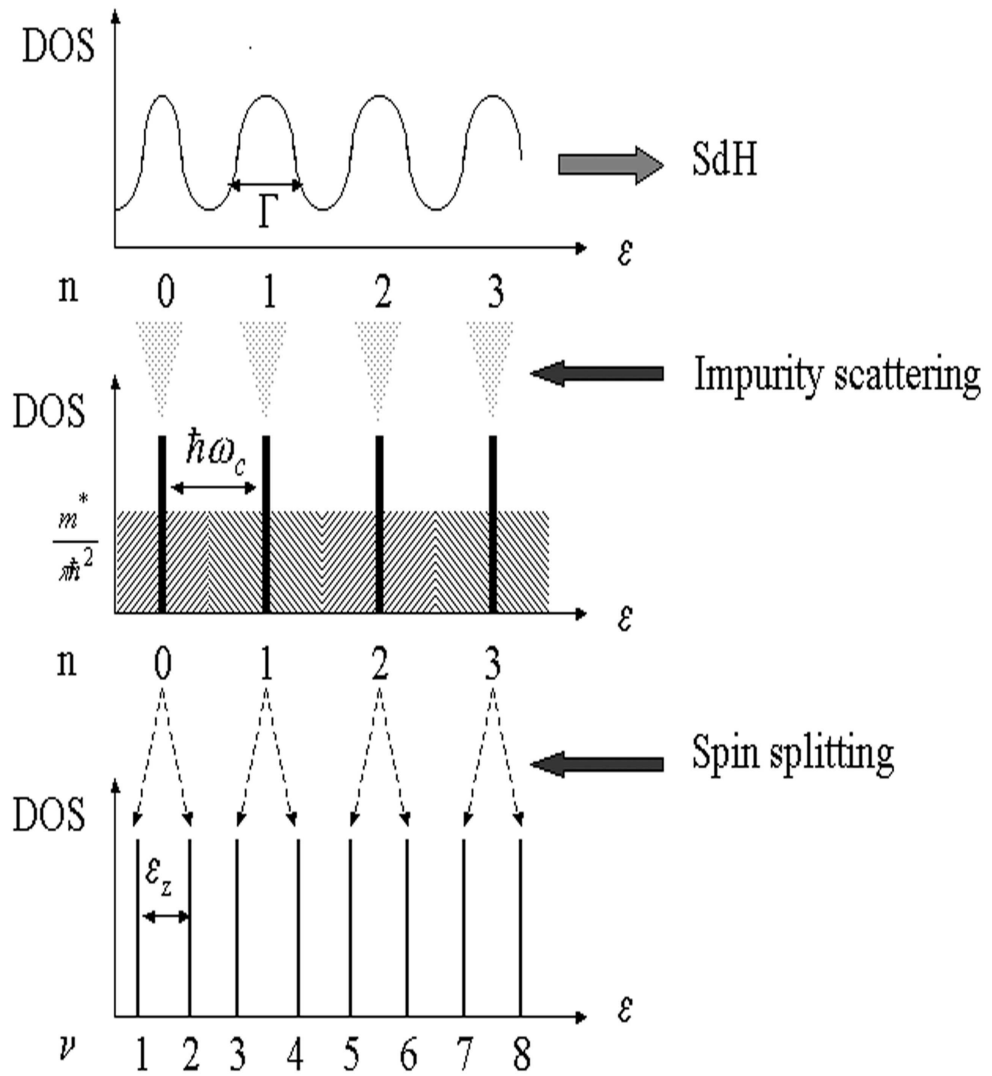
Figure 2.2. Landau level and density of states
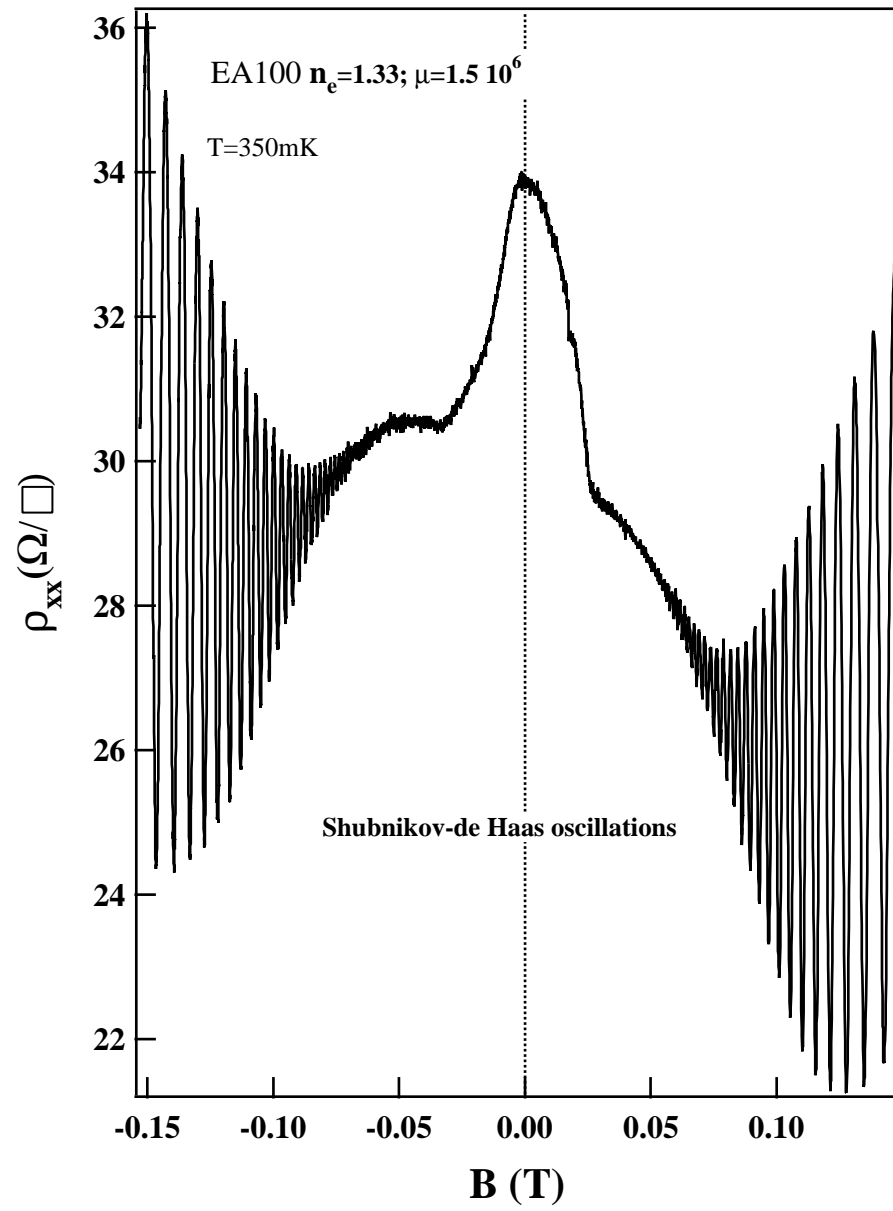
Figure 2.3. Shubnikov-de Haas oscillations

$$\Gamma = \frac{\hbar}{\tau_0} \quad . \tag{2.23}$$

Since the expression of ω_c includes m^*, m^* can be extracted from the temperature dependence of the oscillation amplitude. This is an important way to get effective mass from transport experiments

It is worth emphasizing that, for SdH oscillation, there is no change in Hall resistance. Hall resistance still keeps its classical straight line; however, this situation will change when going to a higher magnetic field at lower temperatures, provided that the sample is clean enough. Integer quantum Hall effect (IQHE) will then be observed.

2.4   Integer quantum Hall effect

IQHE was discovered by Klaus von Klitzing in 1980. Around certain filling factor, ν equal to an integer i, the Hall resistance is no longer a straight line but a plateau, and the diagonal resistance vanishes. Resistance tensor can be written as:

$$\widehat{R} = \begin{pmatrix} 0 & \frac{h}{e^2}\frac{1}{i} \\ -\frac{h}{e^2}\frac{1}{i} & 0 \end{pmatrix} \quad . \tag{2.24}$$

This observation is universal and independent of all microscopic details, such as sample materials, purity of sample, precise value of magnetic field, and so forth. It is a surprising macroscopic quantization phenomenon. The quantization number i is a simple integer, and the resistance R_H ($h/e^2 = 25812.807\Omega$) can be measured with a precision of about 10^{-10} and an absolute accuracy of about 10^{-8}[19]. This leads to two important applications: standard resistance reference in metrology labs and measurement of the fine structure constant (α). The fine structure constant is a dimensionless constant ($\sim \frac{1}{137}$) and of fundamental importance in quantum electrodynamics, written as:

$$\alpha \equiv \frac{\mu_0 c e^2}{2h} = \frac{\mu_0 c}{2R_H} \quad . \tag{2.25}$$

Based on the known value of the vacuum permittivity (μ_0) and speed of light (c), measurement of R_H is equivalent to measuring α.

Figure 2.4 shows IQHE measured in this thesis work. The order of Hall plateau of Hall resistance observed here can be as high as 40, and the diagonal resistivity approaches zero at the highest filling factor up to 30. Spin splitting already begins at $\nu = 25$, or around $B = 0.6$ T. At $B < 2$ T, there are beats resulting from two different electron densities occupying the first two subbands.

How can this phenomenon be understood? Based on the idea of localization and delocalization and, along with edge state theory [17, 20, 21], a standard picture can give a qualitative explanation [19, 21, 22, 20],

(A) 2D electrons are localized at low temperature, due to the existence of impurities. Localized electrons do not contribute to transport properties, so conductivity is zero and resistivity is infinity.

(B) In a low magnetic field, the localization is destroyed; however, in a high magnetic field ($\omega_c \tau \gg 1$), most electrons are localized again. Electron cyclotron motion is localized along the equi-potential line in a disordered potential area. Nevertheless, the most important fact is that *not* every state is localized, and there are always finite extended states centered at each Landau Level, which can be explained by percolation in finite-sized sample. Figure 2.5 shows the localized and delocalized (extended) states in the DOS spectrum.

(C) There are two important concepts in the Hall system at $\omega_c \tau \gg 1$. First, longitudinal (diagonal) conductivity comes from scattering due to disorder. This is opposite to the ordinary concept, where conductivity is reduced by disorder. Without scattering, both σ_{xx} and ρ_{xx} are zero. Second, even without an electric field along the longitudinal direction, the current can still be maintained by the Hall field.
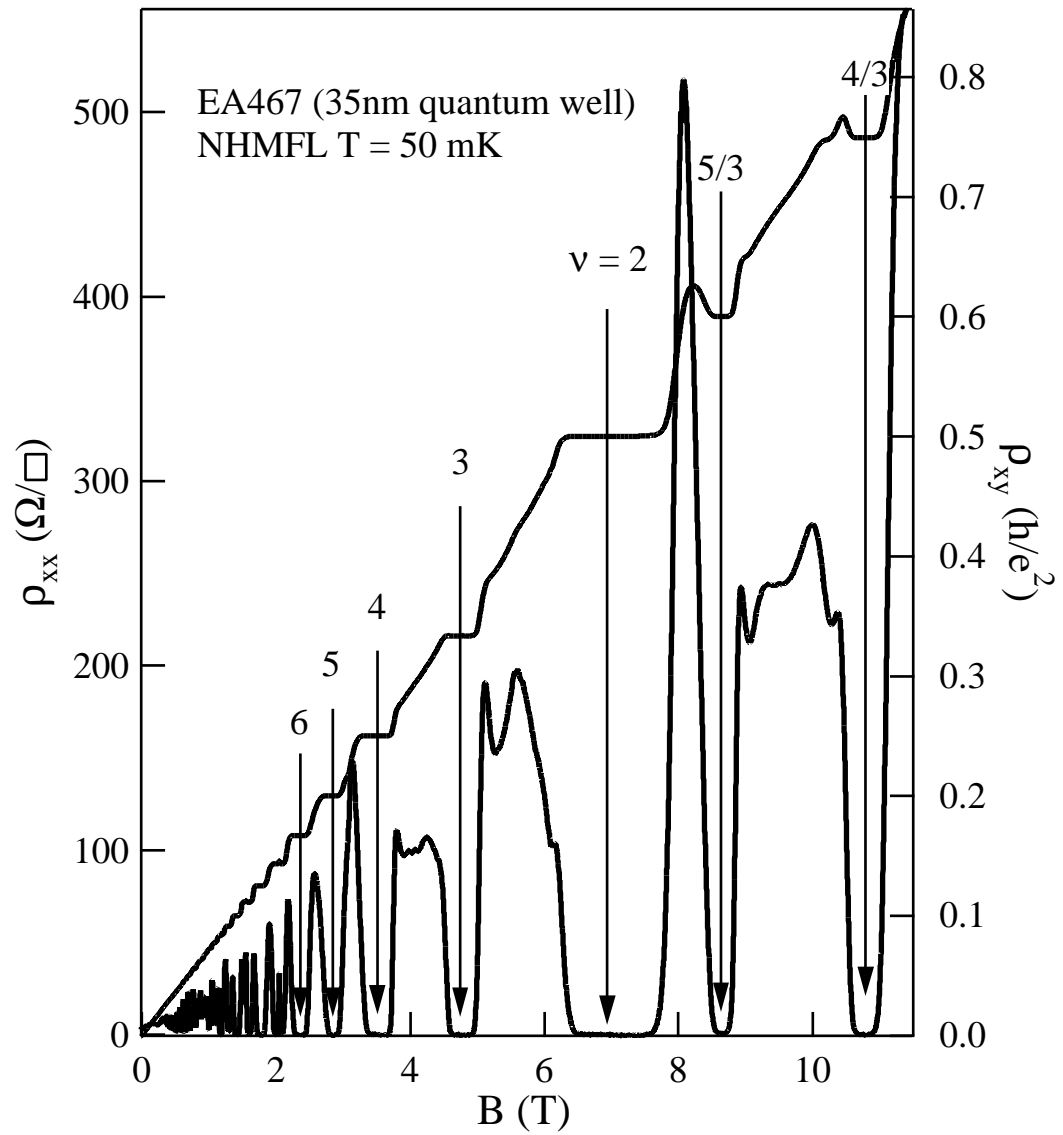
Figure 2.4. Integer quantum Hall effect
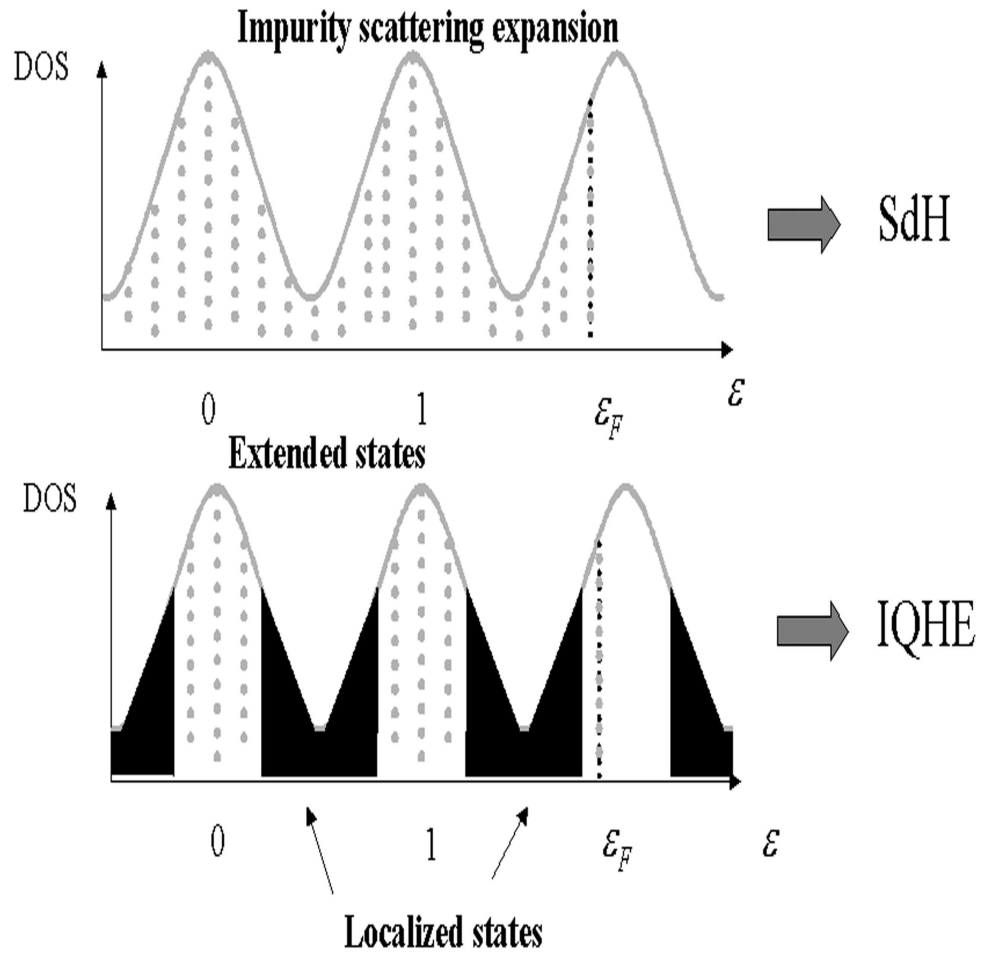
Figure 2.5. Localized and delocalized (extended) states in DOS spectrum

(D) When the Fermi level locates in the mobility gap (localized states interval), both conductivity and resistivity are zero. However, extended states at each LL carry the current, and have a contribution of h/e^2 to the Hall resistance. The total Hall resistance is thus $\frac{h}{e^2}\frac{1}{i}$, according to the parallel resistance principle. The Hall plateau can be observed.

(E) When the Fermi level lies in the extended region, there are some unoccupied extended states above the Fermi level, so scattering can occur at this region. Scattering produces finite conductivity and resistivity. A slight increase in magnetic field will change the density of the extended states at the Fermi level, as well as σ_{xx} and ρ_{xx}. The Hall plateau will then disappear.

(F) The phenomenon that the extended states below the Fermi level carry the current can be explained by the edge state theory. The confined potential at the sample edge bends all Landau levels up, then the Fermi level meets all Landau levels at the edge. In this way, all extended states are located on the Fermi level and are able to carry the current. The edge states that carry the current do not meet any back scattering, since the two opposite currents at these two edges are isolated by the wide bulk area. This is the reason why the Hall resistance can be quantized.

The exact quantization of Hall resistance requires symmetry or topological arguments, see, *e.g.*, a gauge invariance argument given by Laughlin in 1982 [23].

From argument (D), even though there are no extended states near the Fermi level when it locates within the mobility gap, there are extended states in the next LL above it. An energy gap equal to the LL interval ($\hbar\omega_c$) needs to be overcome when electrons are scattered from lower fully-occupied extended states to higher states. This is why the experimental value of longitudinal resistance in the mobility gap is proportional to $exp(-\hbar\omega_c/k_BT)$. It vanishes exponentially as T approaches zero.

In Figure 2.4, there are two plateaus on the Hall trace and corresponding zero resistivities on the ρ_{xx} trace. This is similar to IQHE, except that the filling factors are rational numbers of 5/3 and 4/3, not integers. The observation is

called fractional quantum Hall effect (FQHE). The underlying physics is related to electron-electron interaction. The observation of FQHE is a powerful example of many-body physics in a high-mobility 2DEG.

2.5 Fractional quantum Hall effect

Two years after the discovery of IQHE, Tsui, St$\ddot{o}$rmer, and Gossard discovered the fractional quantum Hall effect [2]. Their discovery was totally unexpected and astonishing. In a very high field, around filling factor ν=1/3, the Hall resistance develops a plateau at a value of $3h/e^2$, and the longitudinal resistance tends to zero as temperature is lowered. Figure 2.6 shows more FQH states at the lowest LL. The filling factor $\nu = p/q$ is a rational fraction with q an odd integer. The nature of FQHE can be understood as an incompressible quantum fluid, first proposed by Laughlin [3].

Instead of solving the Schr$\ddot{o}$dinger eigen equations with Coulomb interaction potential, Laughlin suggested a variational correlated wave function for $\nu = 1/m$ FQH state, with m=odd integer:

$$\Psi_{1/m} = \prod_{j<k} (z_j - z_k)^m \cdot \exp\left(-\frac{1}{4}\sum_l |z_l|^2\right) \quad , \tag{2.26}$$

where z is a complex plane coordinate. Lots of interesting features can be derived from this wave function. As two electrons approach each other, this wave function vanishes very fast due to mth power factor. This helps minimize the expectation value of the Coulomb energy and keep the system at a low energy state. At the ground state, the electron system is an incompressible quantum liquid, which means if the area of 2DEG is changed, a finite energy will be cost, and infinitesimal change is forbidden. This conjectured wave function turns out to have the most overlap with the true ground state wave function. Excitations of the $1/m$ ground state will appear at $T > 0$ or at filling factor slightly deviated from $1/m$. These quasi-particles carry a fractional charge of e/m and are capable of carrying an electric current. At exact $\nu = 1/m$, quasi-hole and quasi-electron can be produced in pairs with finite

467D (35nm well)

T=50mK

NHMFL
Hybrid magnet
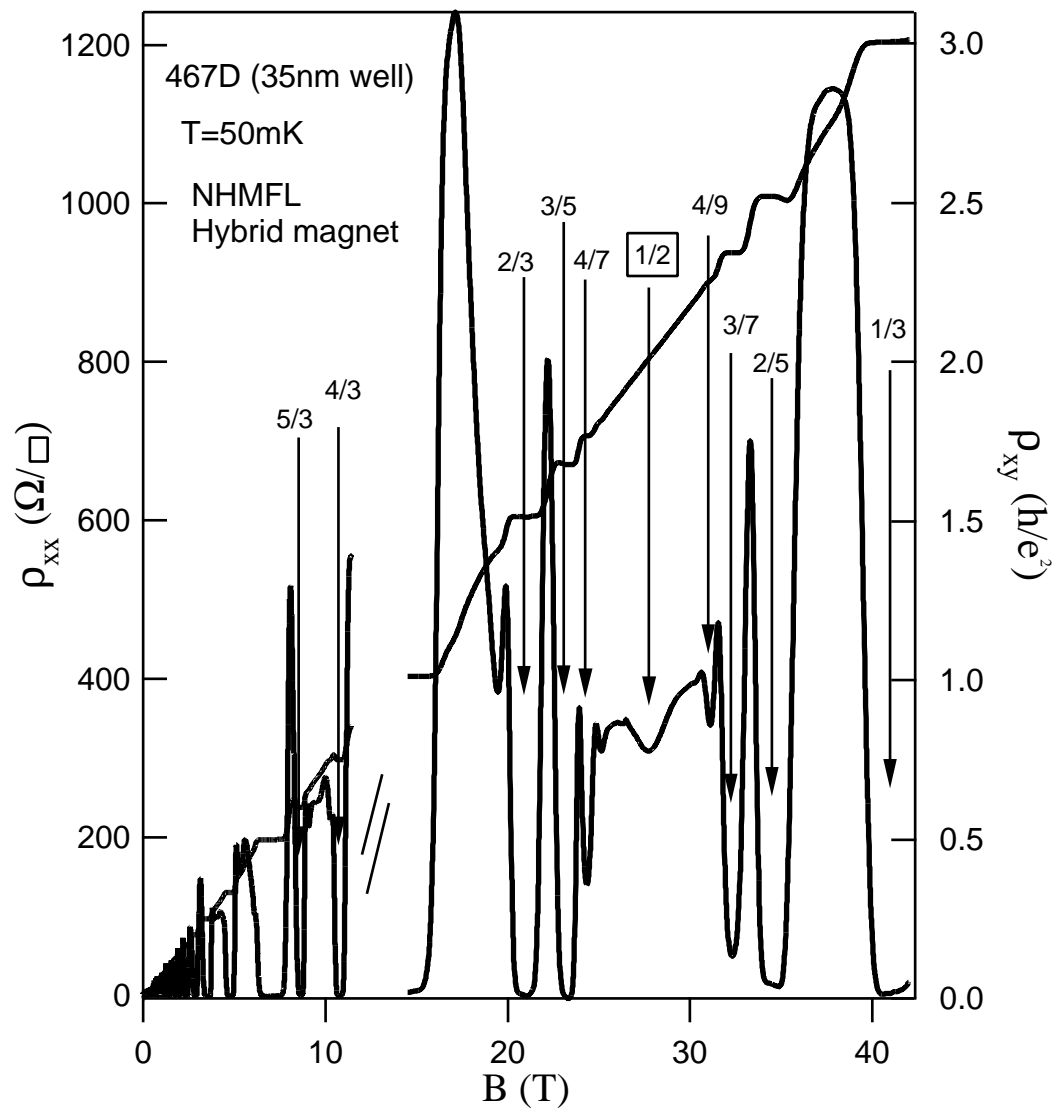
Figure 2.6. Fractional quantum Hall effect

energy cost, because there is a excitation energy gap (Δ) between the ground state and the excited state.

In a very clean sample subject to a high magnetic field, Coulomb interaction (correlation energy $= e^2/\epsilon l_B$) effect will prevail. Electrons are no longer localized by interplay of magnetic field and impurities. Instead they are able to carry current and contribute to the Hall resistance as $\frac{1}{\nu}h/e^2$. At $\nu = 1/m$, $R_{xy} = mh/e^2$. Due to the energy gap between ground state and excited state, there is no dissipation at this filling factor, so it is expected that R_{xx} approaches zero as T goes down to zero. As magnetic field slightly deviates from this filling factor, a small number of quasi-particles appear. Due to the existence of impurities, these quasi-particles are localized and cannot participate in carrying the current, so the Hall plateau can be formed. As B changes more, the number of quasi-particles increases, and eventually these quasi-particles are delocalized because of the interaction among them. The delocalized quasi-particles are able to contribute to the Hall resistance, then make it go back to classical Hall resistance again. Since the FQH states have smaller energy gaps (a few Kelvin) than IQH states, FQHE is much more sensitive to thermal fluctuation and impurity scattering.

As the density of quasi-particles increases, these quasi-particles may form another Laughlin liquid of the next generation, according to the hierarchy scheme [24]. For example, FQH states appear in order, such as $1/3 \rightarrow 2/5 \rightarrow 3/7 \rightarrow 4/9 \rightarrow 5/11 - --$. Considering the Electron-hole symmetry, another sequence of generation can be obtained as $2/3 \rightarrow 3/5 \rightarrow 4/7 \rightarrow 5/9 \rightarrow 6/11 - --$.

The value of energy gap can be extracted from the temperature dependence of R_{xx} in Arrhenius type of function, considering their activation behavior:

$$R_{xx} \propto e^{-\frac{\Delta/2}{k_B T}} \quad . \tag{2.27}$$

Fractional charges are observed in resonant tunneling experiment [25] and shot noise experiment [26]. In general, fractional charge is just the collective excitation of incompressible quantum liquid.

However, there is another possible theoretical model— Composite Fermions model, which can give us an excellent explanation of FQHE in a way similar to IQHE.

2.6 Composite Fermions

The Composite Fermion model is especially appealing in explanation of so-called "high-order" FQHE states emanating from the half filling factor. The composite Fermion [10, 11, 12, 13] is a quasi-particle , defined as a bound state of an electron and two flux quanta ($\phi_0 = h/e$). A Chern-Simons gauge transformation can be performed for such flux attachment. However, the stability of such gauge transformation must be guaranteed by the electron-electron interaction. Although having different mass, CF has the same electric charge and spin as electron. The most important difference between electrons and CFs is: weak interaction among CFs but strong Coulomb interaction among electrons. This feature makes it possible to transform the problem of strongly-interacting electrons to problem of weakly-interacting CFs.

In the mean field approximation, electron density is assumed to be uniform. The flux quanta attached to the electrons are smeared out, and their effect is equivalent to a uniform magnetic field having the direction opposite to the external magnetic field. Then effective magnetic field (B_{eff}) of CFs can be written as follows:

$$B_{eff} = B - 2n_e\phi_0 \quad .\qquad(2.28)$$

At $\nu = 1/2$, B_{eff} is zero, and the existence of a Fermi surface of CFs is predicted. Early SAW (Surface Acoustic Wave) results [15] can be explained by the existence of a CF Fermi surface at $\nu = 1/2$.

Reduced magnetic field for CFs means larger cyclotron radius, which can be expressed by the following formula:

$$R_c^{CF} = \frac{\hbar k_F^{CF}}{eB_{eff}} \quad ; k_F^{CF} = \sqrt{4\pi n_e} \quad ,\qquad(2.29)$$

where R_c^{CF} does not include the effective mass. This larger radius has been observed in the magnetic focusing experiments [27], which gave strong support to the Composite Fermions model.

The filling factors of electrons (ν) and CFs (p) are connected as follows:

$$\nu = \frac{p}{2p+1} \quad . \tag{2.30}$$

FQH states at 1/3, 2/5, 3/7, 4/9, and 5/11 now correspond to IQH states at $p=1$, 2, 3, 4, and 5. As $\nu \to 1/2$, $p \to \infty$. The corresponding energy gaps of these IQH states are:

$$E_{gap} = \hbar\omega_c^{CF} = \hbar\frac{eB_{eff}}{m_{CF}} \quad . \tag{2.31}$$

This reveals a relation that E_{gap} is proportional to B_{eff}. Experimental results showed some evidence about this linear relation [28].

Beyond the mean field approximation, the density fluctuation needs to be considered due to the singularity of electron in space as well as the existence of random potential of impurities. Once there is a local density fluctuation, the nearby CF can feel the Coulomb interaction. When a CF moves, it carries an electric current, and the attached flux quanta also move together with it. Due to Faraday's effect, the moving flux quanta produce an internal electric field, called Chern-Simons (CS) electric field (e), which can be obtained as follows [29]:

$$e = -\rho_{CS}j \quad ; \quad \rho_{CS} = \begin{pmatrix} 0 & 2h/e^2 \\ -2h/e^2 & 0 \end{pmatrix} \quad . \tag{2.32}$$

This CS electric field is fictitious, and can only be felt by another CF. A CF responds to both e and physical external electric field (E). What can be actually measured is only about the E; then the following expression can be derived:

$$j = \sigma_{CF}(E + e) \quad ; E = \rho j \quad ; \rho = \rho_{CF} + \rho_{CS} \quad . \tag{2.33}$$

The last equation gives the important relation between the theoretical calculated value (ρ_{CF}) and experimental value (ρ). The Hall resistivity of CFs is $\frac{1}{p}h/e^2$, and the CS Hall resistivity is $2h/e^2$, so the total measured Hall resistivity is $\frac{2p+1}{p}h/e^2 = \frac{1}{\nu}h/e^2$, which gives the correct Hall resistivity value.

Furthermore, at $\nu = 1/2$, the external magnetic field cannot exactly be cancelled out in every space point by the attached flux quanta. There is some magnetic field left at some points, so-called residual magnetic field (RMF), which affects greatly the transport properties of CFs around $\nu = 1/2$. The attached Chern-Simons flux quanta (Chern-Simons gauge field) also cause an interaction. When a CF moves, its bound flux quanta also move, and other CFs can feel the resulting change in the vector potential of gauge field. Thus an interaction (Chern-Simons gauge field interaction) between them appears. Around $\nu = 1/2$, transport properties are not well understood primarily due to these peculiar features of CFs.

As mentioned before, at $\nu = 1/2$, there is a composite Fermions sea with a defined Fermi surface. In general, the Fermi surface is not stable against going down to lower energy state; a more stable state can be reached by forming an energy gap between the ground state and the excited state at lower temperature. Pairing mechanism is a possible candidate in this case, and FQHE could appear at even filling factor[14, 16]. Experimental discovery of FQHE state at $\nu = 5/2$ is a good example [4, 30]. The possibility of FQHE at $\nu = 1/2$ in a single-layered 2DEG has remained a most interesting issue in the composite Fermion physics.

2.7 Thermopower basics

2.7.1 Phenomenological relations

When a temperature gradient (∇T) is applied to the 2DEG, an electric current (j) or electric field (E) would built up along the gradient. This phenomenon is called thermo-electric effects. On the other hand, an electric current also carries

heat current (Q) and produces thermal effects. These effects can be summarized in the following phenomenological relations [31]:

$$E = \rho j + S \nabla T \qquad j = \sigma E + \epsilon \nabla T \qquad S = -\rho \epsilon$$
$$Q = \Pi j - \kappa \nabla T$$
$$\Pi = ST \quad . \tag{2.34}$$

There are some definitions: S—thermo-electric power; ϵ—thermoelectric coefficient; Π—Peltier coefficient; κ—thermal conductivity. The last equation is called the second Kelvin relation. At the presence of a magnetic field, all coefficients are tensors, instead of scalars. Specifically, S_{xx} is called thermo-electric power, and S_{xy} is called Nerst-Ettingshausen coefficient. Generally, there are two kinds of mechanisms contributing to thermopower: electron diffusion (S^d) and phonon-drag (S^g) mechanisms.

For experimental measurement, there exist two standard configurations: 1) open circuit — $j = 0$, $S = E/\nabla T$; 2) closed circuit — $E = 0$, $\epsilon = j/\nabla T$. For the thermopower measurement, the open circuit method is always applied. By heating constantly at one end of the sample, a ∇T is built up, which is measured by two low temperature sensors. When the magnetic field is swept, the data of potential difference (voltage) between different contacts of 2DEG sample along the ∇T direction are recorded. $S_{xx}(B)$ is then calculated by open circuit equation.

There are several approaches to derive TEP theoretically:

1). Π approach: assume $\nabla T = 0$ and constant E, Q is calculated first, then Π can be obtained. S is derived from Π based on the second Kelvin relation.

2). Balance approach: assume $j = 0$ and constant ∇T, E is calculated from balance condition, then S is derived directly.

3). ϵ approach : assume $E = 0$ and constant ∇T, j is calculated first, then ϵ can be obtained. S is derived from the basic relation $S = -\rho \epsilon$.

The relaxation time approximation and the Boltzmann distribution equation are employed for detailed derivations.

2.7.2 Diffusive thermopower

The diffusion thermopower (S^d) measures the electron entropy, which is directly related to the DOS of a 2DEG. It is a powerful method to detect the change of DOS when electron states undergo a phase transition. Under the open circuit condition, electrons diffuse from the high temperature end to the low temperature end when a ∇T is applied. An electric field is then built up. The drift current (from E) cancels the diffusing current (from ∇T) so that there is no net electric current.

S_0^d can be derived by the ϵ approach:

$$
\begin{aligned}
\frac{\partial f}{\partial t} &= \frac{\partial f}{\partial t}\Big|_{drift} + \frac{\partial f}{\partial t}\Big|_{collision} \quad , \\
\frac{\partial f}{\partial t}\Big|_{drift} &= -\frac{dr}{dt}\cdot\nabla_r f - \frac{dk}{dt}\cdot\nabla_k f \quad .
\end{aligned}
\tag{2.35}
$$

At a steady state, $\partial f/\partial t = 0$. The collision term in the Boltzmann equation can be simplified by relaxation time ($\tau(k)$) approximation:

$$
\frac{\partial f}{\partial t}\Big|_{collision} = -\frac{f - f_0}{\tau(k)} \quad .
\tag{2.36}
$$

In the ϵ approach, no electric field exists and only the temperature gradient (∇T) is present. Under the first order approximation, $f = f_0 + f_1$ and $f \approx f_0$ in the drift term. Then f_1 can be derived as follows:

$$
f_1 = \tau(k)\frac{\partial f}{\partial \varepsilon}\frac{\varepsilon - \varepsilon_F}{T}v\cdot\nabla T \quad .
\tag{2.37}
$$

The current density (j) due to electron diffusion is obtained as follows:

$$
\begin{aligned}
j &= \frac{1}{A}\sum_{ks}(-ev)f(k) \\
&= 2\int(-ev)f(k)\frac{d^2k}{(2\pi)^2}
\end{aligned}
$$

$$= \int_0^\infty (-ev) f(k) g(\varepsilon) d\varepsilon$$
$$= \int_0^\infty (-ev) f_1(k) g(\varepsilon) d\varepsilon \quad , \tag{2.38}$$

where f_0 has no contribution to the current, s accounts for spin degree of freedom of electrons, and $g(\varepsilon)$ is the density of states, which is defined as:

$$g(\varepsilon) = 2 \int \delta(\varepsilon - \varepsilon_F) \frac{d^2 k}{(2\pi)^2} \quad . \tag{2.39}$$

From the phenomenological relations, ϵ is obtained as follows:

$$\epsilon = \frac{e}{\pi\hbar^2} \int_0^\infty \tau(k) \frac{\partial f}{\partial \varepsilon} \frac{\varepsilon - \varepsilon_F}{T} \varepsilon g(\varepsilon) d\varepsilon \quad . \tag{2.40}$$

Since $S = -\epsilon/\sigma$, S^d can be calculated easily. After completing the tricky integration, final result of S^d is expressed as follows:

$$S^d = -\frac{k_B}{e} \frac{3\pi^2 k_B T}{3} \frac{\sigma'(\varepsilon_F)}{\sigma(\varepsilon_F)} \quad . \tag{2.41}$$

This equation is called Mott's formula, which shows that the diffusive TEP depends linearly on temperature. Generally, $\tau \sim \varepsilon^p$, so,

$$S^d = -\frac{k_B}{e} \frac{\pi^2 k_B T}{3} \frac{p+1}{\varepsilon_F} \quad . \tag{2.42}$$

Because ε_F is proportional to n_e, S^d is thus inversely proportional to n_e. p is close to 1. For sample (EA100), $n_e = 2.03 \times 10^{11}$ cm^{-2}, at $T = 0.8$ K, $S^d \sim 6$ μV/K, which is much less than experimental value of 50μV/K. Thus phonon-drag mechanism must be dominant in this case.

When applying a magnetic field, the motion of electron is quantized. Quantum transport theory needs to be employed to calculate S^d. One of the results is that at

half filling factors, S^d reaches its maximum value. The result is easy to understand since S^d measures the entropy of 2DEG, which has the maximum value at half filling factors. Under the condition where $\hbar\omega_c \gg k_B T > \Gamma$ (Γ is the LL width), this value is independent of T, and is given by:

$$S^d = -\frac{k_B}{e}\frac{ln2}{\nu} = -\frac{60}{\nu} \quad (\mu V/K) \quad .$$ (2.43)

At ν=10 + 1/2, S^d_{xx} has the value of 6μ V/K, which is also much less than our experimental value of $(50\mu$ V/K). This result shows that the diffusive TEP plays a minor role in the sample studied.

2.7.3   Phonon-drag thermopower

When there is a temperature gradient (∇T) along the sample, phonons flow from the hot place to the cold place, and a heat current (Q) is produced. Along the ∇T direction, there is a net momentum density (P) of phonons, which is partially transferred to 2D electrons. Electrons gain the momentum (P_e), and flow along the same direction. Under the open circuit condition, an electric field is built up and the resulting electric current cancels out the phonon-drag electron flow. By this balance approach, zero magnetic field TEP (S_0^g), based on the phonon drag mechanism, can be easily derived at macroscopic level [32].

For 3D phonons, $P = Q/v_s^2$, where $Q = -\kappa\nabla T$ and $\kappa = C_v v_s^2 \tau_p/3$. Then P can be written as:

$$P = -\frac{1}{3}C_v\tau_p\nabla T \quad .$$ (2.44)

The ratio of P_e to P is τ_e/τ_{pe}, where τ_{pe} is the electron relaxation time, due to electron-phonon interaction (EPI):

$$P_e = P\frac{\tau_e}{\tau_{pe}} \quad .$$ (2.45)

The phonon-drag electric current is $-eP_e/m^*$. E is then built up and the resulting drift current cancels out this phonon-drag current:

$$
\begin{aligned}
E &= -\frac{1}{\sigma}\frac{-eP_e}{m^*} \\
&= \frac{m^*}{n_e e^2 \tau_e}\frac{e}{m^*}\frac{\tau_e}{\tau_{pe}}P \\
&= \frac{1}{n_e e}\frac{P}{\tau_{pe}} \quad .
\end{aligned}
\tag{2.46}
$$

On the other hand, $E = S\nabla T$, so S_0^g is finally obtained :

$$
\begin{aligned}
S_0^g &= -\frac{1}{3e}\frac{C_v}{n_e}\frac{\tau_p}{\tau_{pe}} \\
&\propto \frac{T^3}{n_e} \quad .
\end{aligned}
\tag{2.47}
$$

Generally, the impurity scattering is dominant in τ_e at low temperature. It is very important that τ_e is cancelled out in Equation 2.46, which means that the electron-impurity scattering does not enter into S^g; only the electron-phonon scattering matters. This feature makes S^g a powerful tool to detect electron-phonon interaction at low temperature. S_0^g is proportional to T^3 and $1/n_e$. T^3 temperature dependence is an important criterion to distinguish S^g from S^d.

A rigorous derivation of S_0^g can be found based on the Boltzmann equation [33, 34, 35]. The ϵ approach is followed. The electric current is induced by nonequilibrium phonon, which is the result of ∇T. In the Boltzmann equation, the drift term is ignored, which is only responsible for the diffusive TEP. The collision term can be expressed as follows:

$$
\frac{\partial f}{\partial t}\Big|_{collision} = \frac{\partial f}{\partial t}\Big|_{impurity} + \frac{\partial f}{\partial t}\Big|_{epi} = 0 \quad ,
$$

$$0 = -\frac{f - f_0}{\tau_{ei}} + 2\sum_{k'}[f(k')(1 - f(k))P_q(k',k) - f(k)(1 - f(k'))P_q(k,k')] \quad,$$

$$f_1 = \tau_{ei}2\sum_{k'}[f_0(k')(1 - f_0(k))P_q(k',k) - f_0(k)(1 - f_0(k'))P_q(k,k')] \quad. (2.48)$$

A first order approximation is employed in the last equation. $P_q(k',k)$ is the scattering probability from k' state to k state, due to both phonon absorption and phonon emission scattering processes. From the Fermi gold rule, $P_q(k',k)$ is shown as follows:

$$P_q = P_q^{absorption} + P_q^{emission} \quad,$$

$$P_q^{absorption} = \frac{2\pi}{\hbar}N_q A_q(k',k)\delta(k - k' - q)\delta(\varepsilon_k - \varepsilon_{k'} - \hbar\omega_q) \quad,$$

$$P_q^{emission} = -\frac{2\pi}{\hbar}(N_q + 1)A_q(k',k)\delta(k' - k - q)\delta(\varepsilon_{k'} - \varepsilon_k - \hbar\omega_q) \quad. (2.49)$$

k and q are the wave vectors of electron and phonon, respectively. $A_q(k',k)$ is the squared matrix element of EPI, due to deformation potential scattering and pizeoelectric effect mechanisms. A_q is independent of k and k'. Its explicit form is given at $B = 0$ as follows:

$$A_q = (|V_{ql}|^2 + |V_{qt}|^2)\delta(q_z) \quad,$$

$$\delta(q_z) = |\int \phi^*(z)e^{iq_z Z}\phi(z)dz|^2 \quad,$$

$$|V_{ql}|^2 = \frac{\hbar q}{2\varepsilon(q_{\parallel})^2 \varrho v_l}(E^2 + (eh_{14})^2\frac{A_l}{q^2}) \quad,$$

$$|V_{qt}|^2 = \frac{\hbar q}{2\varepsilon(q_{\parallel})^2 \varrho v_t}(eh_{14})^2\frac{A_t}{q^2} \quad, \tag{2.50}$$

where $q = (q_{\parallel}, q_z)$. $\delta(q_z)$ is a factor of finite 2DEG thickness along the z direction; l is for the longitudinal acoustic phonon modes and t for transverse modes; E is the coupling strength for the deformation potential; h_{14} is the coupling constant of the piezoelectric effect; ϱ is the mass density of GaAs; v_l and v_t are phonon velocities; A_l

and A_t are anisotropic factors, given by $9q_\parallel^4 q_z^2/2q^6$ and $(8q_\parallel^2 q_z^4+q_\parallel^6)/4q^6$ respectively; $\varepsilon(q_\parallel)$ is the static dielectric screening constant, given as follows:

$$\varepsilon(q_\parallel) = 1 + \frac{2\pi e}{\kappa_s q_\parallel} D(\mu)F(q_\parallel) \quad , \tag{2.51}$$

κ_s is the dielectric constant of GaAs, $D(\mu)$ is the DOS of 2DEG, and $F(q_\parallel)$ is the form factor.

N_q is the phonon distribution function, which is just the Bose-Einstein distribution function (N_q^0) at equilibrium state. Only nonequilibrium N_q can have contribution to f_1. This quantity can be derived from the phonon Boltzmann equation:

$$\upsilon_s \cdot \nabla N_q = -\frac{N_q - N_q^0}{\tau_p} \quad . \tag{2.52}$$

Under the first order approximation, the equilibrium N_q^0 will substitute N_q at the left side, then:

$$\delta N_q = \tau_p \upsilon_s \frac{dN_q^0}{d(\hbar w_q)} \frac{\hbar w_q}{T} \nabla T \quad . \tag{2.53}$$

After long and tedious calculations and simplifications, S_0^g is obtained for the deformation potential scattering:

$$
\begin{aligned}
S_0^g &= -\frac{k_B}{e} \frac{m^* \hbar E^2 \upsilon_l \Lambda}{(2\pi)^2 (k_B T)^2 \varrho n_e} \int \delta(q_z) dz \int \frac{q_\parallel^3 q^2 G(q) H(q)}{\varepsilon(q_\parallel)^2} dq_\parallel \quad , \\
G(q) &= \frac{1}{[(\frac{\hbar k_F q}{m^*})^2 - (\hbar\omega_q - \frac{\hbar^2 q^2}{2m^*})^2]^{\frac{1}{2}}} \quad , \\
H(q) &= \frac{e^{\frac{\hbar\omega_q}{k_B T}}}{(e^{\frac{\hbar\omega_q}{k_B T}} - 1)^2} \quad .
\end{aligned}
\tag{2.54}
$$

At very low temperature, further simplification can be made where $q \ll 2k_F$,

and hence $\delta(q_z) \to 0$, $F(q_\parallel) \to 1$, and $G(q) \to m^*/\hbar^2 k_F q$. Performing variable transformation by using $u = \hbar q_\parallel v_l/k_B T$ and $w = \hbar q_z v_l/k_B T$, the final explicit expression is obtained as follows:

$$S_0^g = -\frac{k_B}{e} \frac{\kappa_s^2 E^2 \Lambda k_B^6}{2^{11/2}\pi^{7/2}\varrho e^4\hbar^5 v_l^7} \frac{T^6}{n_e^{3/2}} \int_{-\infty}^{\infty} dw \int_0^{\infty} u^4(u^2+w^2)\frac{e^\gamma}{(e^\gamma-1)^2}du \quad . \qquad (2.55)$$

A very important result is the T^6 temperature dependence for the deformation potential. For the piezoelectric effect, S_0^g can be derived by substituting E^2 with $(eh_{12})^2 A_s/q^2$:

$$S_0^g(s) = -\frac{k_B}{e} \frac{\kappa_s^2 (eh_{12})^2 \Lambda k_B^4}{2^{11/2}\pi^{7/2}\varrho e^4\hbar^3 v_s^5} \frac{T^4}{n_e^{3/2}} \int_{-\infty}^{\infty} dw \int_0^{\infty} u^4 \frac{e^\gamma}{(e^\gamma-1)^2} A_s du \quad . \qquad (2.56)$$

Because these two mechanisms have different temperature dependence, at higher temperatures, the deformation potential effect is dominant for S_0^g, whereas at lower temperatures, the piezoelectric effect is more effective.

2.7.4 Phonon-drag thermopower in a magnetic field

In a magnetic field, the motion of electron is quantized. A formal derivation is based on the Kubo Green function method. However, there is a simple method [36, 37] based on the Π approach. Under high magnetic field condition ($\omega_c\tau = B\mu \gg 1$) (for samples studied, $\mu = 300$ m^2/Vs then $B > 0.03$ T), several approximate relations can be obtained as follows:

$$\rho_{xy} \gg \rho_{xx} \quad ,$$
$$\sigma_{xy} \gg \sigma_{xx} \quad ,$$
$$J_y \gg J_x \quad ,$$

$$\epsilon_{xy} \quad \gg \quad \epsilon_{xx} \quad . \tag{2.57}$$

Consequently, $S_{xy} \ll S_{xx}$ and $\Pi_{xx} \gg \Pi_{xy}$. The Π approach assumes that $\nabla T = 0$, and E is along the x direction. The diagonal phonon-drag TEP (S_{yy}) can be derived as follows:

$$
\begin{aligned}
S_{yy} &= \frac{\Pi_{yy}}{T} \\
&= \frac{Q_y}{j_y} \frac{1}{T} \\
&= \frac{\rho_{yx}}{E} \frac{1}{T} Q_y \quad , \\
Q_y &= \sum_{qS} \delta N_q \hbar \omega_{qS} v_y \quad , \\
v_y &= \frac{d\omega_{qS}}{dq_y} = v_s \frac{q_y}{q} \quad .
\end{aligned}
\tag{2.58}
$$

E produces a large electric current along the y direction (j_y), which causes phonons to slightly deviate from equilibrium state and produces heat current (Q_y) through EPI. At first, Q_y can be derived by the phonon Boltzmann equation, Π and S can be obtained later on.

The phonon Boltzmann equation can be written as follows:

$$
\begin{aligned}
0 &= \frac{\partial N_q}{\partial t}\Big|_{boundary} + \frac{\partial N_q}{\partial t}\Big|_{epi} \quad , \\
0 &= -\frac{\delta N_q}{\tau_p} + \frac{\partial N_q}{\partial t}\Big|_{epi} \quad .
\end{aligned}
\tag{2.59}
$$

The EPI term can be expressed in a similar way as in the previous section. However, there are some differences: 1) since the change of N_q (δN_q) is concerned, sum over all electron states is necessary; 2) in a magnetic field, electron states are labeled by LL index-n and k, and electron wave function is written as the superposition of a plane wave function along the y direction and an oscillator wave function along the x

direction in the Landau gauge; 3) N_q can be approximated by the equilibrium Bose-Einstein distribution function, where f is a nonequilibrium distribution function due to the existence of E and B.

f can be derived from the electron Boltzmann equation as follows:

$$
\begin{aligned}
\frac{dk}{dt} \cdot \nabla_k f &= -\frac{f_1}{\tau_e} \quad , \\
\frac{dk}{dt} &= -\frac{e}{\hbar}(E + v_e \times B) \quad .
\end{aligned}
\tag{2.60}
$$

f_1 can then be calculated. Substituting f_1 into the phonon Boltzmann equation, δN_q can be obtained immediately, then Q_y can be found. The final result is:

$$
S_{xx}^g(B) = \frac{-k_B h}{ep(k_B T)^2} \sum_{\mathbf{q}S} \sum_{n,\ell} u_s \Lambda_{\mathbf{q}} q_y^2 \, N_{\mathbf{q}} |V_{\mathbf{q}S}|^2 \Delta_z(q_z) \Delta_{n,\ell}(q_\parallel)
$$
$$
\times \int d\varepsilon \rho_n(\varepsilon) \int d\varepsilon' \rho_{n'}(\varepsilon') f(\varepsilon)[1 - f(\varepsilon')]\delta(\varepsilon + \hbar\omega_{\mathbf{q}S} - \varepsilon') \quad ,
\tag{2.61}
$$

where p is the LL filling factor for the spin-degenerate case, $\Lambda_{\mathbf{q}}$ the phonon mean-free-path, $N_{\mathbf{q}}$ the boson occupation function, $\rho_n(\varepsilon)$ the spectral DOS at the nth Landau Level, and $f(\varepsilon)$ the Fermi function. The strength of electron-phonon interaction $|V_{\mathbf{q}S}|$ and the q_z-conservation factor $\Delta_z(q_z)$ are given in Equation 2.50. $\Delta_{n,\ell}(q_\parallel)$ is the in-plane-momentum conservation factor:

$$
\Delta_{n,\ell}(q_\parallel) = \frac{n!}{(n+\ell)!}\chi^\ell e^{-\chi}[L_n^\ell(\chi)]^2 \quad , \qquad \chi = \frac{(q_\parallel l_B)^2}{2} \quad .
\tag{2.62}
$$

$\ell = 0$ is for the intra-LL scattering; $\ell \neq 0$ is for the inter-LL scattering. Numerical simulation is needed to show the temperature dependence of $S_{xx}^g(B)$.

CHAPTER 3

LOW FIELD OSCILLATIONS OF
THERMOPOWER

Thermopower measurement has been performed in the quantum Hall system for almost two decades. Similar to diagonal resistance measurement, TEP experimental data have shown the integer quantum Hall effect and the fractional quantum Hall effect in 2DEG in GaAs-AlGaAs heterostructure [38, 39, 40, 41, 42]. The early experimental data of TEP were explained by the phonon-drag mechanism [43], instead of the well-known diffusion mechanism. Later, it was clear that phonon-drag mechanism was dominant at $T > 300$ mK in the high-mobility sample [34], while the diffusion mechanism was responsible at $T < 100$ mK in 2DHS (2D holes system) [44]. After the composite Fermion model was developed, TEP experiments gave support for this model both in the diffusive TEP [44, 45] and the phonon-drag TEP regimes [34, 46]. All experimental data showed that the intra-LL scattering was dominant in a magnetic field.

In this chapter, experimental data in a low field ($B < 0.5$ T) are shown. This reveals a new class of oscillations, related to the inter-LL scattering mechanism and acoustic magneto-phonon resonance. These results are remarkably different from the previous TEP works.

3.1 Thermopower setup

Low temperatures ranging from 300 mK to 2 K can be achieved in a top-loaded ^{3}He refrigerator (OXFORD Heliox^{TL} ^{3}He refrigerator). At approximately 1.3 K, which is obtained by mechanical-pumping of ^{4}He, ^{3}He gas begins to condense. The temperature of the ^{3}He liquid is reduced by evaporation, a process facilitated by a charcoal sorption pump set at low temperatures between 4 K and 45 K.

Changing temperature of the sorption pump gives control of the temperature of ^{3}He liquid between 300 mK and 1.5 K. The TEP setup is immersed in the ^{3}He liquid. Magnetic field is supplied by a 12 Tesla superconducting magnet made from Niobium-Titanium ($NbTi$) and Niobium-Tin (Nb_3Sn) superconducting coils. Its superconducting transition temperature is around 8 K. The magnetic field is always perpendicular to 2DEG in our TEP experiments.

Hall bar mesa is lithographically defined on 2 mm $\times$ 8 mm $\times$ 0.5 mm wafer; the lithographic procedure is given in Table 3.1. The width of Hall bar is 0.5 mm. The 10 contacts are made by diffusing Indium into 2DEG at 400 ^{o}C for 10 minutes in 15% hydrogen and 85 % nitrogen forming gas.

TEP setup is schematically shown in Figure 3.1. The vacuum can is made of Stycast epoxy 1266 (AB). The cold sink of copper is extended into ^{3}He liquid. One end of the sample is Indium soldered onto the cold sink. On the other end, a strain gauge serving as a heater is glued by Ag paint. Two Ruthenium Oxide bare chip sensors are glued at the back of the sample by Epoxy 2850 FT. All wires are anchored on a plastic plate attached to the cold sink. These wires are 38 gauge Manganin and serve as connection between the inside and the outside. Alternative configurations for the TEP setup can be found in [39, 40, 47, 48, 42, 44, 45] for different low temperature systems. All the low temperature parameters of the materials can be found in the book "Matter and Methods at Low Temperature" [49].

Stycast epoxy 1266 (AB) [50] is easily cast and modeled. It is semitransparent and suitable for red light LED illumination purpose (to change electron density). It is strong enough to resist the pressure when the air inside is condensed. Its relative linear expansion coefficient (-1.15%) is larger than the copper's (-0.3%) at $T \sim 4$K, which means a compression seal can be readily formed between the Stycast and the copper cold sink at low temperatures.

Copper (OFHC) has the highest thermal conductivity ($\kappa = 1 - 10$ W/cmK) at $T \sim 0.5$ K among normal pure metals, and it is easy to solder. Al also has the same order of thermal conductivity as copper; however, it becomes a superconductor at

Table 3.1. Procedure of optical lithography

Step	Tool	Parameter
1. Photoresist coating	Spinner	1813 (positive) 60s 9000rpm
2. Soft baking	Hot plate	195 °F 60s
3. Exposure	Aligner	UV light 120s
4. Developing	352 solution	15-30s
5. Hard baking	Hot plate	250 °F 180s
6. Etching	10:8:1 solution	60 nm/s 12s
7. Removing 1813	Acetone	5 min
8. Cleaning	Acetone-Methanol-DI	supersonic 20 min each
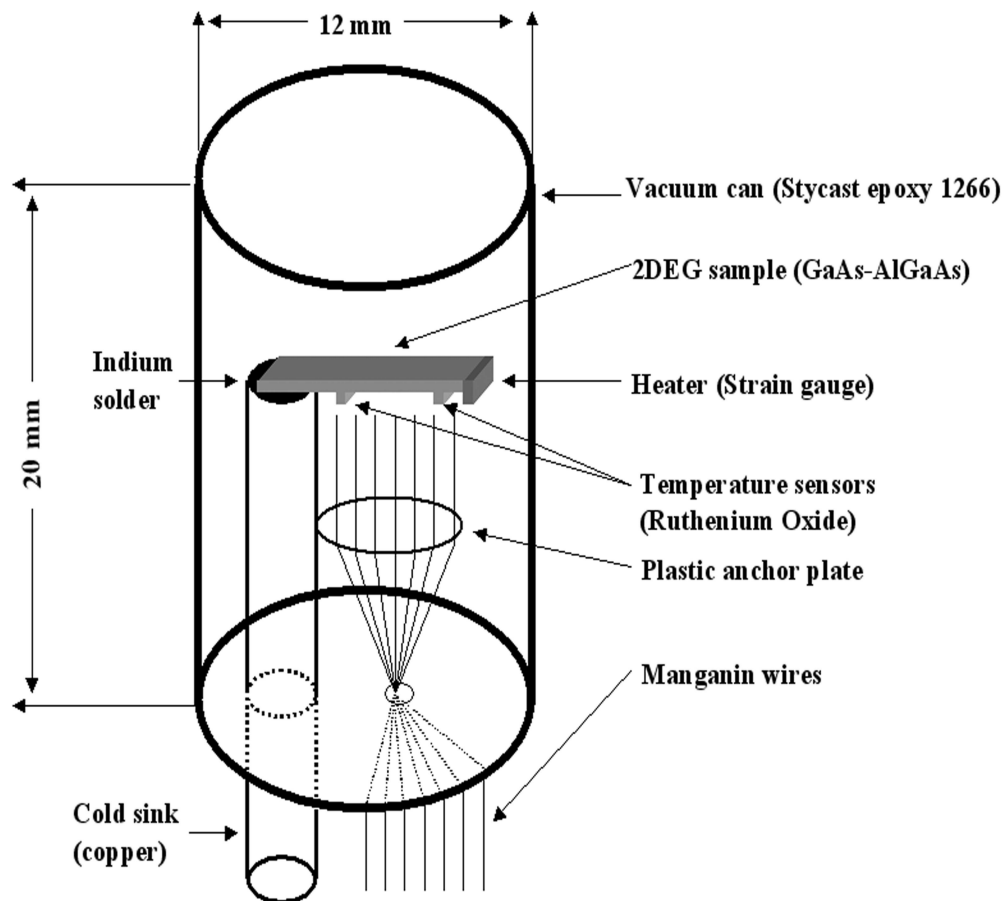
Figure 3.1. Thermopower set-up

1.18 K. No obvious thermal boundary resistance (Kapitza resistance) exists between copper and ^{3}He liquid at 0.3 -1 K [49].

Thermal anchoring of the sample (GaAs substrate) to the cold sink is usually done by Indium soldering. Comparing with alternative methods using Ag paint, GE 7031 varnish, and epoxy, soldering has relatively good thermal contact as well as reliable holding strength after thermal cycling. Although the thin layer of Indium becomes a superconductor at $T < 3.4$ K, its superconducting state is destroyed at $B = 0.02$T.

Ruthenium oxide sensor (Lakeshore RX-102A-BR) [51] has a relatively small magnetoresistance, and works fine in the magnetic field. The bare chip is small enough (1.2 mm $\times$ 1.5 mm). Therefore it can be glued to the sample back directly by Epoxy 2850FT [52]. Manganin wire has a very poor thermal conductivity (0.0001 W/cmK) at low temperature, so the thermal leakage can be ignored.

Strain gauge (HBM, LY-11-1.5/120) [53] can be made very small (for example, 1.0 mm $\times$ 1.5 mm) to suit our purpose. It has resistance of 110 Ohm at low temperature. Ag paint [54] is used to glue strain gauge to the sample.

Ruthenium Oxide sensors are calibrated in the thermal equilibrium environment by a Spear sensor, which again is calibrated by a Ge commercial standard low temperature sensor (Lakeshore GR-200). Sensor resistance is measured by a resistance bridge (AVS-47). Experimental data show that there is no change of sensor resistance at the magnetic field up to 1 T. After the calibration, the thermal conductivity of GaAs wafer is measured at low temperature. The T^3 temperature dependence is shown in Figure 3.2, which is good evidence of our reliable calibration.

A sinusoidal wave from the voltage output of a lock-in amplifier is applied to the heater. The temperature gradient produced by heater is expressed as follows;

$$
\begin{aligned}
Q &= \frac{V_0^2}{AR_0}cos(\omega t)^2 = -\kappa\nabla T \quad , \\
\nabla T &= -\frac{V_0^2}{2AR_0\kappa}(cos(2\omega t) + 1) \quad .
\end{aligned}
\tag{3.1}
$$
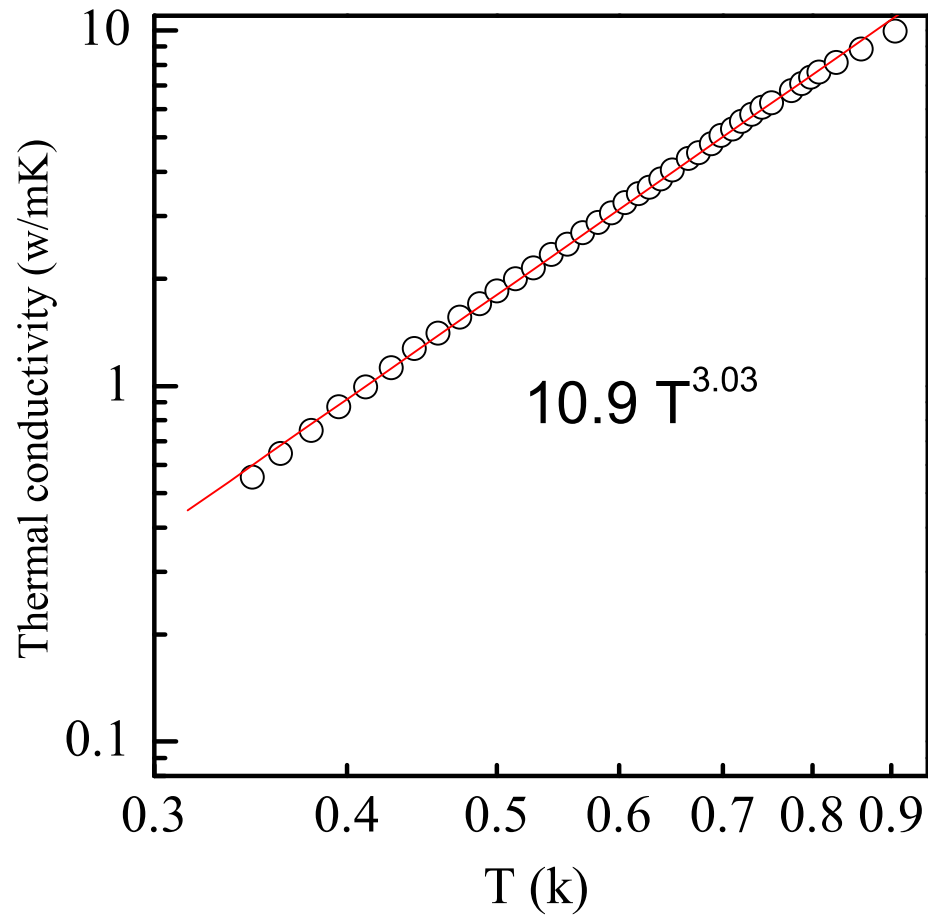
Figure 3.2. Temperature dependence of thermal conductivity of GaAs wafer

∇T is measured by AVS-47, which corresponds to the constant term in Equation 3.1. A lock-in amplifier registers the voltage signal at the frequence of 2ω. ω is set to 2.7 Hz for all TEP measurements. The measurement diagram is shown in Figure 3.3.

3.2 Experimental data in a low magnetic field for EA100 sample

In this section, all experimental data come from the sample EA100, which is made from a $GaAs/Al_{0.3}Ga_{0.7}As$ heterostructure grown by molecular beam epitaxy on the (001) GaAs substrate in the Sandia National Laboratories. At low temperature ($T \sim 2$ K), the n_e and the μ can be varied using a red light-emitting diode (LED). Without LED (saturate LED), the n_e (in unit of $10^{11}cm^{-2}$ throughout this thesis) ~ 1.33 (2.03) and $\mu \sim 2 \times 10^6$ (3×10^6) (in unit of cm^2/Vs throughout this thesis).

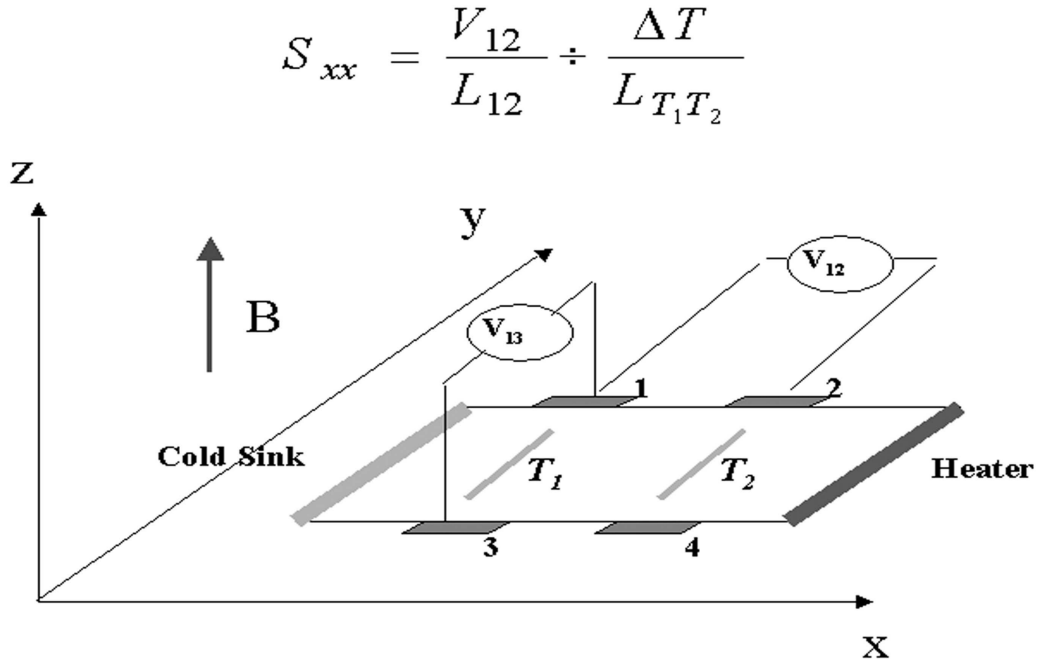$$S_{xx} = \frac{V_{12}}{L_{12}} \div \frac{\Delta T}{L_{T_1 T_2}}$$

Figure 3.3. Thermopower measurement diagram

3.2.1 Experimental data of magneto-TEP

Figure 3.4 shows magneto-TEP in a low magnetic field at 800 mK. First of all, the trace reveals a new type of strong oscillations that appear only at $B < 0.3$ T, where SdH oscillations are relatively weak. Four maxima can be seen clearly in the trace of $n_e = 2.03$. The arrows indicate the maxima (indexed as $l = 1, 2, 3, 4$). Second, - $d^2 S_{xx}/dB^2$ is shown in the middle figure, which reveals stronger oscillation structures. In the bottom figure, the order of oscillations(l) is plotted against $1/B$, which shows a linear relation. It is interesting that the SdH oscillations co-exist with the $l = 1$ maximum. In other words, the new oscillations do not destroy the SdH oscillations; it looks like a new structure just overlaps with the weak low field SdH oscillations. The width of maxima in the new oscillations is much greater than that of SdH oscillations.

In Figure 3.5, it can be seen that the maxima of the new oscillations shift consistently toward the higher field with increasing density, and higher order structures are resolved; meanwhile the peak value and zero field value drop as expected for phonon-drag TEP. In the middle figure, the fast Fourier transformation (FFT) is performed to the original data, and the frequency of the new oscillation is obtained. The bottom figure shows that this frequence is linear with $\sqrt{n_e}$, which is different from the SdH oscillations, whose frequency is proportional to n_e.

Figure 3.6 shows the temperature dependence of the new oscillations for density of 2.03 . The new oscillations are stronger as the temperature goes higher. At $T = 800$ mK, the oscillation amplitude is up to 35%, which is much bigger than 5% of the low field oscillations of MR [55]. This fact not only proves the phonon-scattering nature in the new oscillation of TEP, but also shows that TEP is a powerful tool to directly detect electron-phonon interaction (EPI) as compared to MR at low temperature. As T increases, the absolute value of the new oscillations increase faster than those of zero-field and SdH oscillations. This shows that the inter-LL scattering is dominant in the new oscillations, because the inter-LL scattering mechanism leads to an exponential temperature dependence, whereas the intra-LL scattering mechanism has a power law dependence.
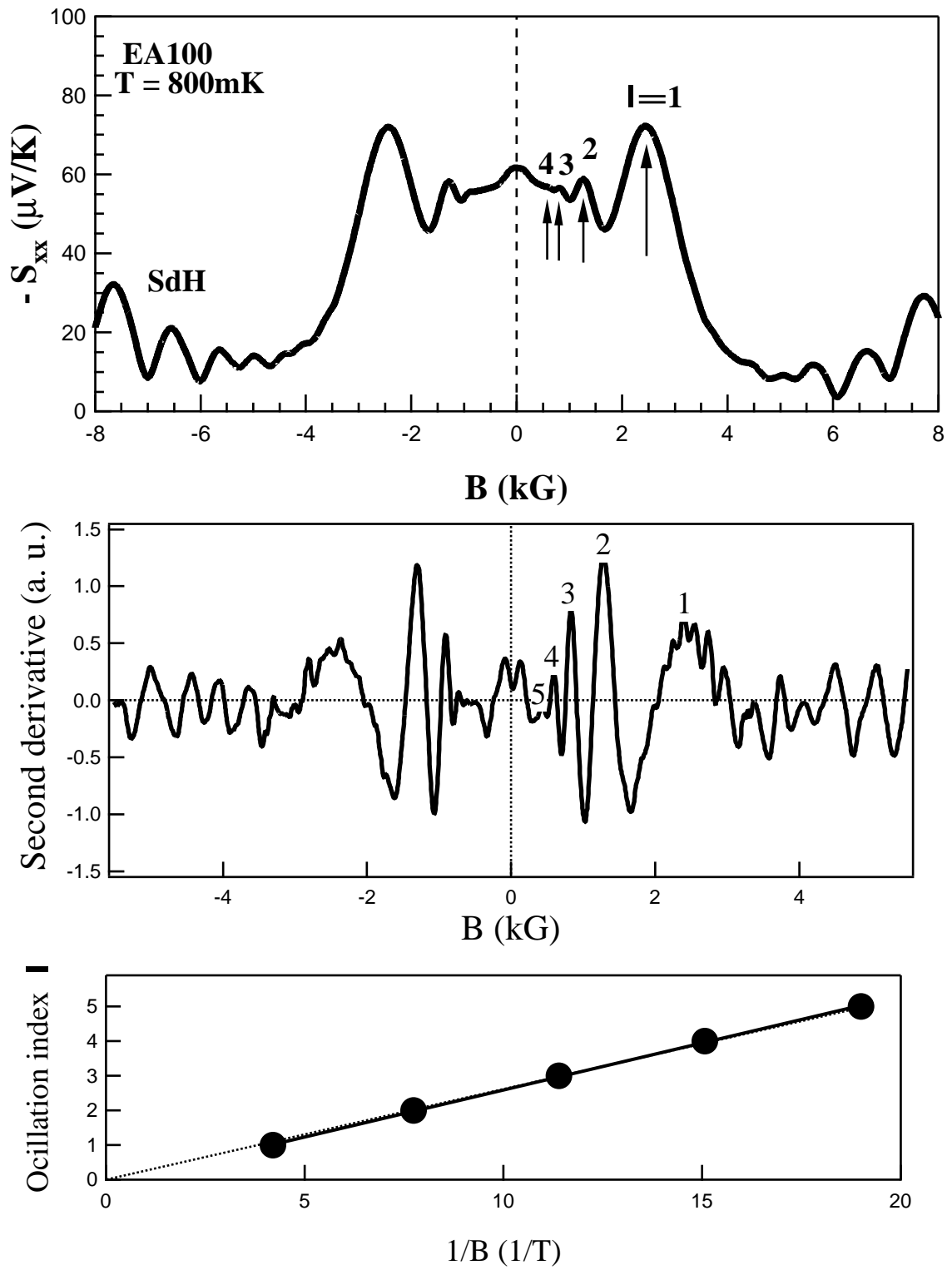
Figure 3.4. New oscillations of TEP at low magnetic field
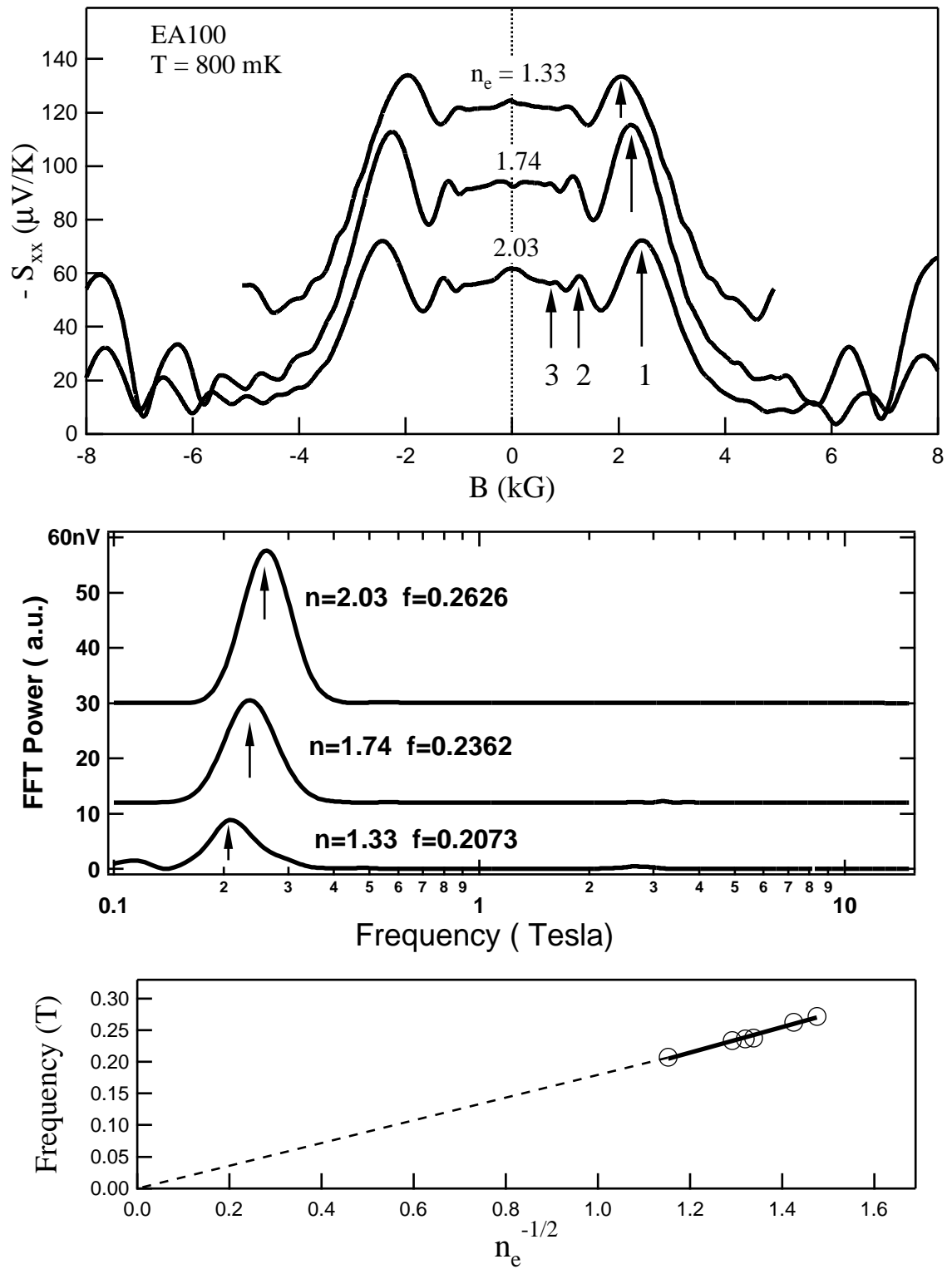
Figure 3.5. Density dependence of the new oscillations
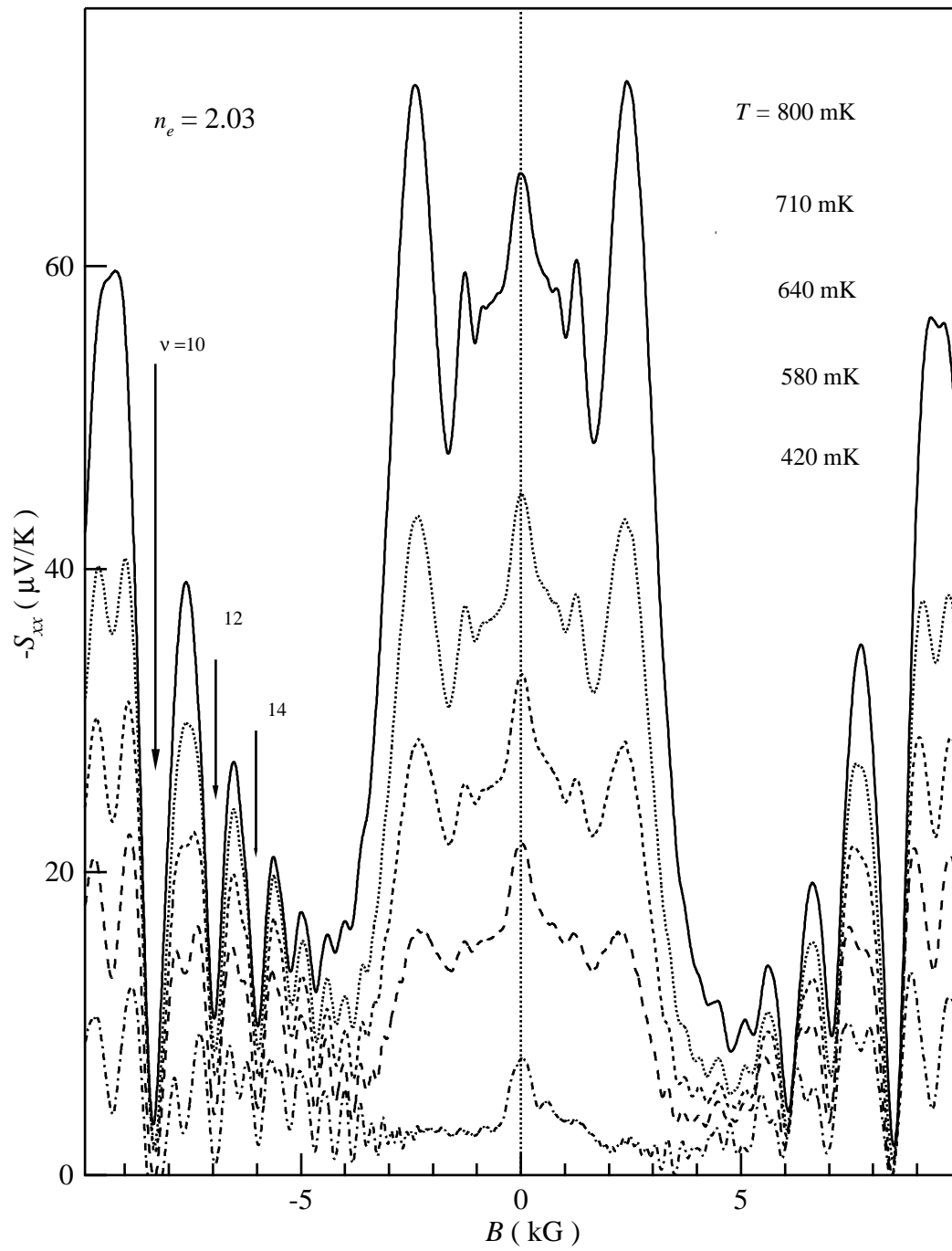
Figure 3.6. Temperature dependence of new oscillations of TEP for EA100

Figure 3.7 shows the temperature dependence of S_0 for three densities. All data show the T^{3-4} dependence, which indicates that the phonon drag mechanism is dominant. This is an essential point that electron-phonon interaction plays an important role in the new oscillation. The absolute values of TEP at zero field are close to the published data [34]. It is observed that the data at $T > 800$mk begin to deviate the T^{3-4} dependence, a phenomenon which is consistent with [34]. In the measurement, even at 900 mK, the temperature gradient is only 13% of the average sample temperature, so there is probably another reason for this deviation.

Figure 3.8 shows the value of resonant peak $(l = 1)$ vs $1/T$ for three densities. All data are fitted very well by $exp(-E/k_BT)/T^2$, which comes from $S_{xx}(B)$ formula

A: n_e=1.33 0.38 $T^{3.5}$

B: n_e=1.74 0.25 $T^{3.3}$

C: n_e=2.03 0.20 $T^{3.6}$
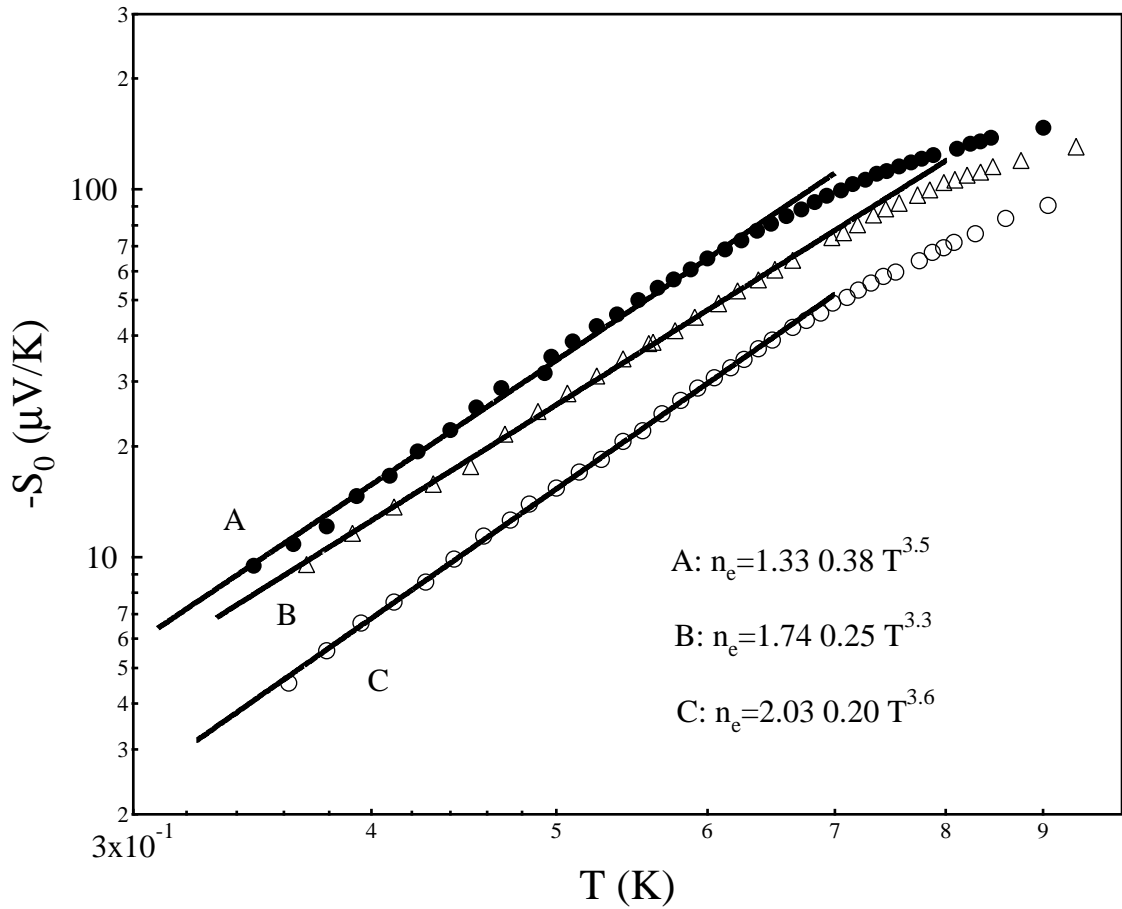
Figure 3.7. Temperature dependence of S_{xx} at $B = 0$ for three densities of EA100

for the inter-LL scattering. E is the resonant phonon energy. The fitted values of E are close to the LL spacing energies ($\hbar\omega_C$) for three densities. This feature suggests that the acoustic magneto-phonon resonance may be responsible for the new oscillations.

Under the close circuit condition, ϵ can be measured by simultaneously measuring the electrical current and the temperature gradient. A similar oscillation at a low magnetic field is observed in Figure 3.9. This oscillation (10%) is not as strong as that of $S_{xx}(B)$ (35%) because ϵ_{xx} not only contains the information of electron-phonon scattering, but also includes the electron-impurity scattering. The
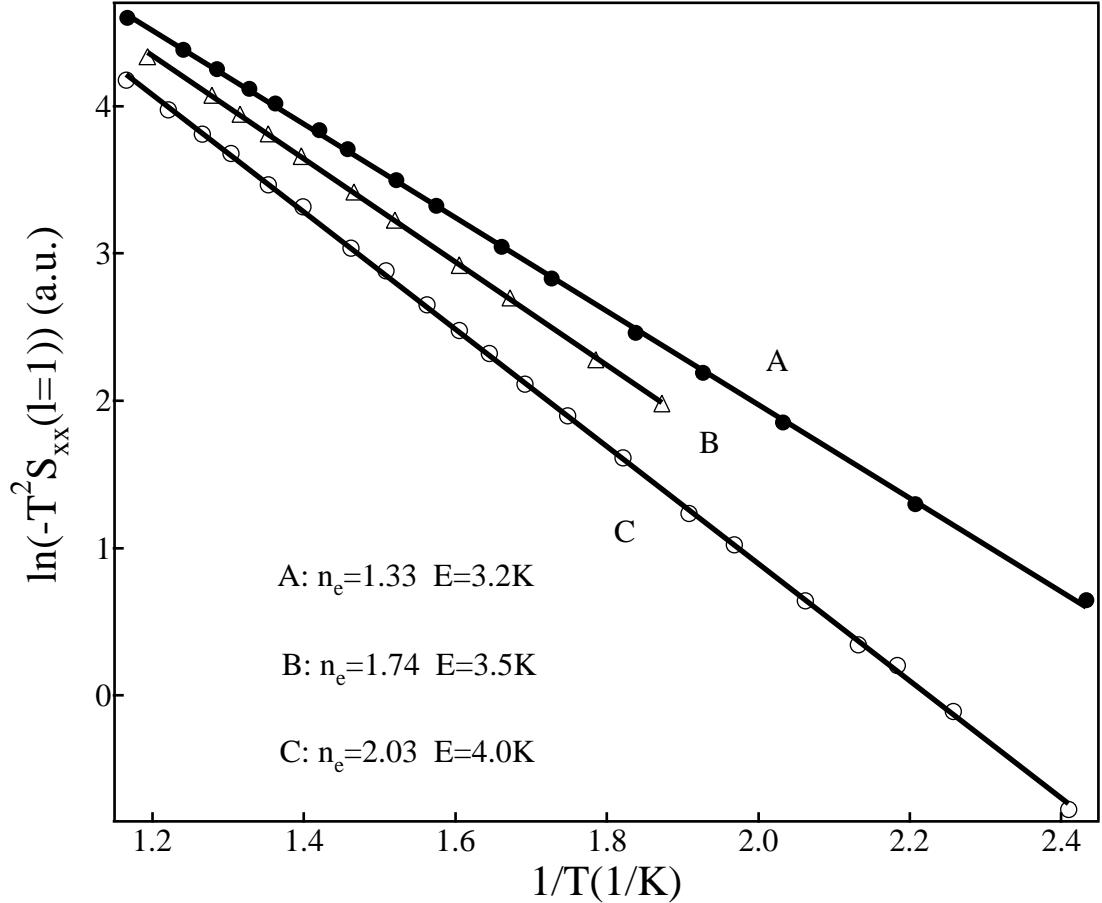
Figure 3.8. Temperature dependence of S_{xx} at $l=1$ for three densities of EA100
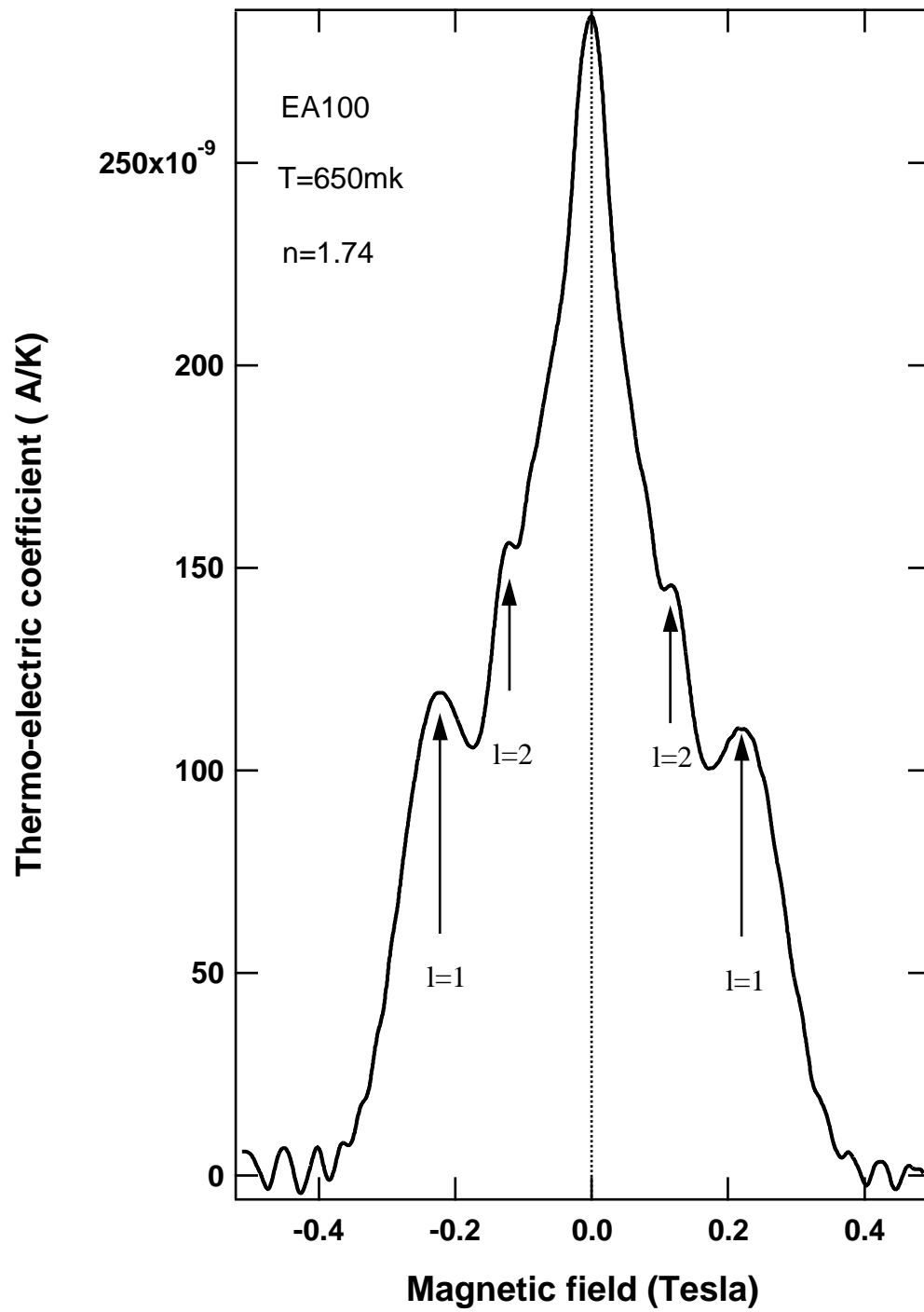
Figure 3.9. New oscillations in thermo-electric coefficient measurement

fast drop of ϵ at higher field is the feature of σ_{xx}, which can be understood from the Drude model.

Can the new oscillations of magneto-TEP be observed at higher temperature (e.g., 4 K) ? Figure 3.10 shows the experimental results at 4 K. Because the sensors are not calibrated in 4 K range, the ∇T data is not available, and the absolute values of S_{xx} are not given. It is interesting that new oscillations can be resolved even at 4 K.

3.3   Experimental data in a low magnetic field for other samples

Besides EA100 sample, EA467 also shows this new oscillation, shown in Figure 3.11. The following features are worth noting:

1). EA467 is a quantum well sample with well width of 35 nm. $n_e \sim 3.4$ and $\mu \sim 3 \times 10^6$. The energy difference between the first subband and the second subband is about 80 K, so there are some electrons in the second subband because of the high density of 3.4. The detailed features of this sample will be given in Chapter 4. Because electrons occupy the second subband, the new oscillations are more complicated. This is a possible reason that there are some extra oscillation peaks in the data. The position of the principle peak is strictly proportional to $\sqrt{n_e}$.

2). The on-set temperature above which the oscillation can be clearly seen is 1200 mK, whereas it is 500 mK for EA100.

3). Comparing with EA100, EA467 has much smaller zero field value. S_0 is not scaled with $n_e^{-3/2}$.

Samples come from Bell Labs are also measured. Figure 3.12 shows one example. The sample has a quantum well (QW) width of 25nm, density of 2.15, and mobility of 12 $\times 10^6$ (which is a factor of 4 higher than EA100). Contacts are made directly on a 8 mm $\times$ 1.5 mm wafer without lithography, so the signal is not symmetrical about zero magnetic field; only the positive TEP data are shown.
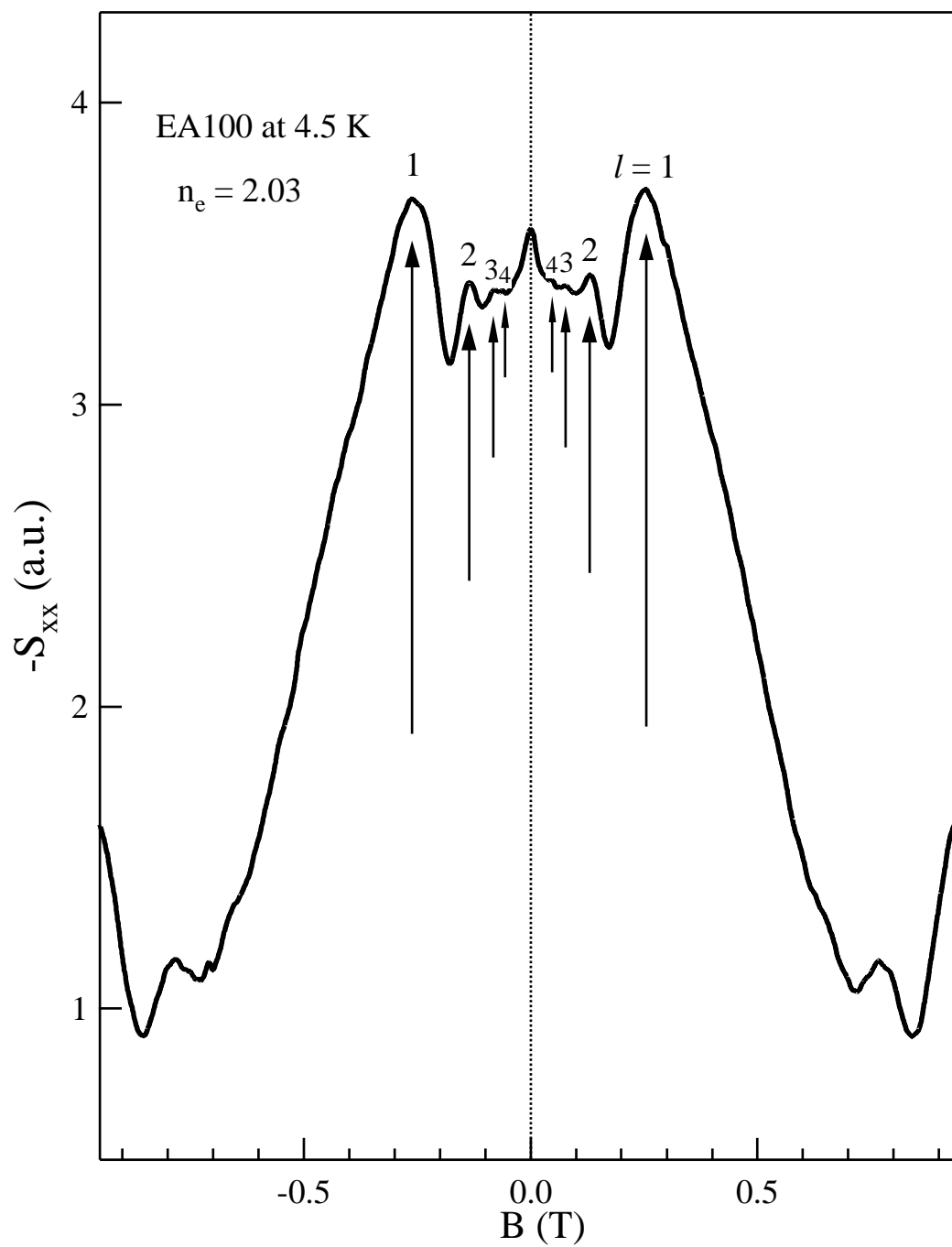
Figure 3.10. New oscillations of TEP at 4.5 K for EA100

Figure 3.11. New oscillations of TEP for EA467

Figure 3.12. New oscillations of TEP for Bell quantum well sample

Figure 3.13 shows the new oscillations in a high-mobility heterojunction from Bell labs. This sample has a low density of 0.93, and a high mobility of 10×10^6. The same features as EA100 are present in this figure. The first peak position is scaled with $\sqrt{n_e}$.

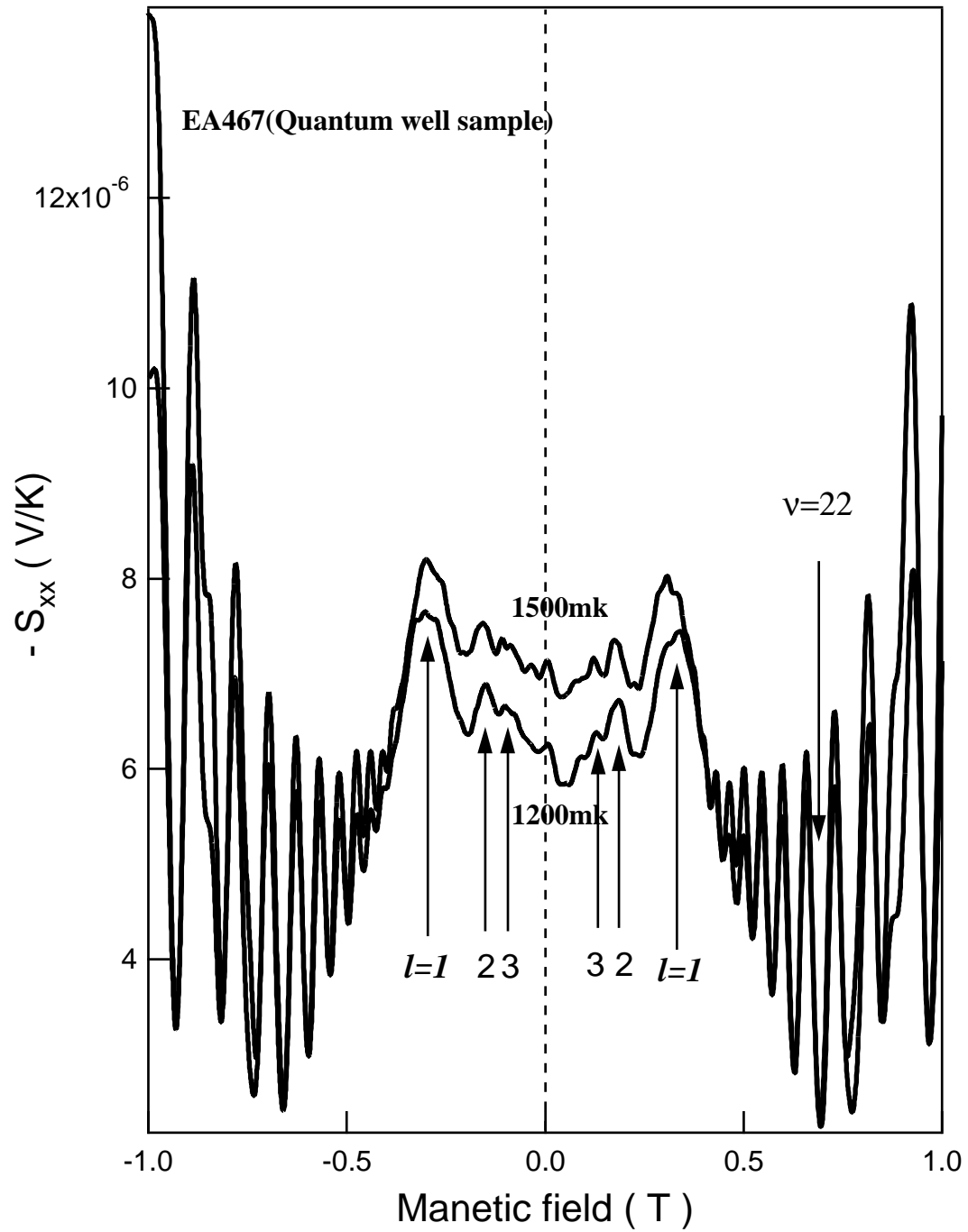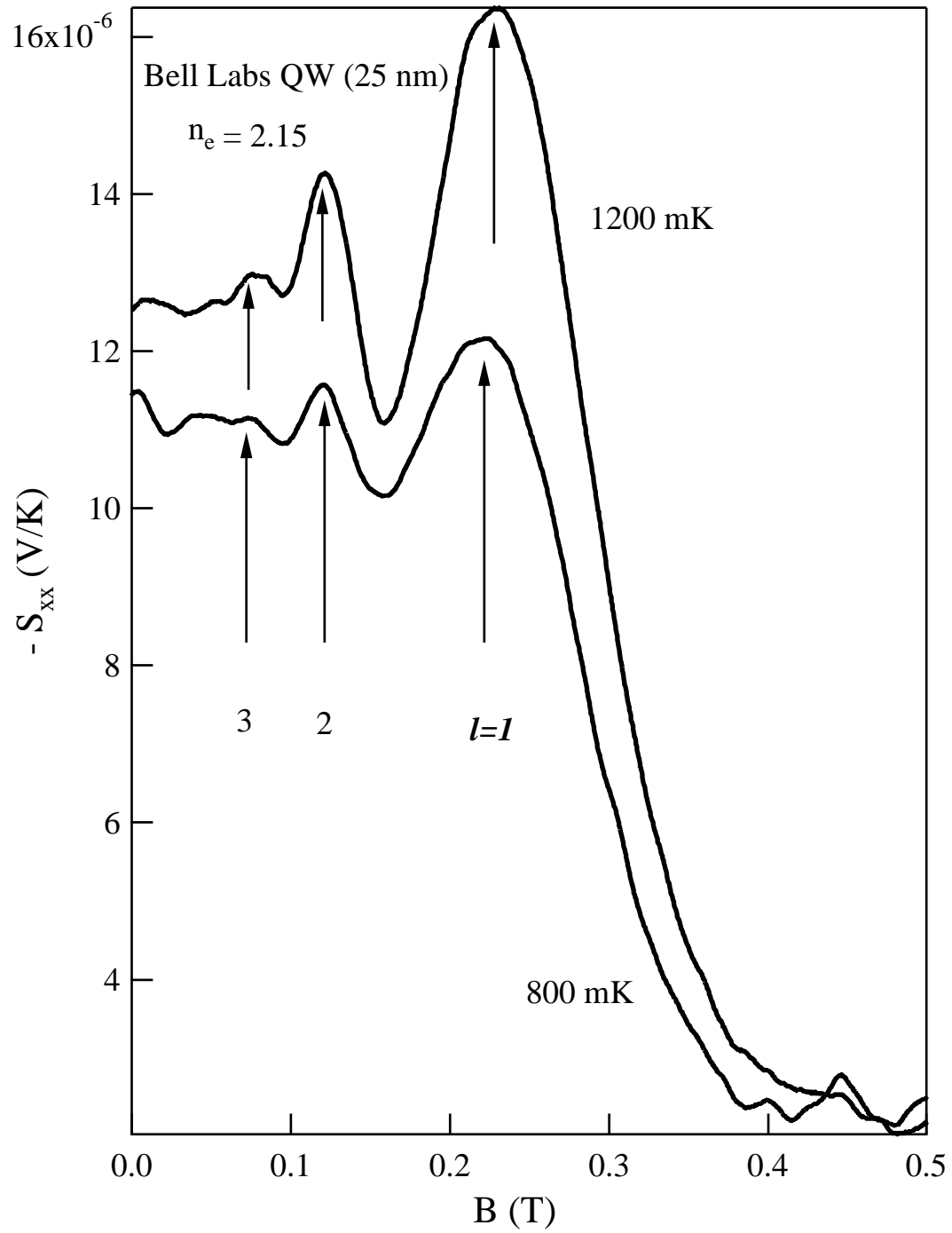From these three sets of experimental data measured from different samples, it is clear that the new oscillations of the magneto-TEP in a low magnetic field are generic in GaAs-AlGaAs 2DEG.

3.4 Theoretical discussion

3.4.1 Acoustic phonon resonance model

From the experimental data, the main features of the TEP oscillations can be summarized as follows:

1) The new oscillation is periodic over $1/B$.

2) The oscillation frequency or the field of the first peak is proportional to $\sqrt{n_e}$. Note that Fermi wave number $k_F = \sqrt{2\pi n_e}$, so the frequency is proportional to k_F.

3) The temperature dependence of zero-field TEP shows that the phonon-drag mechanism is dominant, which indicates the electron-phonon interaction is responsible for this oscillation occurring in a small magnetic field.

4) Fitting to the data of temperature dependence of the first oscillation peak, the excitation behavior is found, which means that electrons jump from the lower Landau level to the higher Landau level by absorbing one phonon. The Fitting excitation energy is also close to the Landau spacing energy at that point.

Considering all experimental evidence, the following scenario emerges: Electrons absorb or emit a phonon and jump to the near Landau level through electron-phonon interaction at a certain magnetic field. This cyclotron resonance results in the maximum of magneto-TEP at that magnetic field point. Only the acoustic phonons participate in the resonant scattering process because the energy scale here is around 4 K. The momentum selection rule is needed to pick up the phonon having the corresponding excitation energy. It is a resonance assumption that only those phonons with wave vector equal to $2k_F$ can effectively interact with electrons.
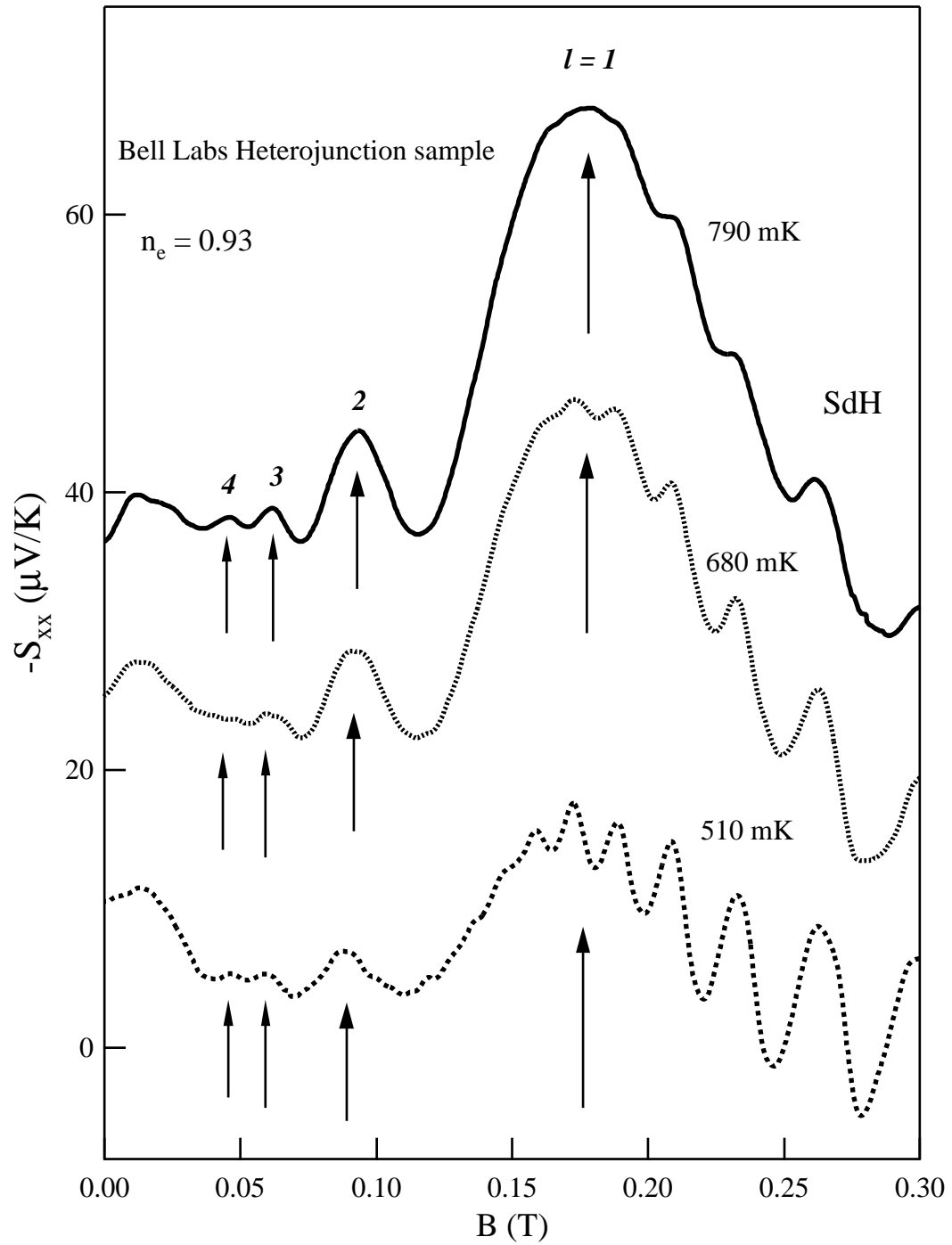
Figure 3.13. New oscillations of TEP for Bell heterostructure sample

The high order oscillation peaks result from the multiple Landau level jumping. So the momentum and energy resonant conditions can be written as follows:

$$q = 2k_F \quad , \tag{3.2}$$

$$\hbar\omega_{qs} = l\hbar\omega_c \quad , \tag{3.3}$$

q is the phonon wave vector and $\hbar\omega_{qs}$ is the phonon energy. l is an integer number for the order of resonant peaks. The linear dispersion relation of the acoustic phonon assumes $\omega_{qs} = uq$, where u is the phonon velocity. The explicit relations revealed by the experimental data can be explained as follows:

$$l = \frac{2m^*u\sqrt{2\pi n_e}}{eB_l} \quad , \tag{3.4}$$

$$f = \frac{2m^*u\sqrt{2\pi n_e}}{e} \quad , \tag{3.5}$$

f is the oscillation frequency, which is obtained from the FFT analysis.

The feature of 4) can be quantitatively understood by the explicit formula of S_{xx}, shown in Equation 2.61.

3.4.2 Explanation of the momentum selection rule

At first, $S_{xx}(B)$ in Equation 2.61 can be simplified by the assumption: the resonant phonons are 2D interface phonons [55], then $q = q_\parallel$. $S_{xx}(B)$ is written as follows:

$$\begin{aligned} S_{xx}(B) &= -\frac{k_B}{e}\frac{\hbar u^2}{(k_BT)^2}\tau_q \sum_{n,l} N_l f_n(1 - f_{n+l}) \times \\ &\quad \times \int_0^\infty dq q^3 \nu(q)\Delta_{n,\ell}(q)\delta(\omega_c l - qu) \quad , \end{aligned} \tag{3.6}$$

where the spectral DOS is approximated as a delta function, and τ_q is the phonon

scattering lifetime determined by the boundary scattering. $\Delta_{n,\ell}(q)$ is the in-plane-momentum conservation factor, which is the overlap integral of electron wave functions of different LLs along the 2DEG plane [56, 35, 55]. $\Delta_{n,\ell}(q)$ is a strongly oscillating function with the magnetic field B. All oscillation peaks have almost the same order of amplitude below a limit or cutoff of B, above this limit $\Delta_{n,\ell}(q)$ is zero. The cutoff means that when two electron wave functions are not overlapped, the scattering probability is zero. The last peak locates at a certain value of the field so as to make $b = (ql_B)^2/2 = 4n$ as long as $n >> 1$ [57] (it could be verified by numerical method). It follows that $q = 2k_F$. Figure 3.14 shows this feature clearly.

In Equation 3.6, δ function forces q to have a linear relation with the magnetic field B after integrating over all q, and q^3 factor is equivalent to B^3. So, sweeping B from zero to first peak position makes $q^3 \Delta_{n,\ell}(q)$ oscillating from small amplitude to maximum amplitude (l=1). If considering Landau level broadening, δ function should be replaced by a Gaussian function, so $q^3 \Delta_{n,\ell}(q)$ has only the last peak left, corresponding with $l = 1$ oscillation peak in experimental trace. This point is shown clearly in Figure 3.15. This is the reason there is a $2k_F$ selection rule, albeit a not very sharp selection rule.

The discussion above shows the explanation of $2k_F$ momentum selection rule based on a 2D interface phonon model. Is it possible that a normal 3D phonon model can still explain the selection rule? The 3D phonon wave vector q can be written as $q_\parallel$ along the 2DEG plane and q_z along the z direction. There is an important argument: in the case of 2D electrons interacting with 3D phonons, only small $q_z \ll q_\parallel$ are important at low temperature due to some angle damping factors in the Equation 2.61, such as the Fang-Howard-Stern confining factor [35, 56] and the Boson distribution function of N_q. The angle damping effect is shown in Figure 3.16. x presents the angle between q and q_z in unit of Radians, $f(x)$ is production of every term depending on angle factor in Equation 2.61, and temperature is at 1K. In this figure, $f(x)$ drops very fast as q deviates from 2D plane. At 15° angle away from the plane, $f(x)$ drops to its half value of its maximum. At this point, q_z is very small, and $q_\parallel$ only deviates from q by 4%. The accurate momentum

$\Delta_{n,n+1}(q)$ --integral of wave function of phonon and electrons

$\Delta_{17,18}(q)$

$$\Delta_{n,n'}(q) \Leftarrow \left| \iint \Phi_{n',k'}(r) e^{iqr} \Phi_{n,k}(r) d^2r \right|^2$$

$$q = k' - k$$
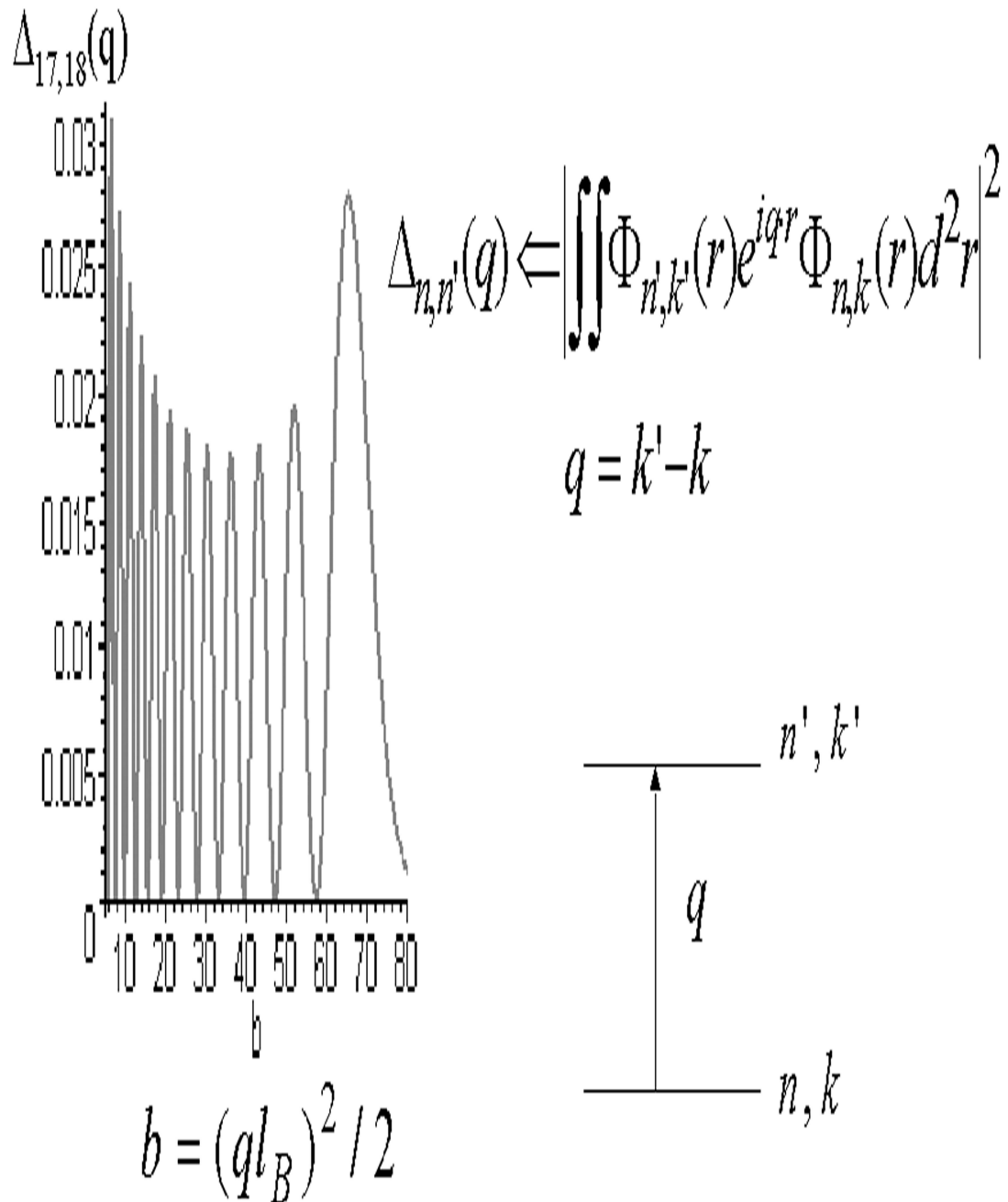
$$b = (ql_B)^2 / 2$$

Figure 3.14. The oscillation and cutoff features of overlap integral function

TEP is proportional to: $q^3 \Delta_{n,n+l}(q)$

$q^3 I_{17,18}(b)$
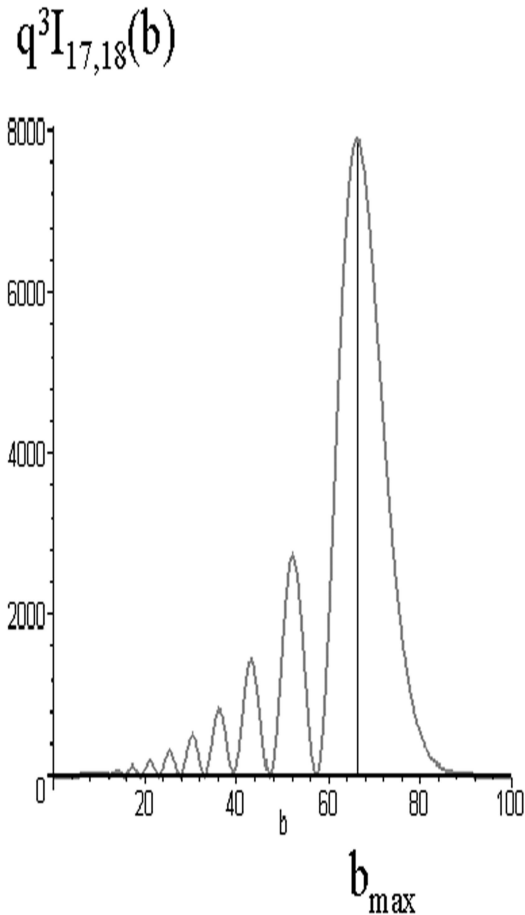
$b_{max} \cong 4n$
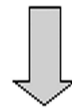
$q = 2k_F$

Larger momentum transfer, i.e., longer jumping distance of guiding center leads to bigger phonon-dragged TEP.

b_{max}

$b = (ql_B)^2/2$

Figure 3.15. $2k_F$ momentum selection rule
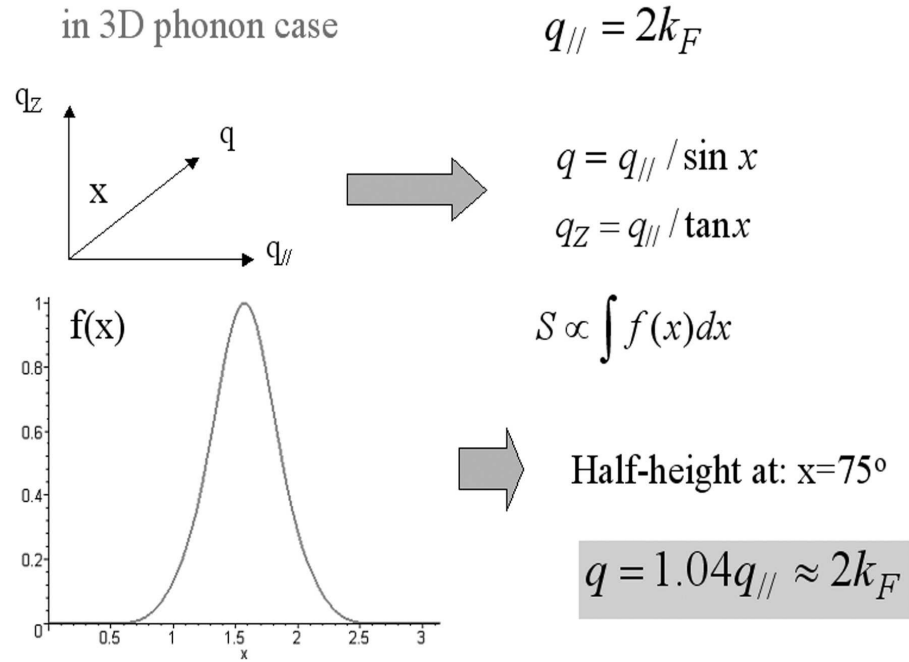
Figure 3.16. The angle damping effect

selection rule should be: $q_\| = 2k_F$. But 4% difference between $q_\|$ and q allows us to approximate 3D phonons to 2D phonons. Even at 4 K, the difference between them at half height point (only around 10 %) is not sufficient to destroy the experimental observation.

In summary, both 2D and 3D phonon models can explain the $2k_F$ momentum selection rule under our experimental conditions.

3.4.3 Numerical calculation

Equation 2.61 has been numerically calculated by Dr. Lyo of Sandia National Labs. The calculated TEP is plotted as a function of B in Figure 3.17, for $\Lambda_{s\mathbf{q}} = 2$ mm and respectively for three densities, 2.03, 1.74, and 1.33. A field-free screening for the electron-phonon interaction is employed. Other parameters are well-known and are given in Ref.[37]. The TEP is proportional to the phonon mean-free-path $\Lambda_{s\mathbf{q}}$, which is basically an adjustable parameter. The thermal conductivity data from the samples yield $\Lambda_{s\mathbf{q}} = 2.8$ mm, which is close to 2 mm
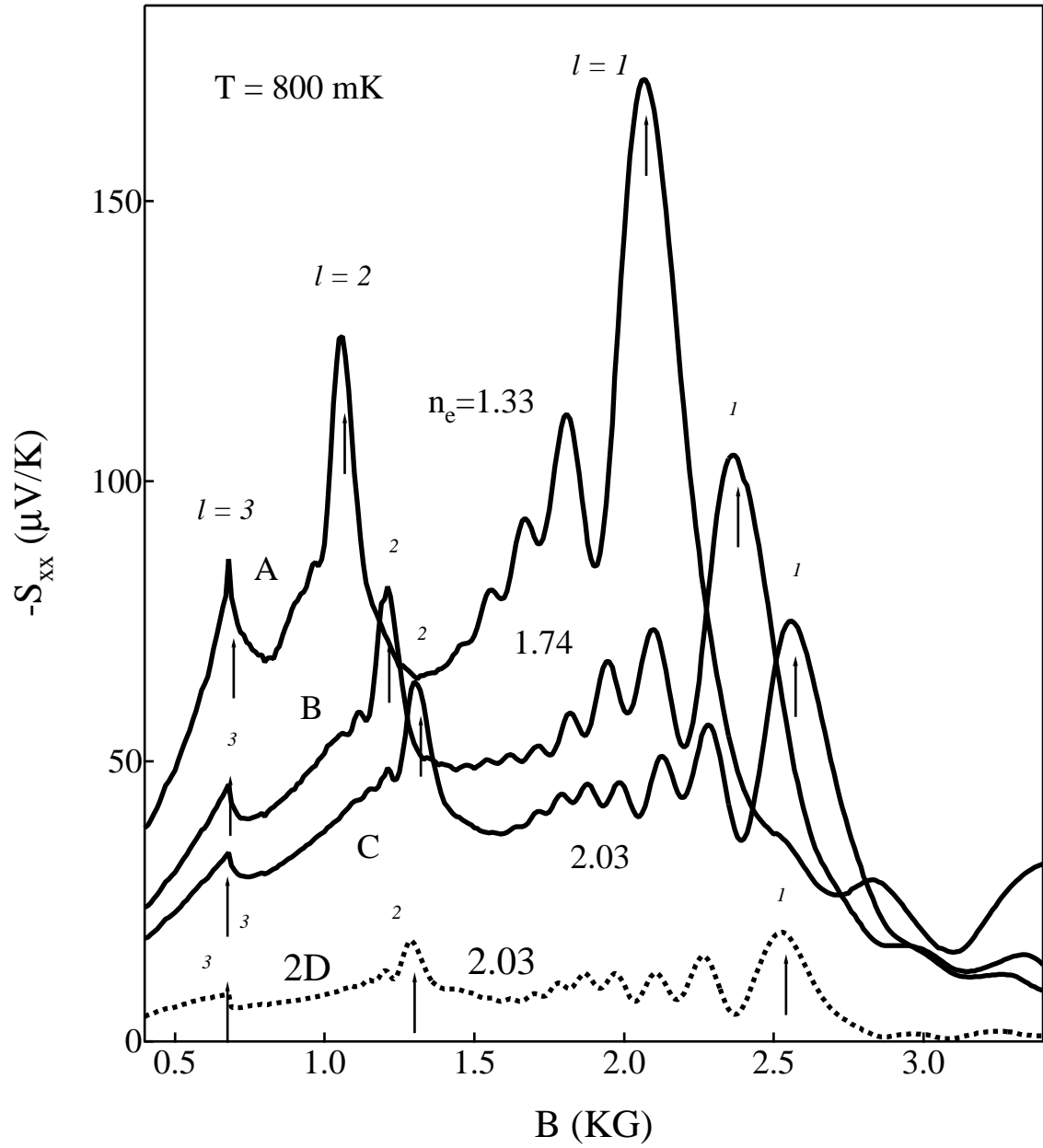
Figure 3.17. Numerical calculation of TEP based on 2D and 3D phonon model

used in the calculation. It is seen that the $\ell = 1, 2, 3, \cdots$ peaks appear on top of the regular SdH oscillations, which are from the phonons with $q_{\parallel} < 2k_F$. Larger Γ makes the peaks broader and the valleys shallower compared to the sharper structures obtained for $\rho_n(\varepsilon) = \delta(\varepsilon - \varepsilon_n)$. A, B and C traces display the TEP as a function of B for three densities $n_e = 1.33, 1.74, 2.03$ at 0.8 K. It is seen that there is an approximate scaling relationship between the peak positions of B, satisfying $B \propto \sqrt{n_e}/\ell$. This relationship is consistent with the inter-LL resonance phonon picture $\hbar\omega_{2k_F} \simeq \ell\hbar eB/m^*$ in view of $\omega_{2k_F} \propto k_F \propto \sqrt{n_e}$, yielding reasonable agreement with experimental data. Numerical results also find $S_{xx} \propto \exp(-E/k_BT)/T^2$ in agreement with Figure 3.8, where it is found that $E \propto \sqrt{n_e}$, close to the transverse $2k_F$ phonon energy. Transverse phonons yield a dominant contribution (~ 70 %) through strong piezoelectric scattering at low temperatures. The calculated background TEP is much lower than the peaks compared with the data in Figure 3.4, probably due to the simplistic non-self-consistent density of states employed in the present low-B situation (where the LLs are closely separated). Also, the magnitude of the calculated TEP keeps decreasing as B approaches $B = 0$ in contrast to the data: below $B < 0.4$ kG, the number of the LLs becomes very large ($n > 100$), requiring a zero-B formalism for a more accurate result.

The 2D phonon modes relevant in the GaAs/Al$_x$Ga$_{1-x}$As heterostructures are the leaky phonons [55, 58] with phonon wave vector component $q_z = 0$ and $q = q_{\parallel}$. The TEP is again given by Equation 2.61 with $\Delta(q_z) \equiv 1$ with the summation on q_z replaced by the summation over the leaky modes. For a rough estimate, the same $|V_{s\mathbf{q}}|$ is assumed with the effective sample volume given by $\Omega = S\ell_p$, where S is the cross section of the well and ℓ_p is roughly the penetration depth of the mode. The result for the 2D phonons is compared with that of the 3D phonons in Figure 3.17 for $\ell_p = 200$ Å using a pair of longitudinal and transverse modes. The B dependence of S_{xx} from the 2D phonons is very similar to that from the 3D phonons, except that it is slightly shifted to lower B. The similarity between the results from the 2D and 3D phonons is numerically confirmed to hold at higher temperatures (e.g., 4 K).

In conclusion, numerical calculation confirms our explanation of $2k_F$ momentum selection rule given above, shows qualitatively the main features of experimental observation, and has reproduced the absolute values close to the experimental data. Both the 2D and 3D phonon model can account for this new oscillation.

3.4.4   Discussion

Some interesting problems should be mentioned here:

1). In Figure 3.7, the linear contribution $S_0 \propto T$ from the diffusive TEP is absent at $B = 0$. The data are similar to the data of Tieke *et al.* [34], but different from the results of Ruf *et al.* [47], in which the diffusive TEP is already visible at 0.6 K and the data deviate from the T^3 slope at 0.6 K. Also, the excellent fitting in Figure 3.8 indicates a lack of intra-LL scattering contribution to the $l = 1$ resonant peak. The fast drop of $S_{xx}(B)$ beyond the first resonant peak is consistent with a cutoff for inter-LL scattering beyond that point.

2). A discrepancy exists between the experimental and the calculations: there is a dip feature between oscillation peaks in experimental data, whereas the calculated data do not show this feature no matter how parameters are adjusted.

3). Both 3D and 2D phonon models can in principle explain this oscillation. However, the peak positions should be affected by 3D mode. For the 3D phonon model, the first resonant peak position should shift to higher field as T goes up, because the resonant 3D phonon energy will be larger due to increasing contribution from q_z as T increases. We have observed this phenomenon in the EA100 sample in the low temperature range of 0.3 K-1 K, but not in the high temperature range of 1 K-4 K. No conclusion can be made at this point.

CHAPTER 4

THERMOPOWER IN A HIGH MAGNETIC FIELD

In the previous chapter, the interesting magneto-TEP data are presented at low magnetic field ($B < 0.5$ T). In a high magnetic field, the integer and fractional quantum Hall states were observed in thermopower data [40, 41, 39, 47, 42, 37, 36, 59, 48]. Major attention has been devoted also to the one-half state ($\nu = 1/2$). In particular, the similarity of temperature dependence of TEP at $B = 0$ and $\nu = 1/2$ [44, 46, 60, 34, 61] strongly supports the Composite Fermion model. In this chapter, the TEP data at a high magnetic field will be presented. Similar features are shown in our data. Besides, two anomalous peaks at $\nu = 2/3, 3/5$ have been observed at $T > 700$ mK, which is not understood at this point.

4.1 General features of thermopower in a high magnetic field

Figures 4.1 and 4.2 show the thermopower data in a high magnetic field for the heterojunction sample (EA100) and the quantum well sample (EA467) respectively. At integer filling factors ($\nu = 1, 2, 3, 4, 5$), TEP reaches a value close to zero, which are correspondent to integer quantum Hall states in magnetoresistance measurement. Nonzero or even negative TEP can be observed at certain intervals around these filling factors. This phenomenon is frequently observed in different samples. The nature of these anomalies are not understood at this point. At fractional filling factors ($\nu = 5/3, 4/3, 2/3, 3/5, 4/7$), corresponding dips in TEP can be clearly seen, indicating the fractional quantum Hall states.

At half filling factors, in particular at the lowest Landau level, such as $\nu = 1/2, 3/2$, MR of the high-mobility samples (such as EA100 and 467) always shows
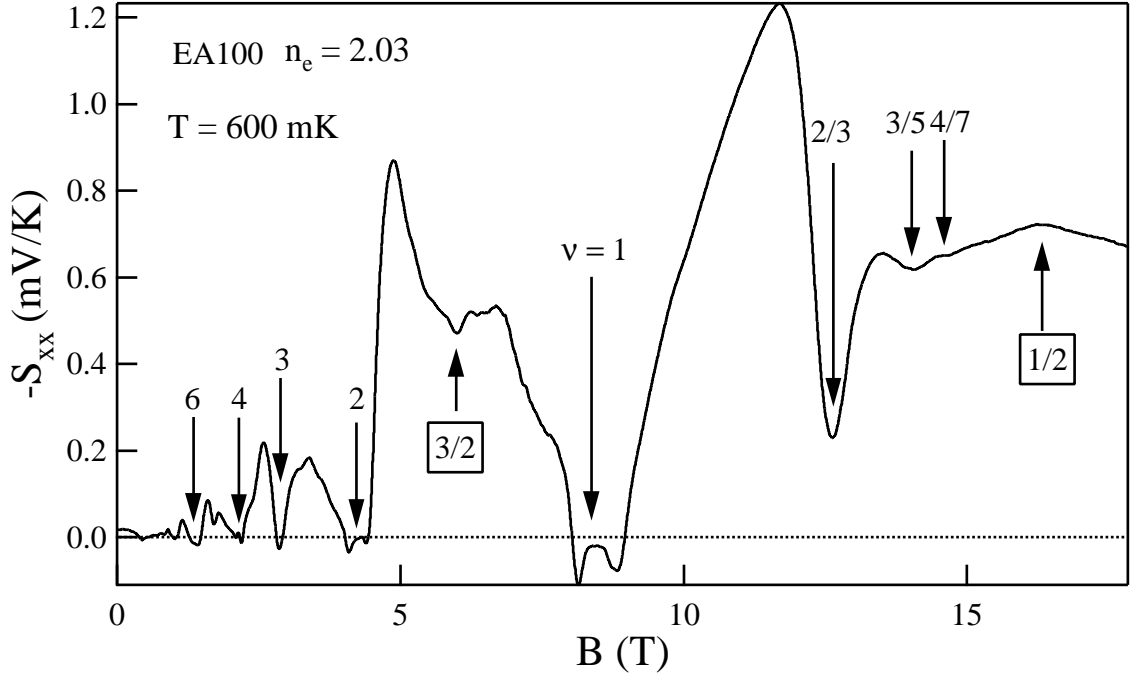
Figure 4.1. Overview of TEP for EA100 in a high magnetic field

the minimum features at 500 mK. From our data and other papers [48, 44, 46, 34], the TEP at $\nu = 1/2$ is a maximum. At $\nu = 3/2$, the situation is not clear; EA100 shows minimum, but EA467 shows the plateau feature, whereas the data in Reference [46] show a local maximum. The maximum feature is easily understood because the DOS is maximum at half filling factors.

4.2 Anomalous peaks of TEP at $\nu = 2/3, 3/5$

4.2.1 BellHSH sample

The BellHSH sample is made from a GaAs/AlGaAs heterojunction grown at Bell labs. It has an electron density of 2.4 and high mobility of 12×10^6 after LED illumination at 2 K. No Hall bar pattern is made on the TEP sample (8 mm$\times$1.5 mm). Contacts are made directly on the edge of the sample.

Figures 4.3 and 4.4 show the TEP signals of V_{xx} ($S_{xx} = \nabla V_{xx}/\nabla T$) in a dilution refrigerator and in a high magnetic field (10 T-18 T). Figure 4.3 shows only the
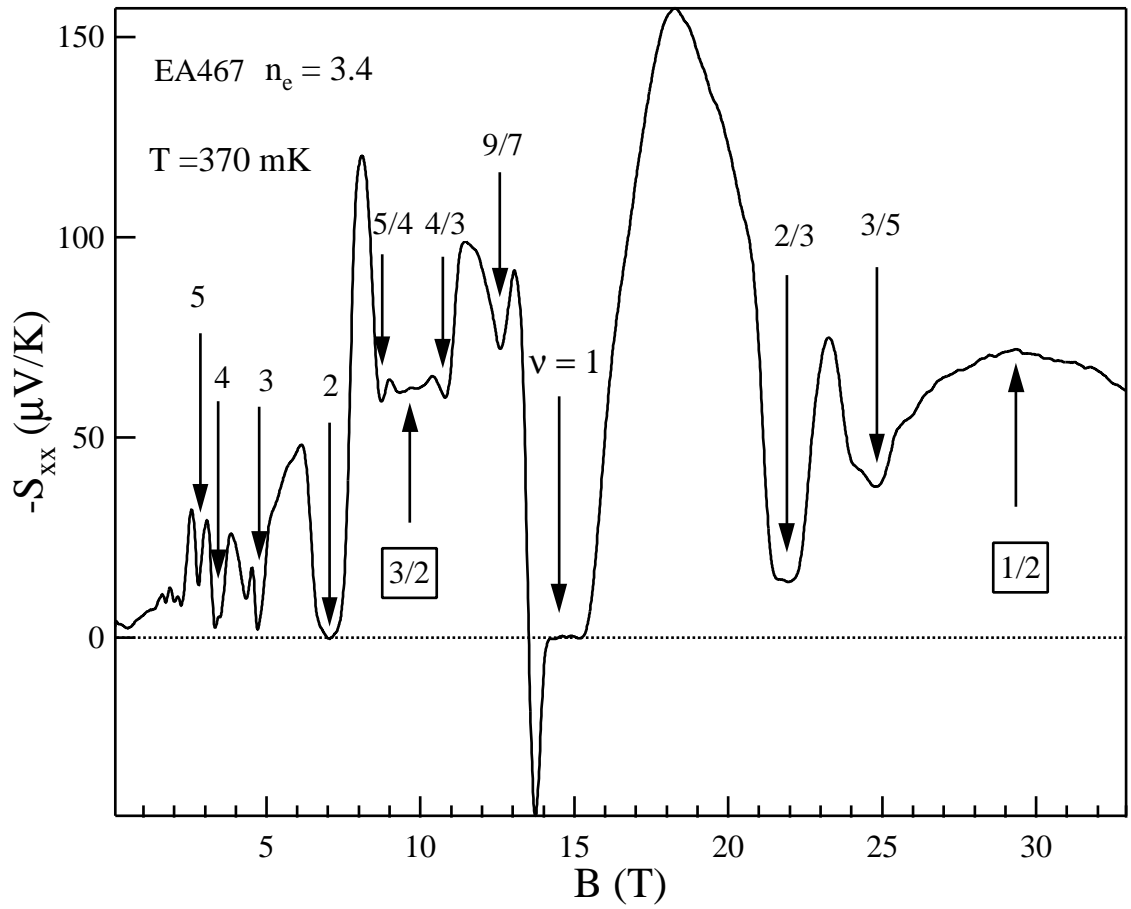
Figure 4.2. Overview of TEP for EA467 in a high magnetic field
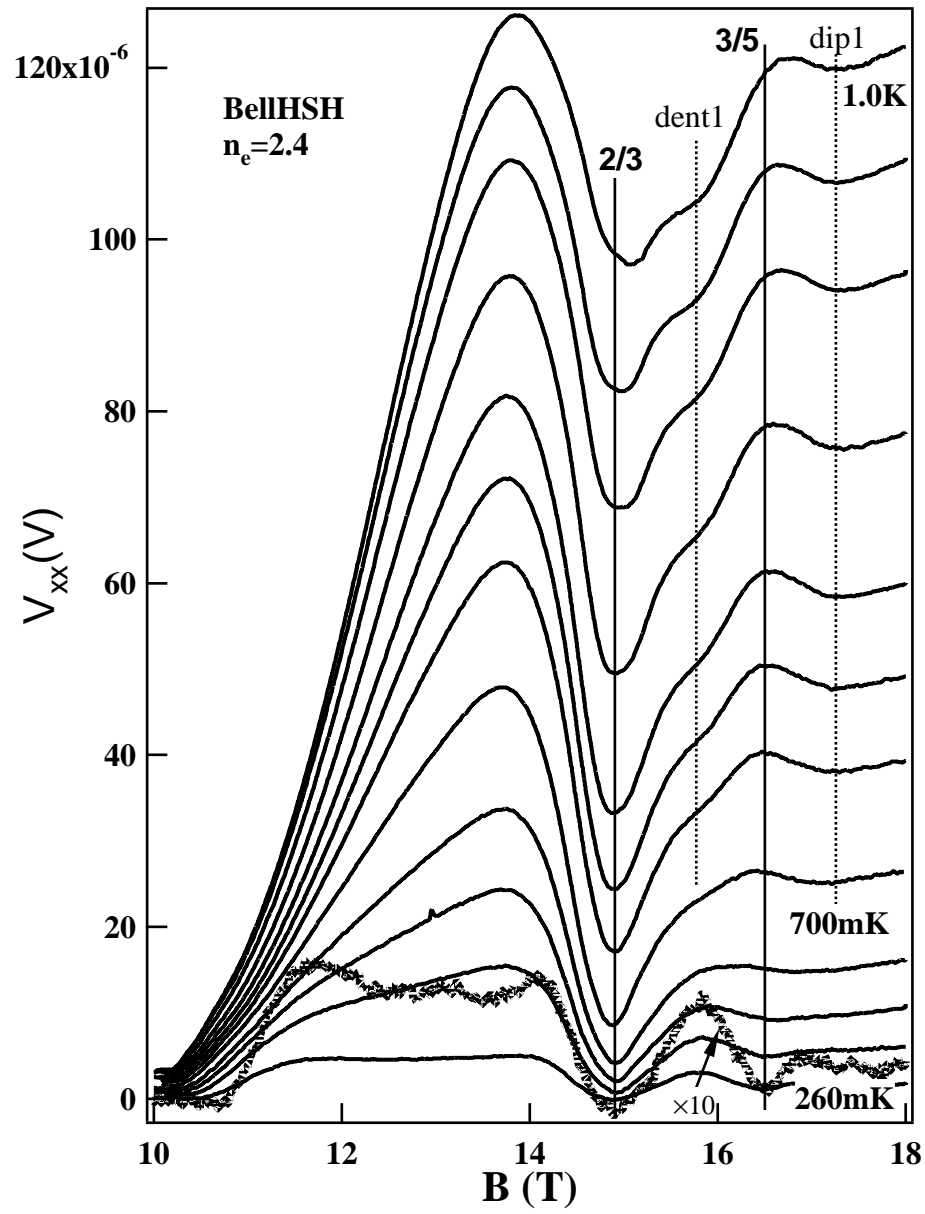
Figure 4.3. Anomalous peaks of TEP for BellHSH at low temperature in a high magnetic field
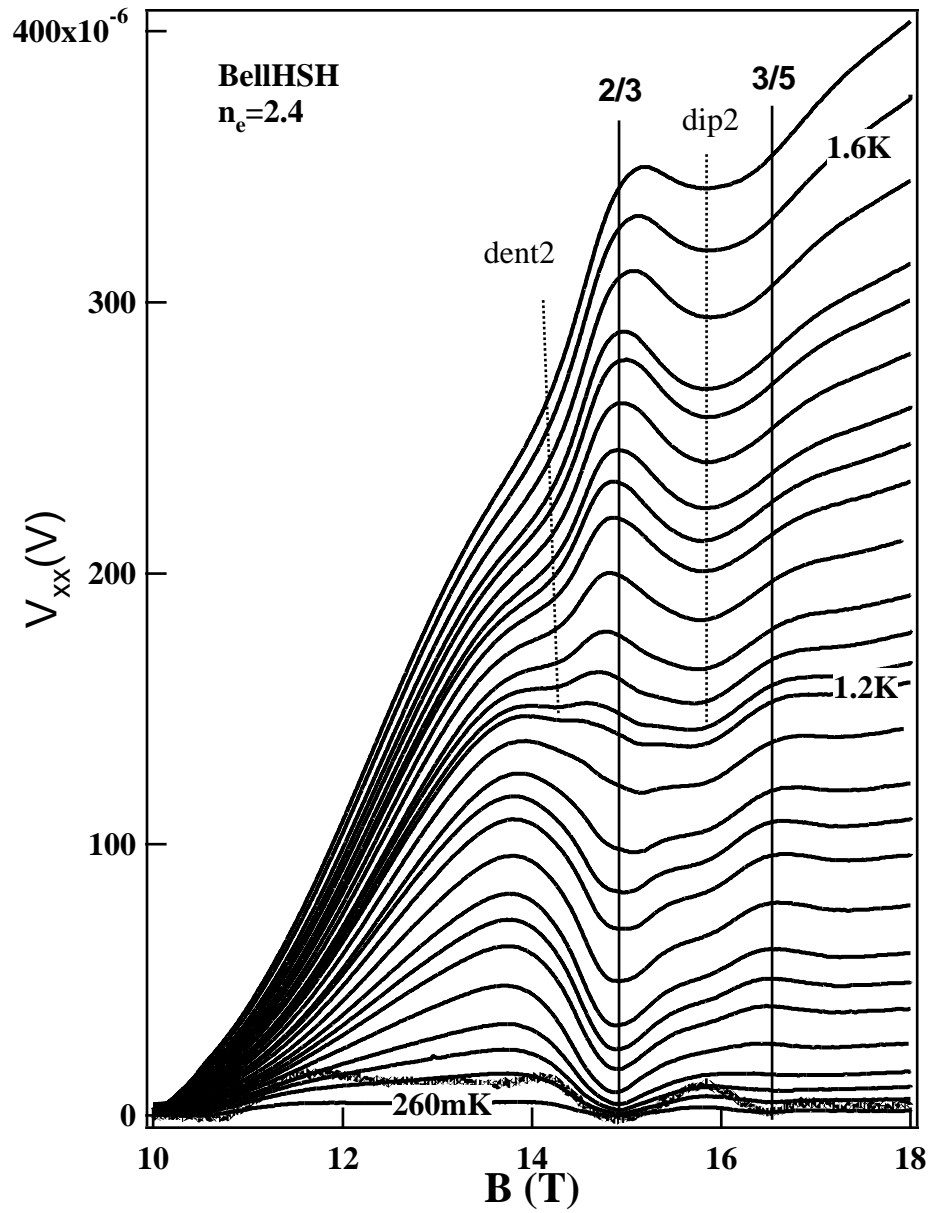
Figure 4.4. Anomalous peaks of TEP for BellHSH in a high magnetic field

portion of data at lower temperature (260 mK-1.0 K) for clarity. The dotted trace is from the lowest temperature (260 mK), and its amplitude has been multiplied by 10, on which the incompressible FQH states at $\nu = 2/3, 3/5$ are clearly shown. For several lower temperature traces, at $\nu = 1$ (located around 9.9 T) and $\nu = 2/3, 3/5$, V_{xx} is close to zero. As T goes up, the dip at $\nu = 3/5$ disappears gradually, then changes to a peak (above 700 mK), while the dent feature on the left (labeled as "dent1") and the dip feature on the right (labeled as "dip1") have been developed. Generally, all the dip and peak features should be smeared out as T goes up [40, 48]. However, at $T > 700$ mK, a new peak appears at $\nu = 3/5$, and becomes stronger as T approaches 1.0 K. Furthermore, dent1 and dip1 features (dotted lines) have been developed. This is the reason why the peak feature at $\nu = 3/5$ is anomalous. The dotted line labeled by "dent1" separates the minimum feature around 2/3 from the peak feature around 3/5.

The higher temperature traces (up to 1.6 K) have been added into Figure 4.4. Similar to Figure 4.3, the anomalous peak feature at $\nu = 2/3$ has been developed after 1.2K. Meanwhile the dent ("dent2") and dip ("dip2") features are shown up. Some observations should be pointed out. First, the anomalous peak at $\nu = 3/5$ disappears gradually above 1.0 K, so do the dip1 and dent1 features. Second, the anomalous peak position at 2/3 shifts to higher field as T increases. Third, in general, from 10 T to 18 T, the trace should have monotonous slope shape; the peak at $\nu = 2/3$ lies above the monotonous background and produces dent2 and dip2 features. Dent2 feature shows the different temperature dependence on the two sides of the dotted line. Above 1.8 K, the peak feature at $\nu = 2/3$ disappears gradually, which can been seen from the top trace.

These data point to an interesting feature which has no counterpart in magnetoresistance at these filling factors: at low enough temperature, a minimum shows in TEP at filling factor $\nu = 2/3$ (also at 3/5), and this minimum evolves into a maximum at high temperature. More data in different cases will be presented to show these features.

4.2.2 BellQW35nm sample

BellQW35nm sample is a GaAs-$Al_{0.3}Ga_{0.7}As$ quantum well (width 35 nm) from Bell labs. It has an electron density of 2.3 and high mobility of 15 $\times 10^6$ at zero magnetic field (no LED). No Hall bar pattern is made on the TEP sample (8mm×1.5mm). Contacts are made directly on the edge of the sample.

Figures 4.5 and 4.6 show the TEP signal of V_{xx} ($S_{xx} = \nabla V_{xx}/\nabla T$) in a high magnetic field (10 T-18 T) using a dilution refrigerator. The BellQW35nm sample shows here the same features as BellHSH sample. Two anomalous peaks at $\nu = 2/3, 3/5$ can be clearly seen in Figures 4.5 and 4.6.

4.2.3 BellHSL sample

The BellHSL sample is a GaAs-$Al_{0.3}Ga_{0.7}As$ heterojunction Bell labs. It has an electron density of 0.93 and a high mobility of 10 $\times 10^6$ by LED illumination at 2 K. No Hall bar pattern is made on the TEP sample (8mm×1.5mm). Contacts are made directly on the edge of sample.

Figure 4.7 shows the TEP signal of S_{xx} in a magnetic field (5 T-11 T) in a ^{3}He refrigerator. Because the density is very low, the positions at $\nu = 2/3, 3/5$ are located at lower field, comparing with BellHSH sample. The energy gaps of The BellHSL sample at these fractional filling factors are relatively small and could be smeared out easily at the measurement temperatures.

The anomalous peak at $\nu = 2/5$ is clear; however, it is less clear about the peaks at $\nu = 2/3, 3/5$. Also the minima showing at $\nu = 7/11, 5/13$ somewhat complicate the situation.

4.2.4 EA100 sample

As mentioned before, EA100 is a heterojunction sample from Sandia National Labs. A Hall bar geometry is lithographically defined. After saturated LED, a density of 2.03 and a mobility of 3 $\times 10^6$ can be obtained.

Figure 4.8 shows the TEP data of the sample EA100 at a density of 2.03 measured in a dilution refrigerator and up to 18 T magnetic field. The same
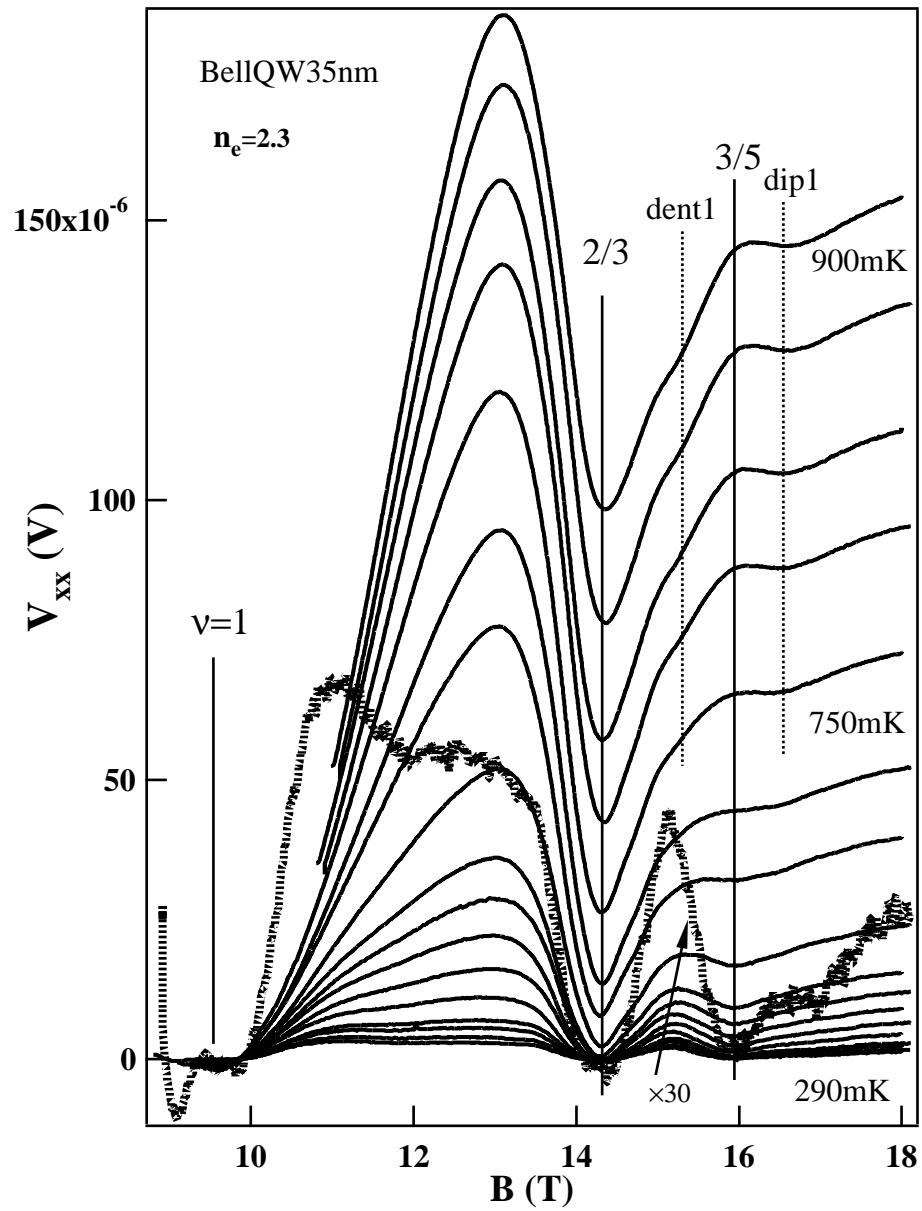
Figure 4.5. Anomalous peaks of TEP for BellQW35nm at low temperature in a high magnetic field

Figure 4.6. Anomalous peaks of TEP for BellQW35nm in a high magnetic field

Figure 4.7. Anomalous peaks of TEP for BellHSL in a magnetic field

Figure 4.8. Anomalous peaks of TEP for EA100 in a high magnetic field

features as that of BellHSH and BellQW35nm samples can be clearly seen. The anomalous peaks locate at the exact positions of $\nu = 2/3$ and $3/5$.

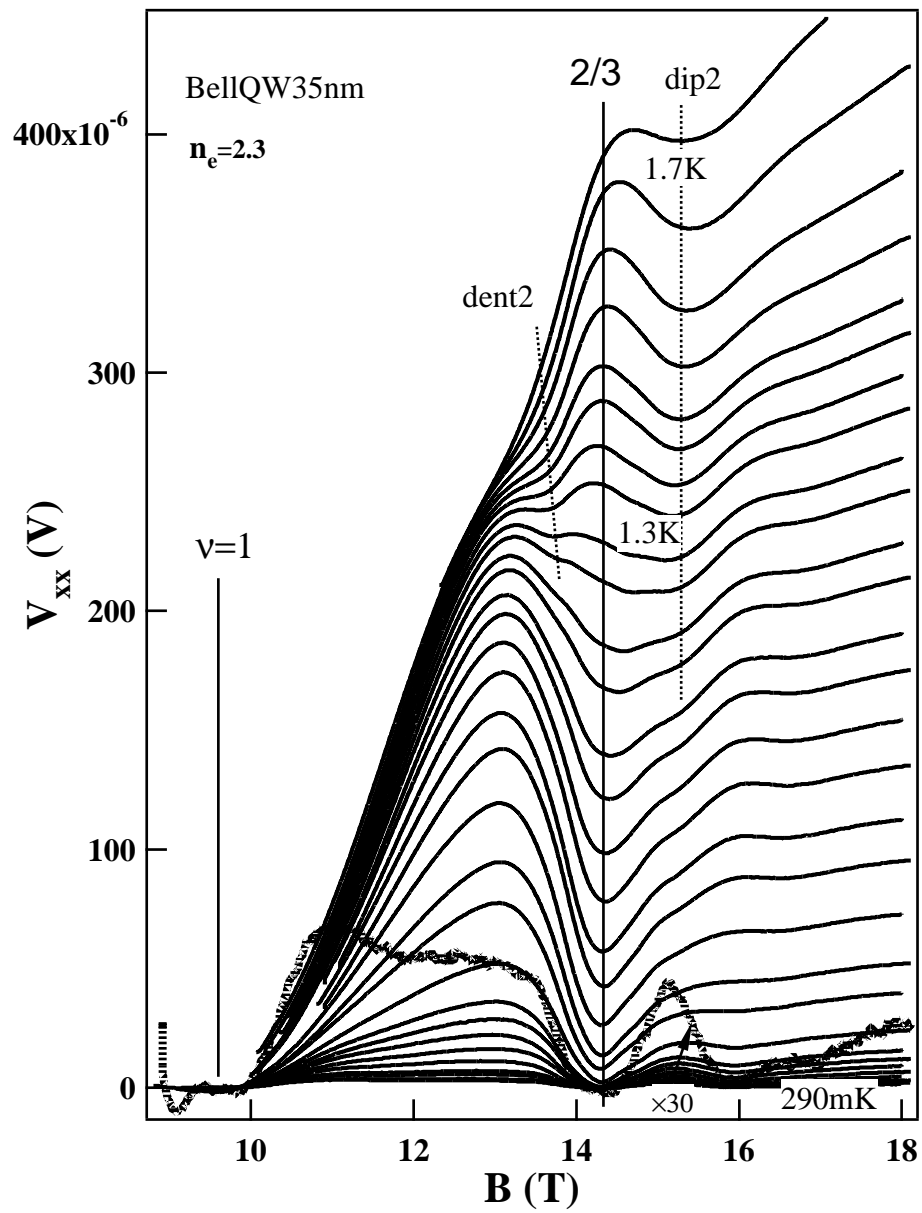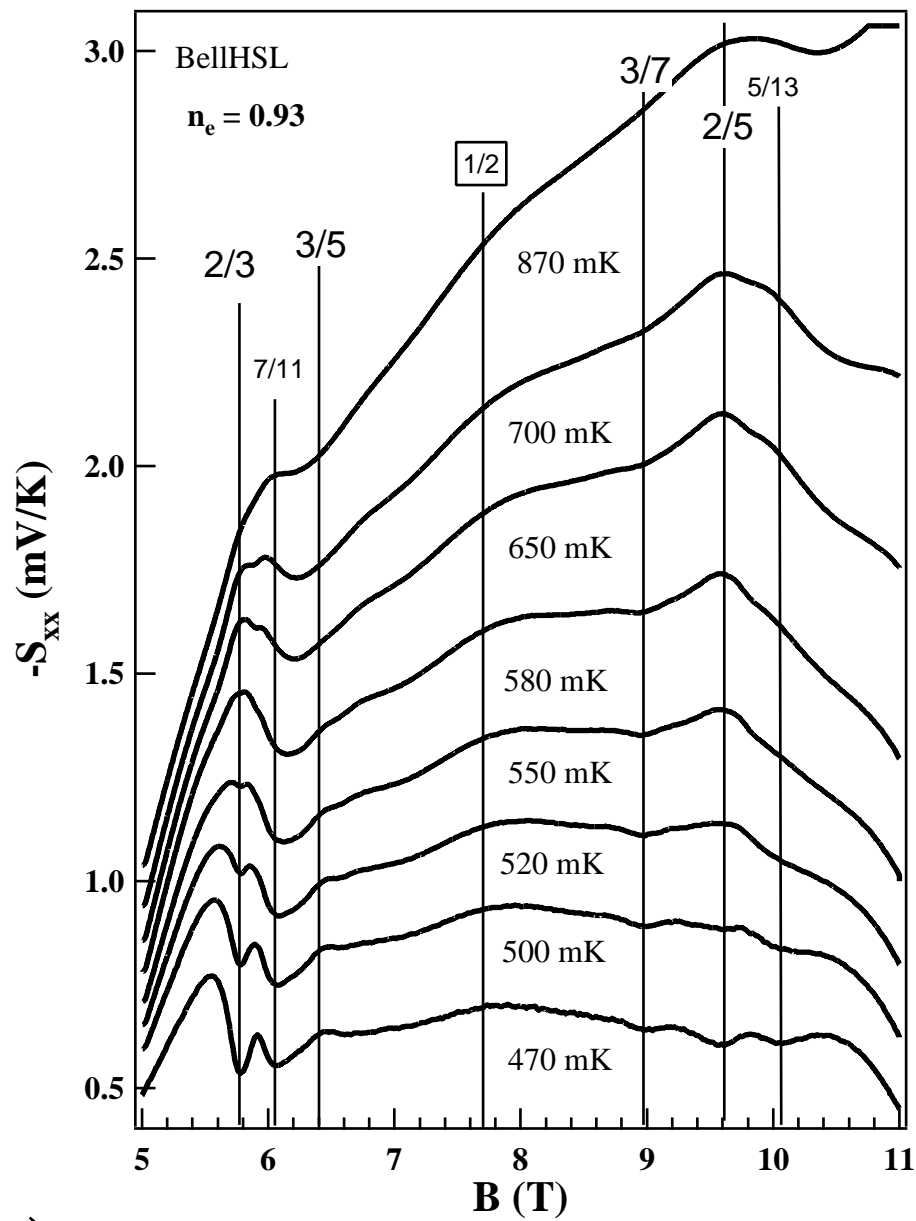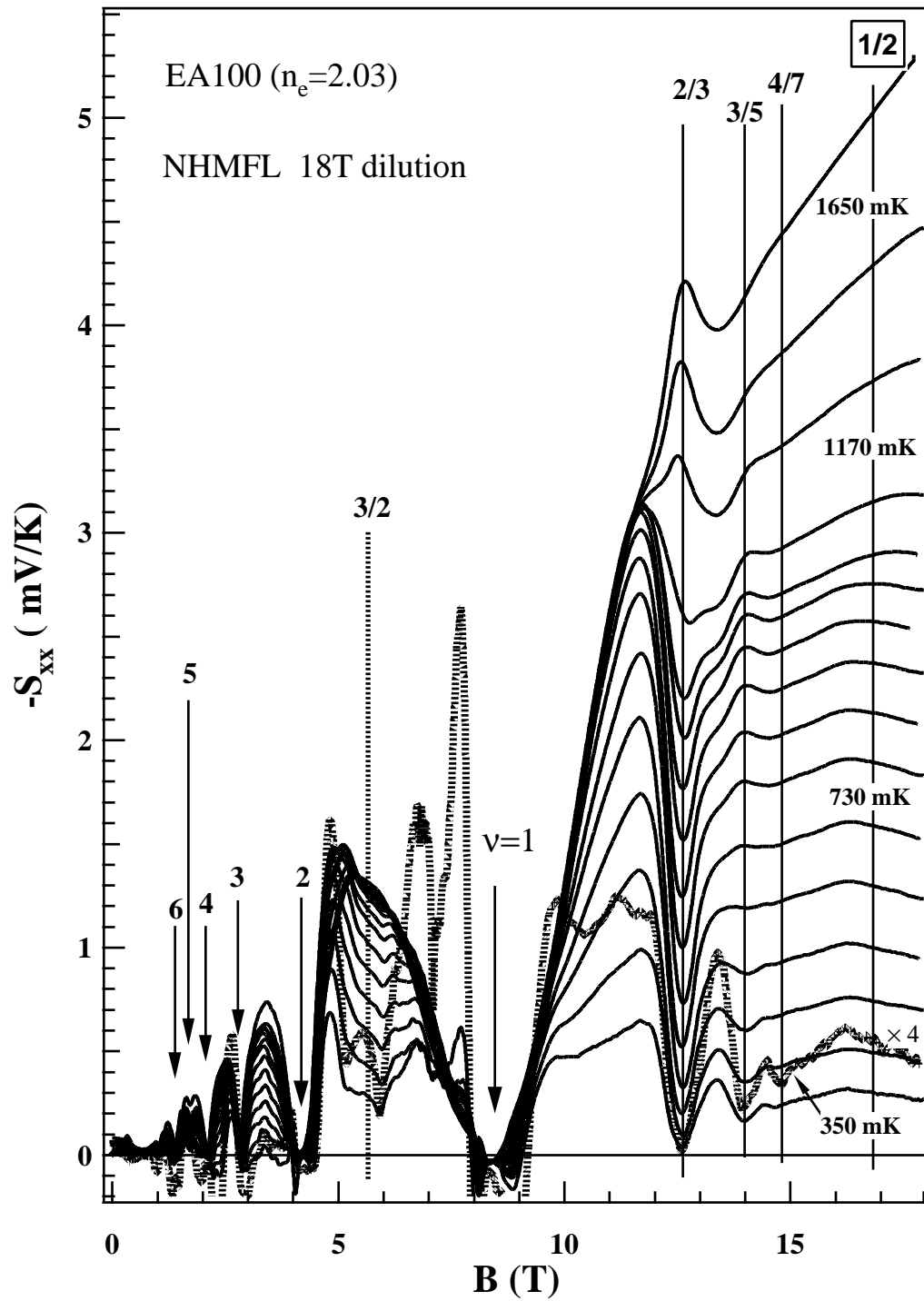## 4.3 Temperature dependence of TEP in a high magnetic field

4.3.1 Temperature dependence of TEP close to $\nu = 1/2$

Figure 4.9 shows the temperature dependence of TEP of the BellHSH sample at 18 T, close to $\nu = 1/2$ (19.8 T). The fitting results in $T^{3.2}$ suggest that phonon-drag mechanism is dominant at this temperature range for the BellHSH sample. There are no features above 16 T, so the temperature dependence at 18 T and 19.8 T should be similar. The sample BellQW35nm has a similar temperature dependence, shown in Figure 4.10.

Figure 4.11 shows the temperature dependence of TEP of the BellHSL sample at $\nu = 1/2$. The fitting results in $T^{3.0}$ suggest that phonon-drag mechanism is again dominant at this temperature range for the BellHSL sample. The sample EA100 has the same temperature dependence, shown in the Figure 4.12. The deviation from the T^3 fitting above 1 K is a general feature for all samples studied. Similar deviation has been reported in zero field temperature dependence [34].

4.3.2 Activation behavior at $\nu = 2/3, 3/5$

Figure 4.13 shows the temperature dependence of TEP at $\nu = 2/3$ and $\nu = 2/5$ for the EA100 sample. The best fitting results can be obtained using the formula $S_{xx} \propto exp(-\Delta/k_B T)/T^2$, much like the temperature dependence of the low field oscillation peak in Chapter 3. This temperature dependence feature shows activation behavior. The power law or simple exponential formula do not fit into the experimental data. The fitted activation energies are $\Delta \sim 4.6$ K at $\nu = 2/3$ and $\Delta \sim 3.5$ K at $\nu = 3/5$. Above 1.6 K, S_{xx} shows saturated behavior and then drops down as T goes up further. Very similar temperature dependence features are observed for all other samples (*i.e.*, BellHSH, BellQW35nm, and BellHSL), which can be seen in Figures 4.14, 4.15, and 4.16. The fitted activation energies

Figure 4.9. Temperature dependence of TEP close to $\nu = 1/2$ for BellHSH

Figure 4.10. Temperature dependence of TEP close to $\nu = 1/2$ for BellQW35nm

Figure 4.11. Temperature dependence of TEP at $\nu = 1/2$ for BellHSL

Figure 4.12. Temperature dependence of TEP at $\nu = 1/2$ for EA100

Figure 4.13. Temperature dependence of TEP at $\nu = 2/3, 3/5$ for EA100
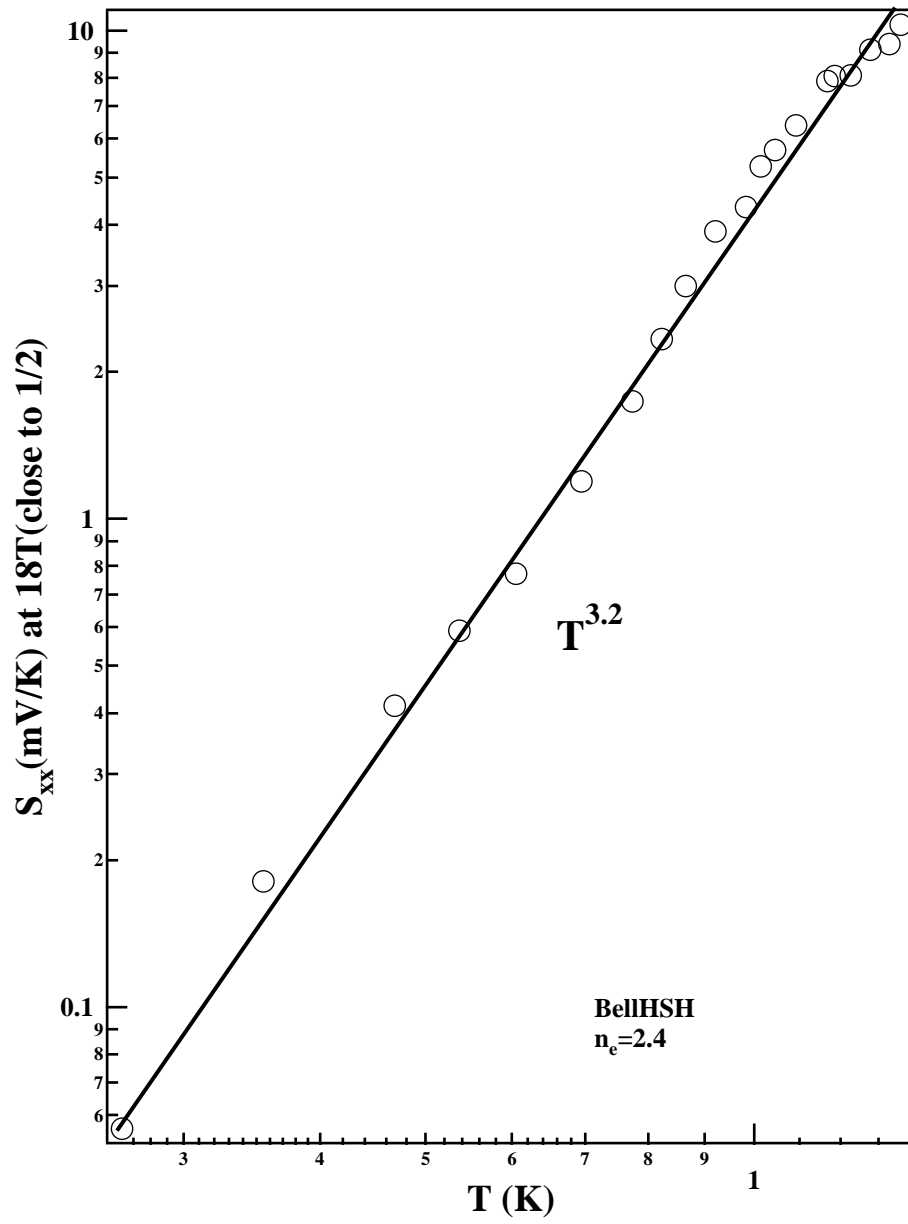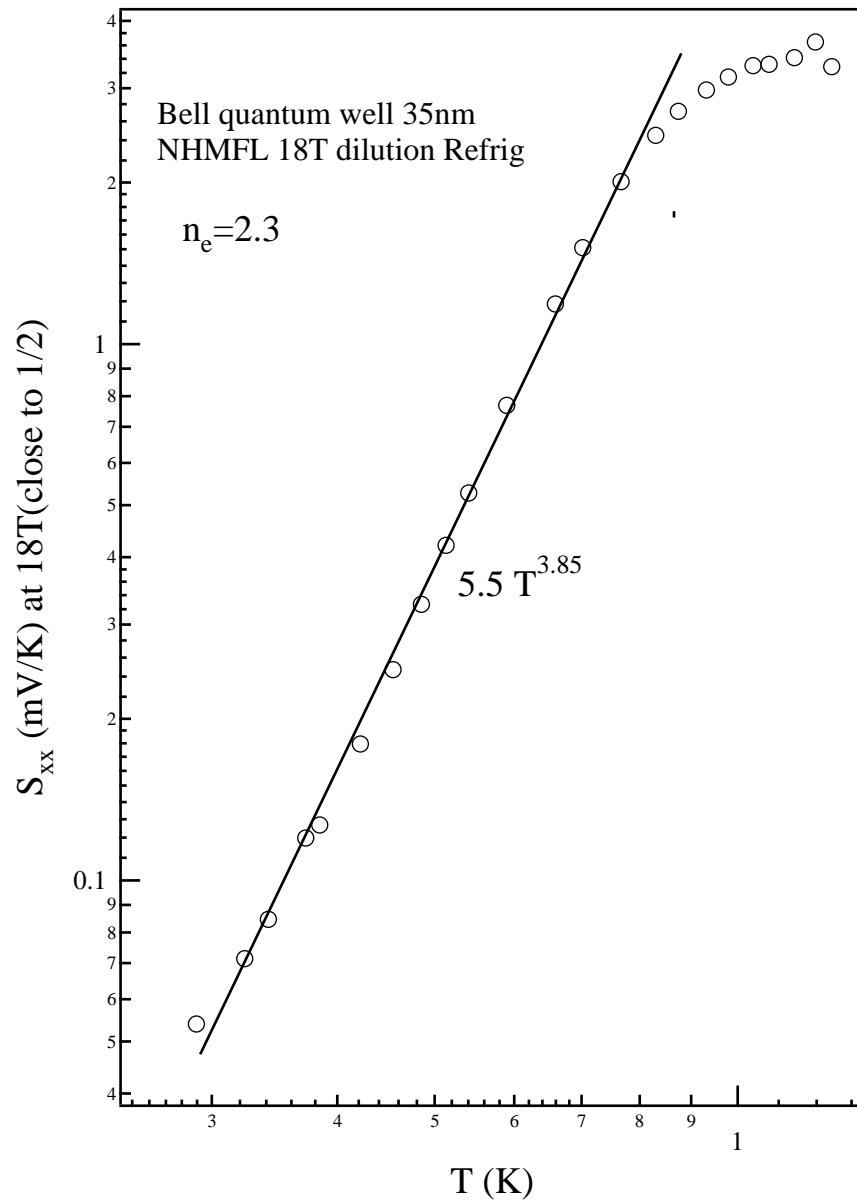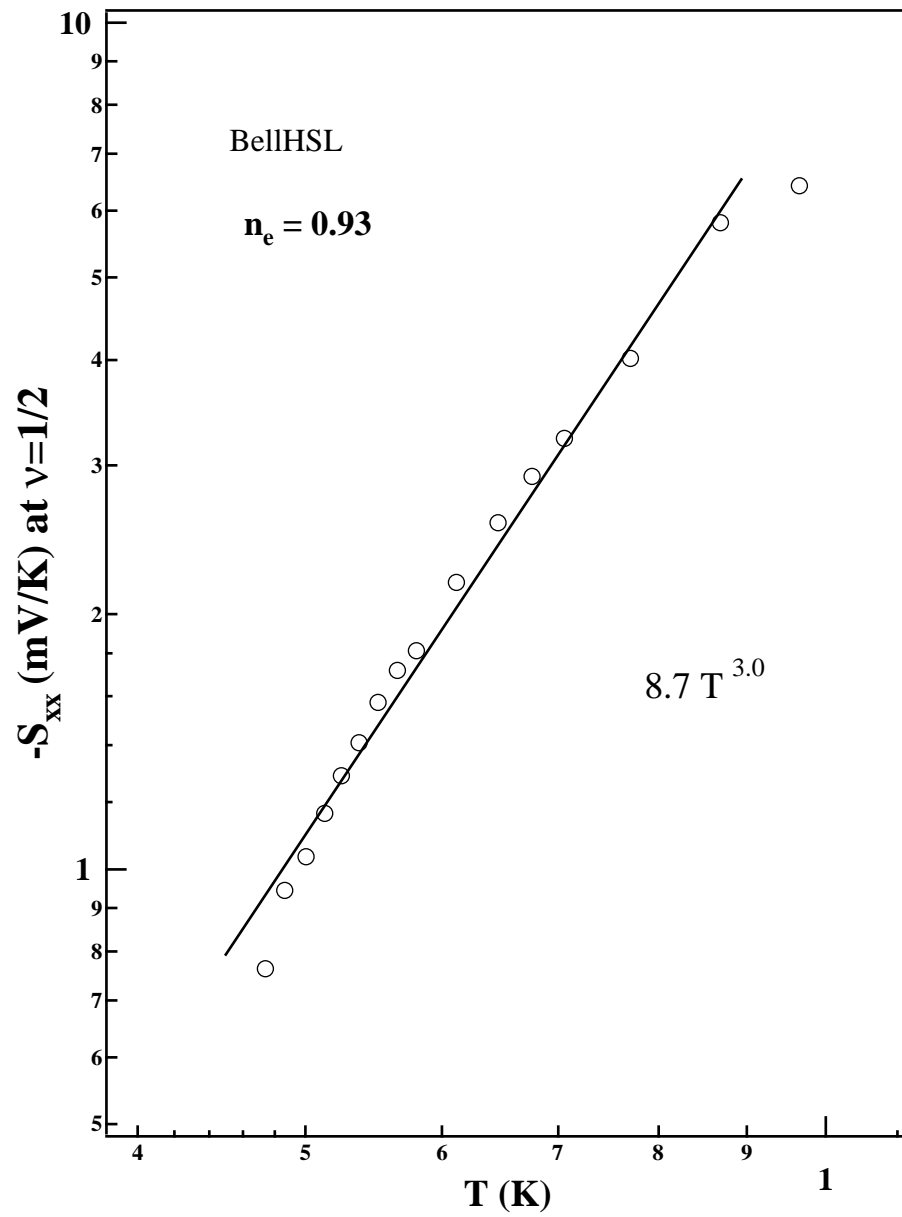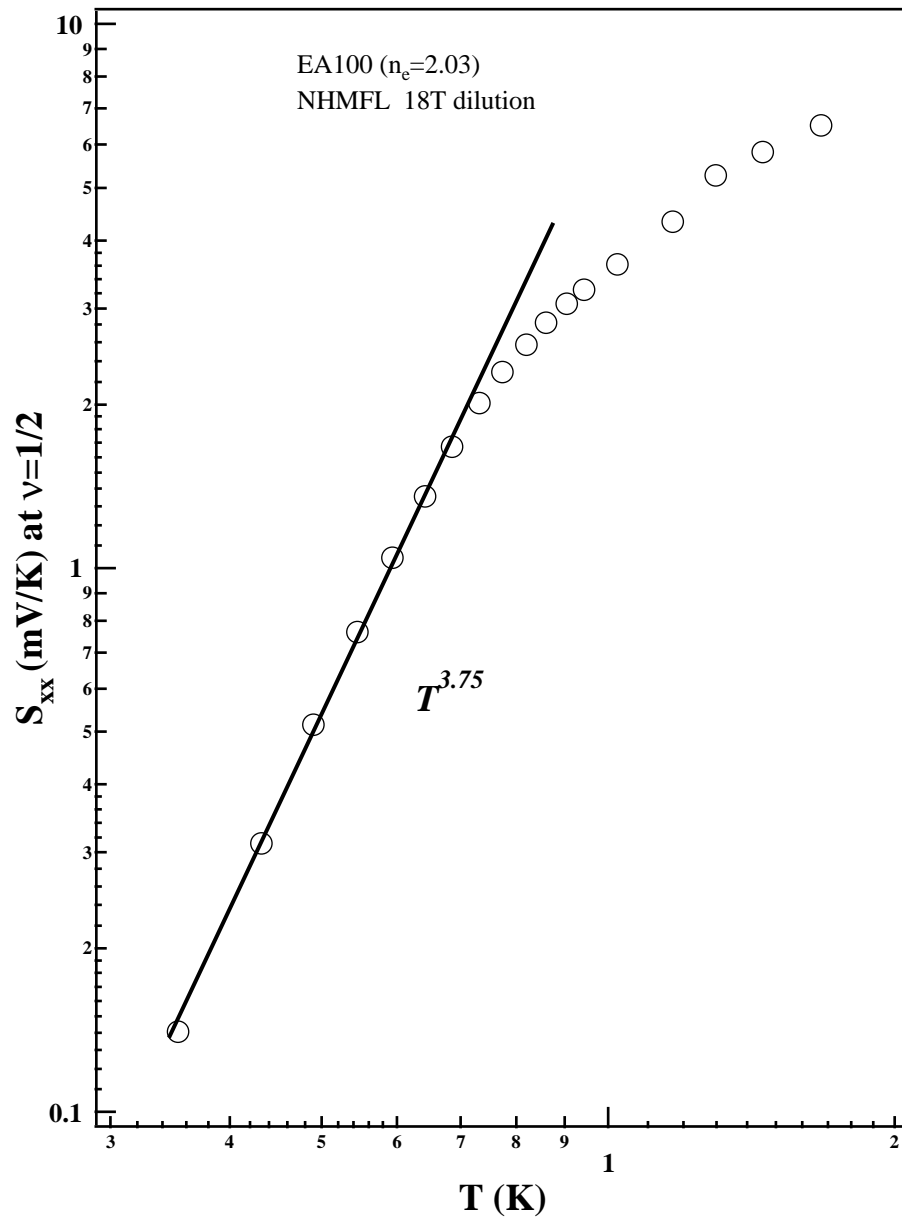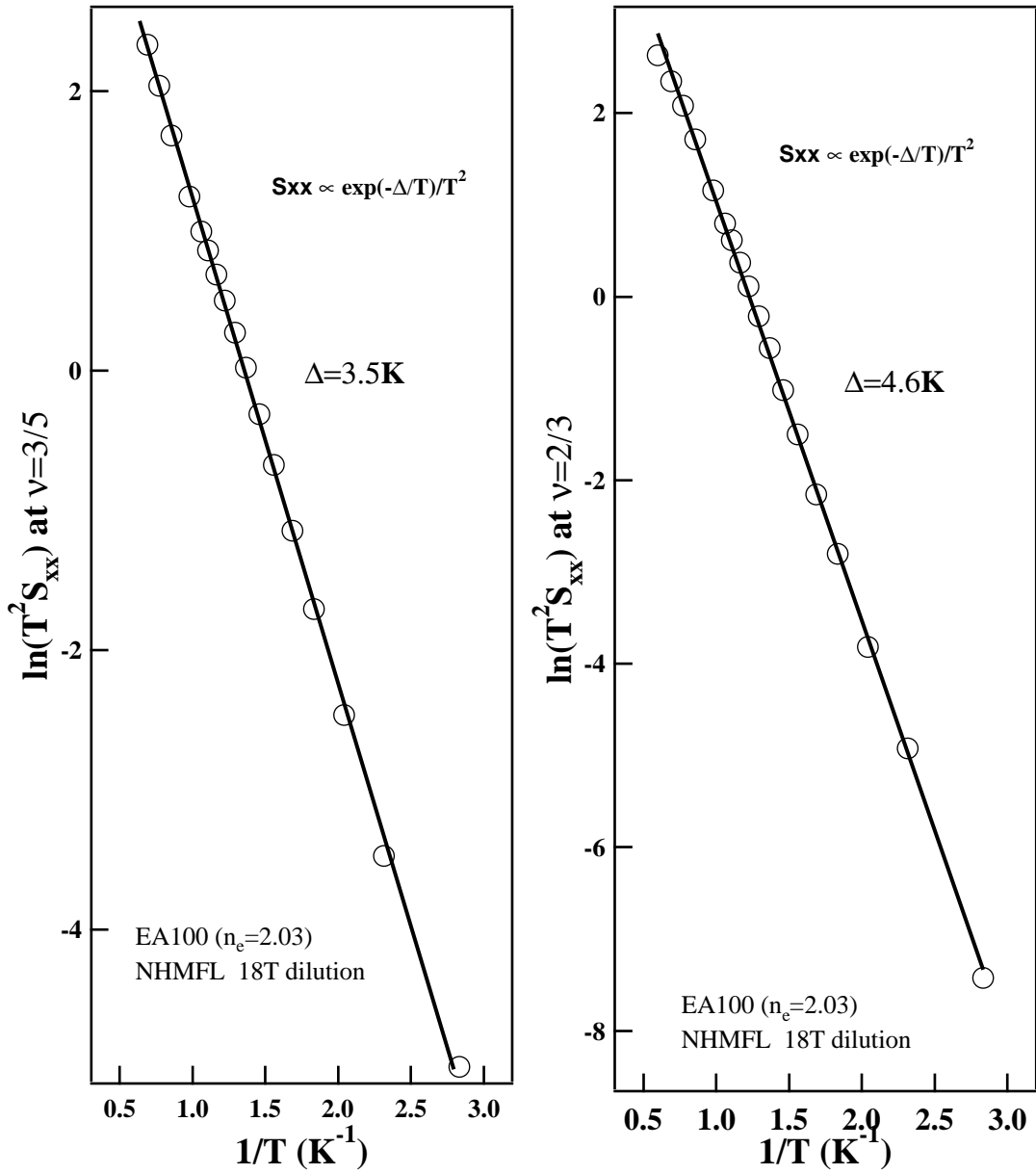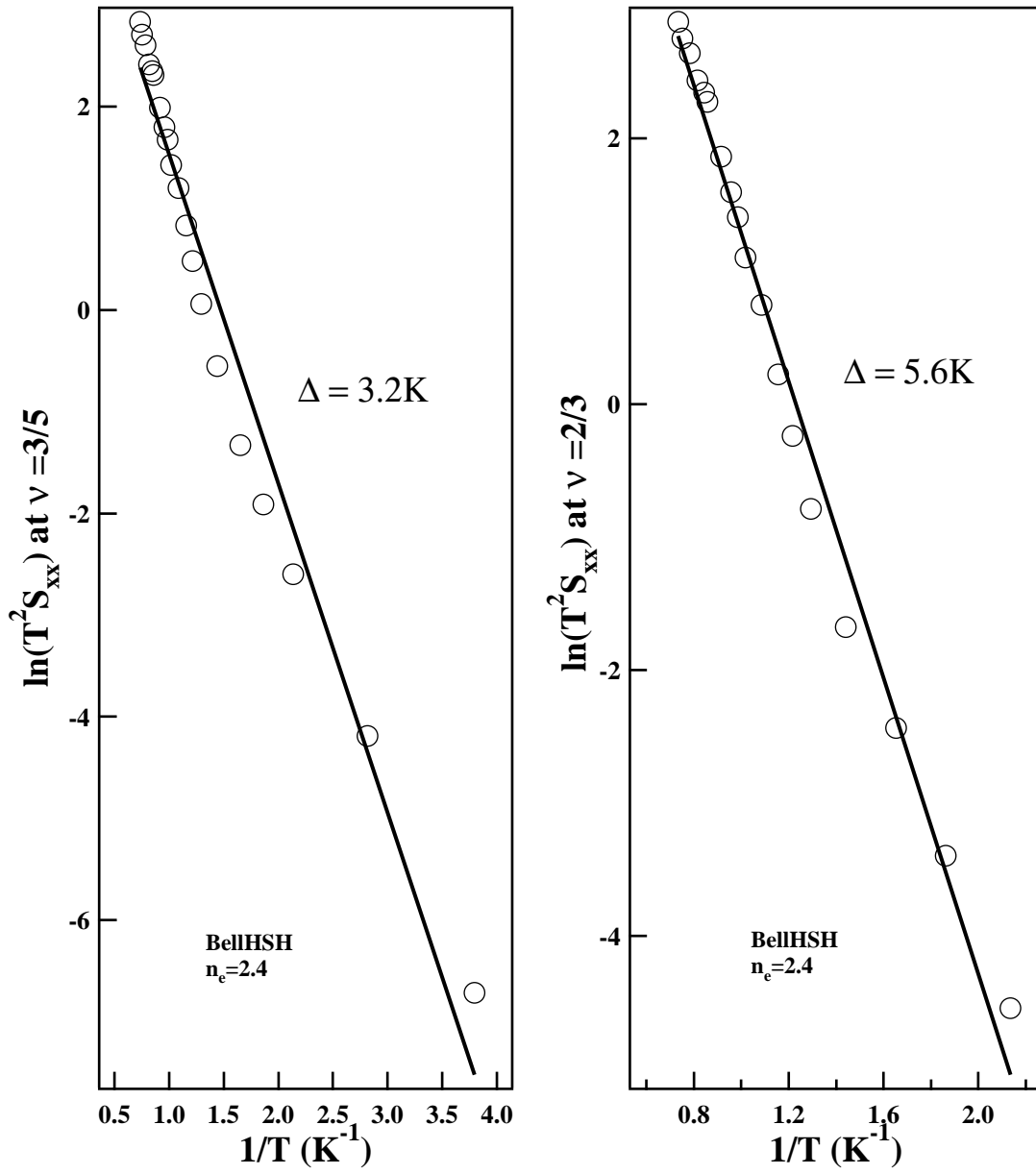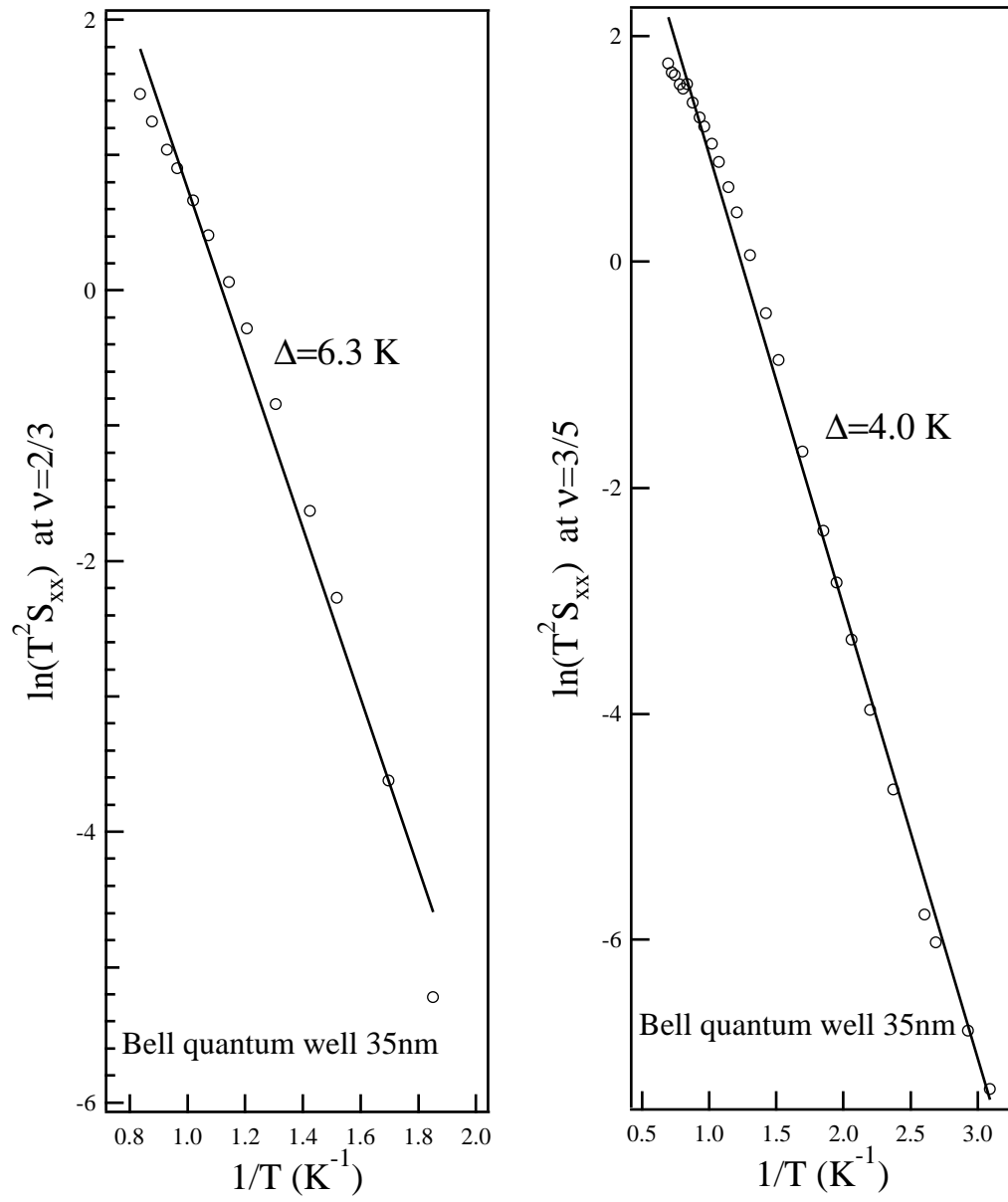
Figure 4.14. Temperature dependence of TEP at $\nu = 2/3, 3/5$ for BellHSH

Figure 4.15. Temperature dependence of TEP at $\nu = 2/3, 3/5$ for BellQW35nm
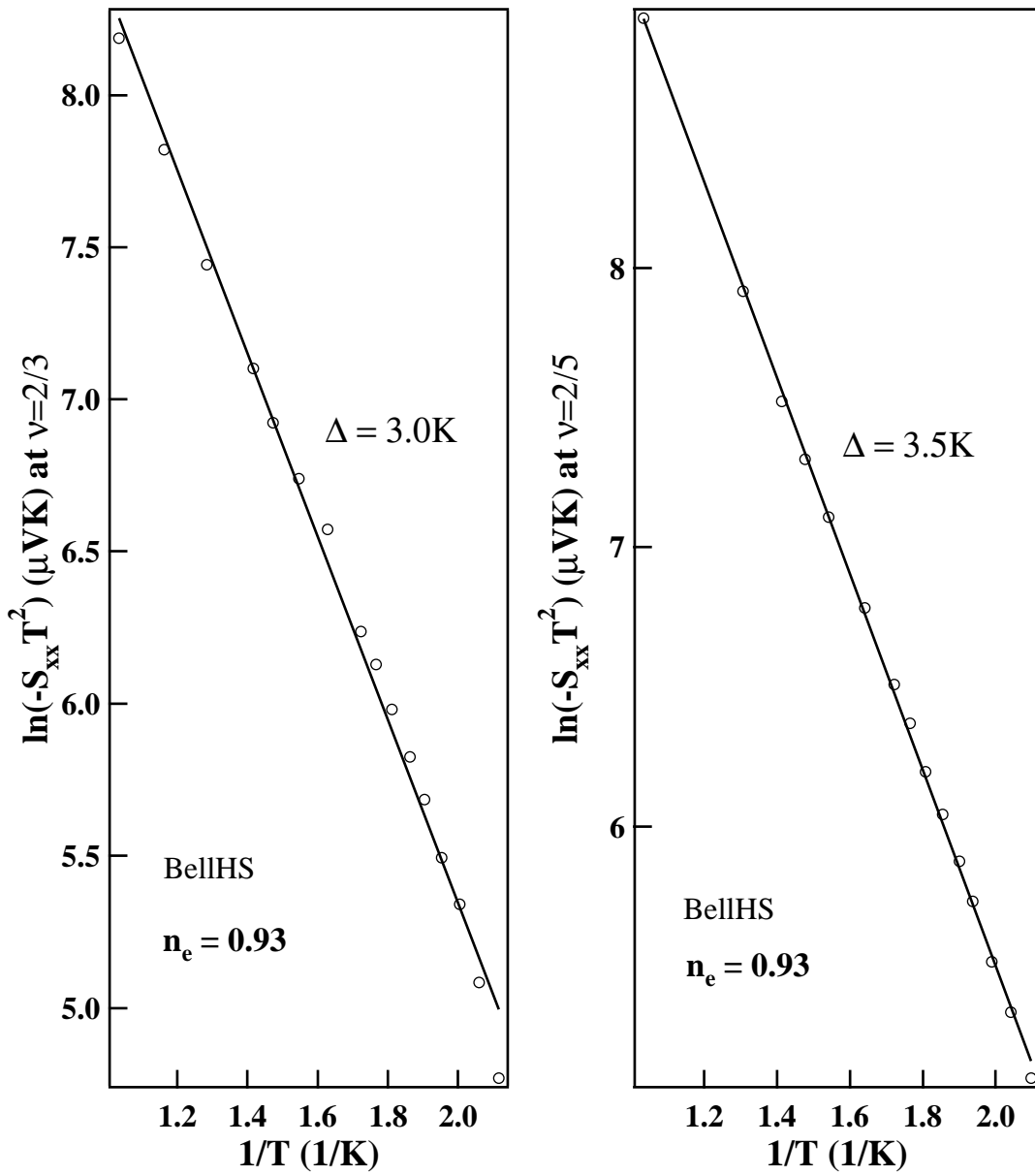
Figure 4.16. Temperature dependence of TEP at $\nu = 2/3, 3/5$ for BellHSL

are $\Delta \sim 5.6$ K at $\nu = 2/3$ and $\Delta \sim 3.2$ K at $\nu = 3/5$ for BellHSH sample. For BellQW35nm sample, $\Delta \sim 6.3$ K at $\nu = 2/3$ and $\Delta \sim 4.0$ K at $\nu = 3/5$. For BellHSL sample, $\Delta \sim 3.0$ K at $\nu = 2/3$ and $\Delta \sim 3.5$ K at $\nu = 2/5$.

Because most samples do not have regular Hall bar or van der Pauw geometry for contacts, conventional resistance measurement of the energy gap is not available. However, the energy gaps in high-mobility samples have been documented [28]. In [28] the samples with density of 1.12 and 2.3, and mobility of 12 $\times 10^6$ have parameters very close to our low and high density samples. For the low density sample of 1.12, the gap energies measured are 4.5 K at $\nu = 2/3$ and 3 K at $\nu = 2/5$, respectively. For the high density sample of 2.3, the gap energies are 6.8 K at $\nu = 2/3$ and 3 K at $\nu = 3/5$, respectively. These gap energies are deduced from the activation behavior of $\rho_{xx} \propto exp(-\Delta/2K_BT)$. The fitted activation energies from TEP, shown above, are close to those cited gap energies. It appears that a fitting formula of $S_{xx} \propto exp(-\Delta/k_BT)/T^2$ is reasonable to obtain the gap energies. This point is important because the conventional fitting formula is supposed to be $S_{xx} \propto exp(-\Delta/2k_BT)/T^2$, which means that the resulted fitting energies will be doubled and unreasonable. A theoretical understanding is certainly needed to clarify this observation.

4.4   Discussion about the anomalous peaks

Specifically, there are several possible mechanisms for the anomalous peaks: 1) The spectral DOS at $\nu = 2/3, 3/5$, and $2/5$ becomes significantly large at high temperature, comparing with the nearby filling factors; 2) Similar to the low field oscillation case, this is another manifestation of the acoustic phonon resonant scattering of CFs; 3) Quasiparticles are being excited from the incompressible ground states to the excited states by ballistic phonons.

It is difficult to imagine that the spectral DOS could be significantly large, comparing with the nearby area. Basically, due to the incompressible quantum liquid states at these fractional filling factors, the spectral DOS is almost zero at low temperature. The contribution to any transport properties comes from the

activation behavior of quasiparticles at higher temperatures. In the limit of high temperatures, there are no incompressible states, so the spectral DOS at these filling factors should be very close to their close area. No anomalous peaks should be observed.

In the CFs model, the FQH states of electron can be equivalently described by the IQH states of CFs. The filling factor (ν) of electron is equivalent to integer filling factor (p) according to the relation: $\nu = p/2p\pm1$. $\nu = 2/3, 3/5$ corresponds to $p = 2, 3$. Similar to the low field oscillation case, it is possible that the anomalous peaks are caused by the CFs resonant absorption or emission of phonons with $q = 2k_F$. However, this idea does not fit into our data, in at least the following two aspects:

a). The effective mass problem of CFs. Based on Equation 3.5, the effective mass of CFs can be derived:

$$m_{CF} = \frac{lB_l^{eff}e}{2\sqrt{4\pi n_e}} \quad , \tag{4.1}$$

where l is the order of the oscillation peaks, and B_l^{eff} is the effective magnetic field of CFs at the oscillation peak of l. There are two reasonable ways to assign l to the two anomalous peaks at $\nu = 2/3, 3/5$: $l = 1, 2$ or $l = 2, 3$. m_{CF} can be calculated in unit of electron vacuum mass (m_0). The results for the EA100 sample are shown in Table 4.1, which also includes the experimental value cited from [62, 28].

From Table 4.1, it is clear that the phonon resonance model does not result in a reasonable value of the effective mass of CFs at $\nu = 2/3, 3/5$.

Table 4.1. The effective mass of CFs

	$\nu = 2/3$	$\nu = 3/5$
$l = 1, 2$	$m_{CF} = 0.77m_0$	$m_{CF} = 1.03m_0$
$l = 2, 3$	$m_{CF} = 1.54m_0$	$m_{CF} = 1.54m_0$
[62]	$m_{CF} = 0.82m_0$	$m_{CF} = 0.82m_0$

b). Experimentally, activation energies of two anomalous peaks at $\nu = 2/3, 3/5$ are not the same, instead, the activation energies are close to the gap energies of $\nu = 2/3, 3/5$ [28], as shown in the previous section. According to the phonon resonance model: $\hbar u 2k_F = l\hbar\omega_c$, they should be the same. No matter how many LLs (l) a CF has jumped over, the absorbed phonon has the same energy. Specifically, the activation energies at different oscillation peaks (l) should be the same.

From a) and b), the anomalous peaks are unlikely caused by the CFs resonant absorption or emission of phonons with $q = 2k_F$.

One of the possible explanations can be related to ballistic phonon scattering. The activation energies can be extracted from the temperature dependence of TEP at $\nu = 2/3, 3/5$ by fitting into the special formula of $S_{xx} \propto exp(-\Delta/k_BT)/T^2$. The fitting energies are close to the corresponding gap energies, shown in Section 4.3.2. This special fitting formula can be understood by the ballistic phonon model [63]. The neutral Magneto-rotons are excited from the incompressible ground states to the gaped excited states by absorbing the ballistic phonons with the energies equal to electron gap energies at $\nu = 2/3, 3/5$. Then the magneto-rotons dissolve to electric quasi-particles, which contribute to S_{xx}, so S_{xx} is proportional to the density of the ballistic phonon ($exp(-\Delta/k_BT)$) [20, 63]. Most probably, in our practical experiments, the measured T is not the temperature of 2DEG, and is the lattice temperature. Further work is needed to find out the origin of the anomalous peaks in TEP.

CHAPTER 5

MAGNETORESISTANCE STUDY
OF ONE-HALF STATE

This chapter focuses on magnetoresistance measurement around one-half state in a high magnetic field. A FQHE state with even-denominator was first discovered at $\nu = 5/2$ [4] in 1987. Later, the FQHE state at $\nu = 1/2$ was found in a double quantum well [5] (DQW) and a wide single quantum well (WSQW) with effective double layers [6] in 1992. By introducing extra degrees of freedom (spin or layer index) to electron, those FQHE states can be explained by the two-component model theoretically [24, 8, 9]. Remarkably, Moore and Read proposed that the FQHE state at $\nu = 5/2$ could also be explained by the one-component model [14], in which CFs are polarized and have no spin degree of freedom, and the FQHE state at $\nu = 5/2$ is a ground state of p-wave paired CFs. The recent experiment [64] supported the one-component model. Furthermore, Park and Jain suggested [16] that a FQHE state at $\nu = 1/2$ may be induced by increasing the thickness of 2DEG in a WSQW sample with single-layer characteristics. Experimentally, it is interesting to study the one-half state in a wide quantum well sample with a single layer, which is different from the previous DQW or WSQW double-layer systems.

The detailed features of the EA467 and EA466 samples will be given first; then their ρ_{xx} over the magnetic field are presented. The temperature dependence and the density dependence of ρ_{xx} around the one-half state are shown. In the end, the differential of ρ_{xy} against the magnetic field gives a very interesting result.

5.1   Sample characterization

EA467 and 466 are made from the modulation-doped GaAs-$Al_{0.3}Ga_{0.7}$ quantum well grown by molecular beam epitaxy on the (001) GaAs substrate in Sandia

National Labs. Both the top and bottom spacers are 70 nm wide. In dark, $n_e = 3.4$ and $\mu = 3 \times 10^6$. In Figure 5.1, numerical calculation shows the electron distribution profile along the z direction. The electron profiles show the single layer feature. λ characterizes the thickness of 2DEG. EA467 has a well width of 35 nm and λ of 29.5 nm. $\nu = 1/2$ is at $B = 28$ T, at which the magnetic length $l_B = 4.85$ nm. Dimensionless thickness α is defined as λ/l_B, which has a value of ~ 6 for EA467 at $\nu = 1/2$. According to Park *et al.* [16], if $\alpha \geq 5$, the one-half state may become a FQHE state by forming p-wave pairs of CFs. The energy difference between the first subband (E_1) and the second subband (E_2) is 82.5 k for EA467, so there are some electrons occupying the second subband for the high density of 3.4. The low-field Shubnikov-de Hass oscillation data are shown in Figure 5.2. The beats are clearly shown in the whole range of SdH oscillations. The beats are always observed if electrons occupy two subbands. Roughly, it can be estimated that 15% electrons occupy the second subband. For the EA466 sample with well width of 30 nm, $\lambda = 24$ nm and $\alpha = 5$ at $\nu = 1/2$. The energy difference between E_1 and E_2 is 125.5 k for EA466, so there are only few electrons occupying the second subband.

The extension of electrons along the z direction reduces the short range part of the repulsive Coulomb interaction between electrons, a situation that favors electrons forming pairs at half filling factors. One example is that electrons get paired and form an FQHE state at $\nu = 5/2$, although reducing the repulsive Coulomb interaction comes from screening by the lowest Landau level, rather than from extension along the z direction. The repulsive Coulomb interaction could be characterized by the Haldane pseudo-potential (V_m) [65, 66, 67]. For small number of m, V_m describes the short-range part of Coulomb interaction, whereas for a large number of m, V_m describes the long-range part. Specially, V_1/V_3 tells us the the relative strength of the repulsive interaction to the electron correlation. If the value of V_1/V_3 is lower than that of the ideal Coulomb interaction, the repulsive interaction is reduced and the pairing mechanism is favorable. V_1/V_3 is calculated at $\nu = 1/2$ for EA467. Comparing with the ideal Coulomb interaction, V_1/V_3 is about 10% smaller for EA467, whereas V_1/V_3 is about 17% smaller at the FQHE
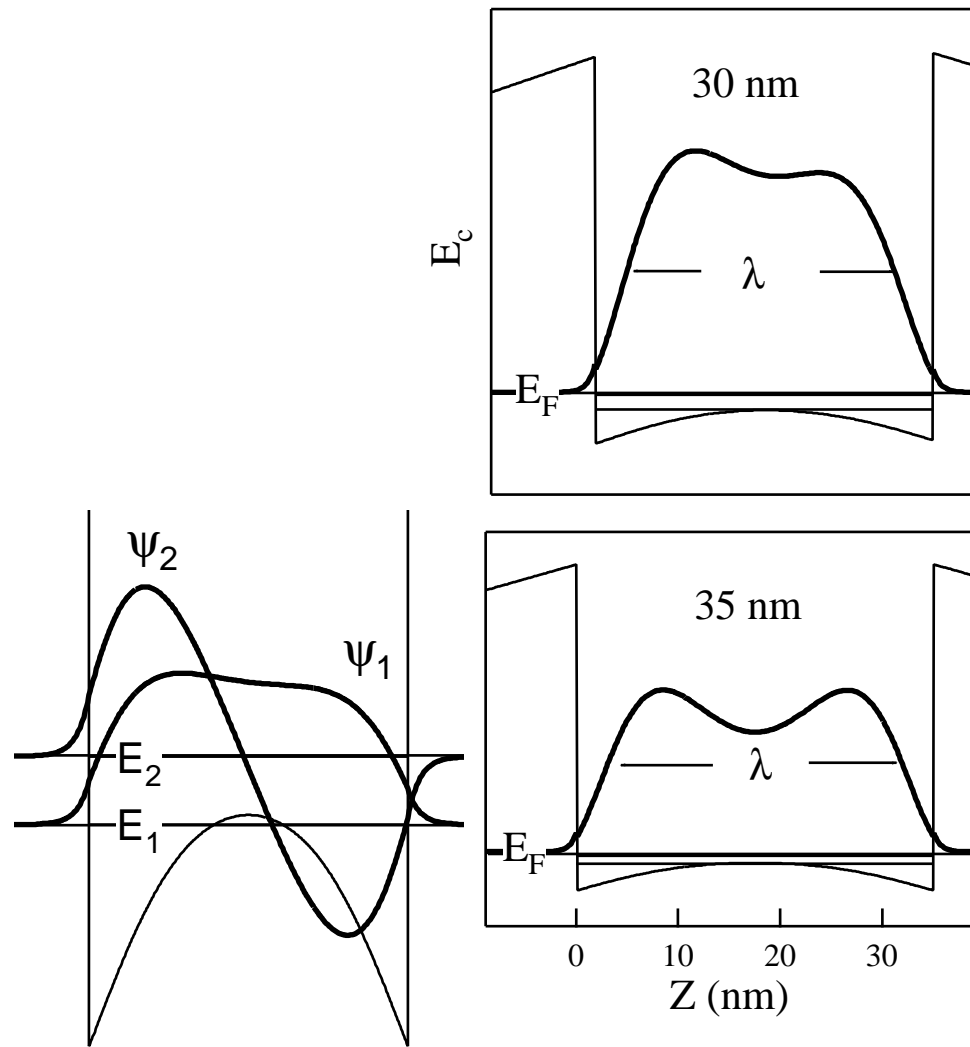
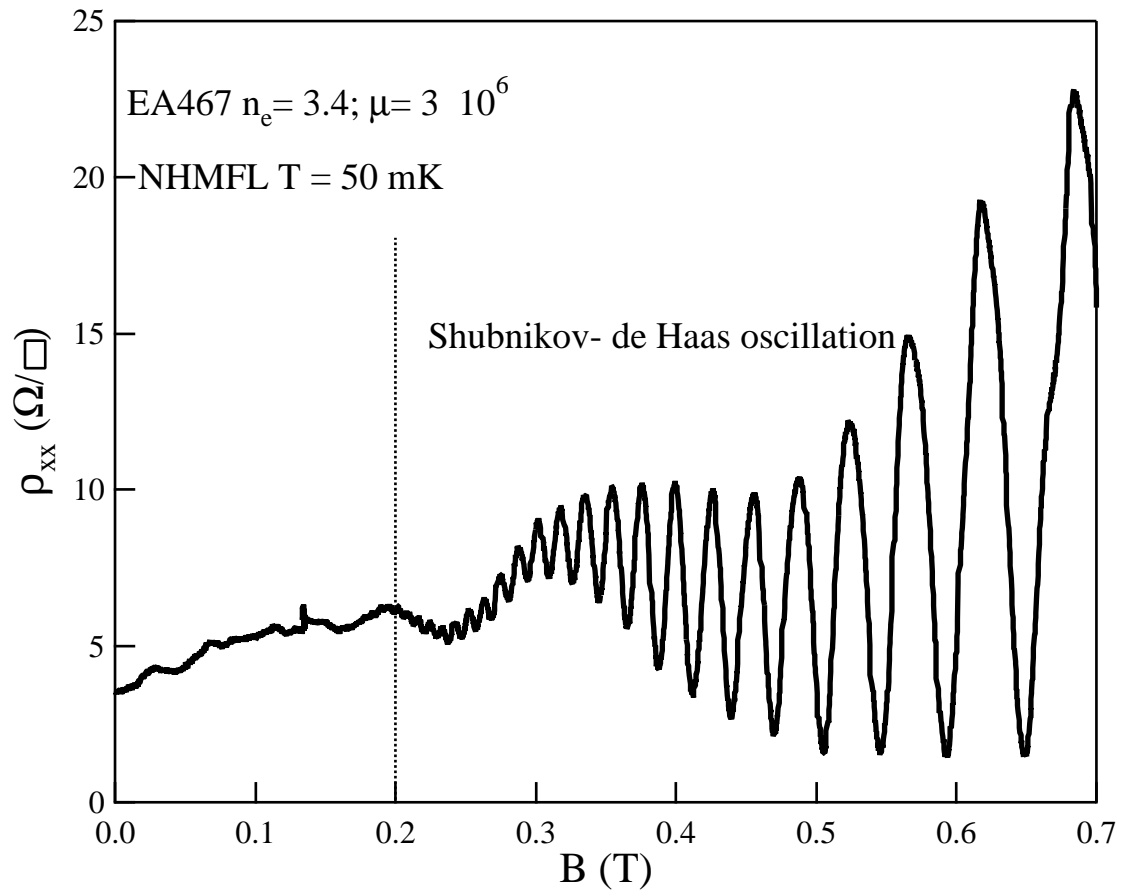**Figure 5.1**. Electron distribution profile along z direction

Figure 5.2. SdH of EA467

state of $\nu = 5/2$. The repulsive part of the Coulomb interaction is reduced for EA467. Ten percent change of V_1/V_3 in EA467 is comparable with 17 % change of V_1/V_3 at the FQHE state of $\nu = 5/2$, so perhaps some new features of one-half state could be observed.

Our samples are patterned in either standard van der Pauw geometry or Hall bar geometry. Hall bar width of 0.2mm is lithographically defined. Experiments are performed in two top-loaded ^{3}He-^{4}He dilution refrigerators, and in a 33T resistive magnet or a 45T hybrid magnet in the National High Magnetic Field Lab (NHMFL). Base temperature can go as low as 50 mk, and the magnetic field can be as high as 45 T. Small electric current of 20 or 50 nA is used to avoid heating. The electron density can be adjusted by the front and back gate voltages.

5.2   Magnetoresistance measurement around one-half state

Figure 5.3 shows an overview of ρ_{xx} at $T = 50$ mK for EA467 and EA466. The series of minima shows IQHE and FQHE. Both samples display FQHE states at filling factors as high as $6/11$, which indicates the high quality of samples. The new feature is that a deep and narrow minimum has developed at $\nu = 1/2$ for the 35 nm sample. The 30 nm sample also shows the deep minimum at $\nu = 1/2$, which is not as sharp as the 35 nm one. Their concomitant Hall resistances do not develop into a quantized plateau around $\nu = 1/2$. There are small dips at $\nu = 3/2$ for the 35 nm sample and at $\nu = 5/2$ for the 30 nm sample. All data shown after are from the 35 nm sample because of its sharper minimum at $\nu = 1/2$.

Figure 5.4 shows the temperature dependence of ρ_{xx} around $\nu = 1/2$ for EA467 with a van der Pauw geometry. The ρ_{xx} around $\nu = 1/2$ exists a deep minimum, which is strongly temperature dependent. As T goes up, the ρ_{xx} at $\nu = 1/2$ moves down at first, then it goes up above 500 mK. The ρ_{xx} behavior is completely different from the observation of Jiang *et al.* on one-half minimum in a heterojunction [68], in which ρ_{xx} at $\nu = 1/2$ shows no discernible T dependence at low temperatures. In the right upper figure, ρ_{xx} at $\nu = 1/2$ shows roughly logarithmic temperature
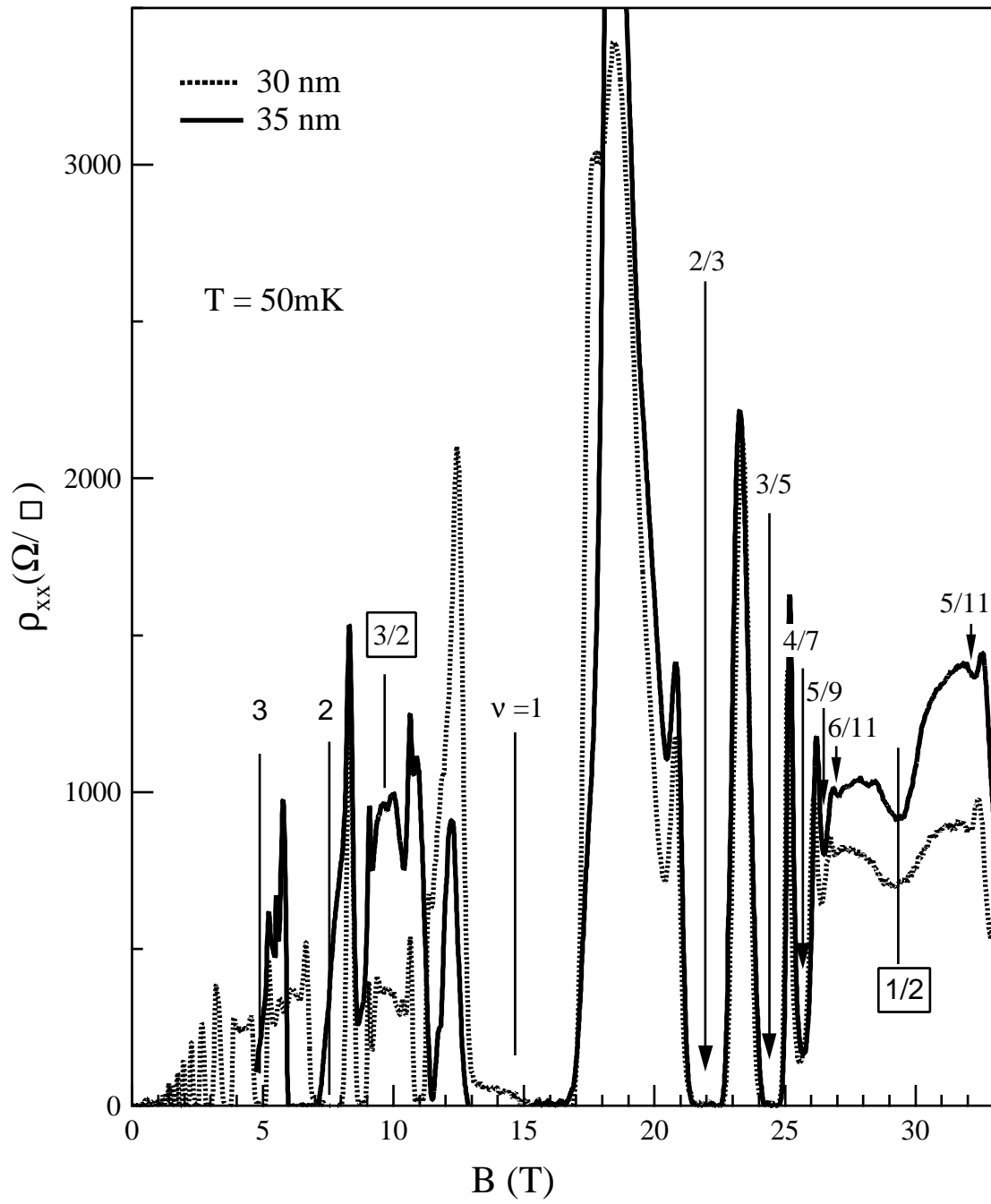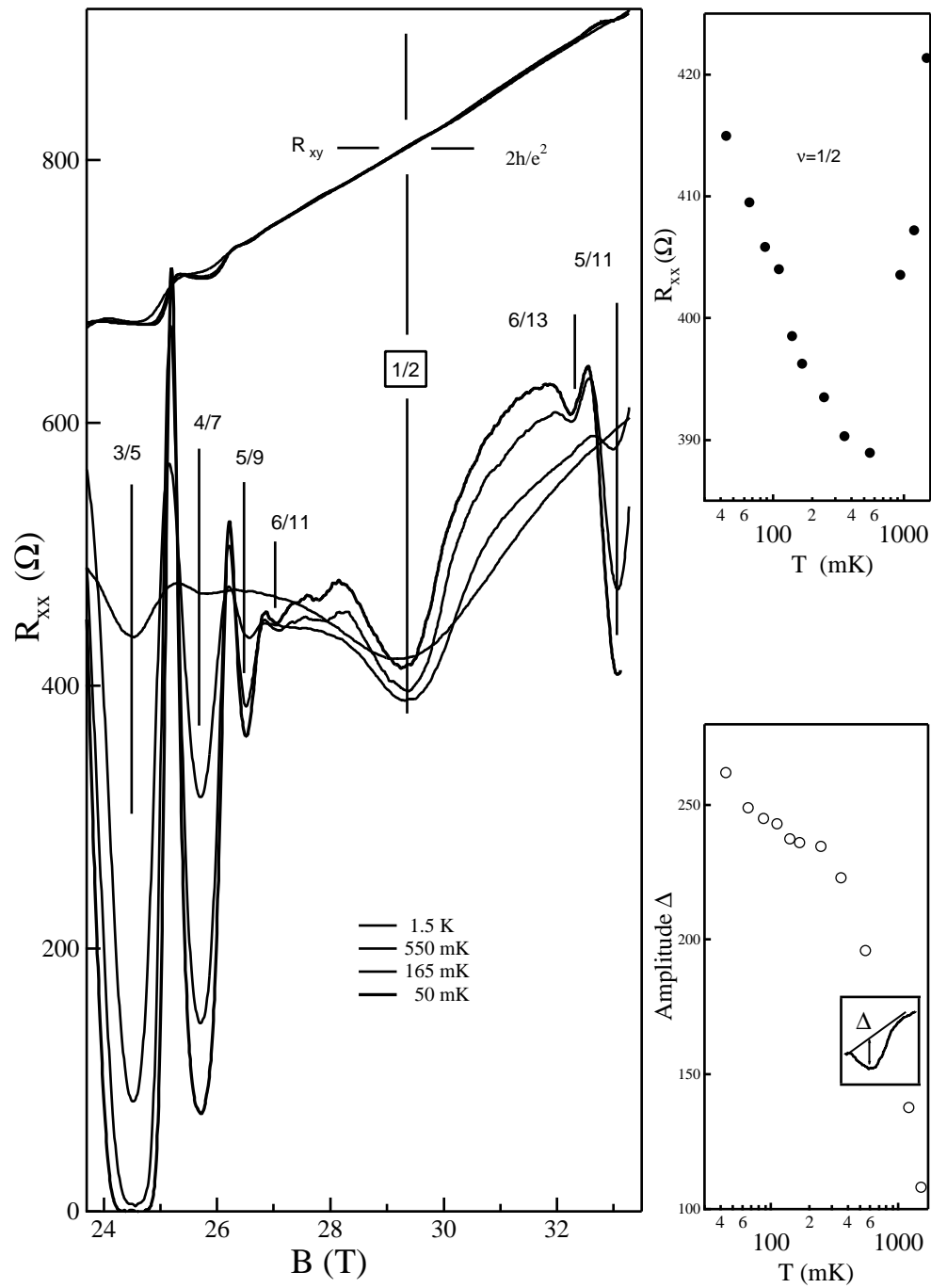
Figure 5.3. Magneto-resistivity overview of 30nm and 35nm QWs

Figure 5.4. Temperature dependence of R_{xx} around $\nu = 1/2$ for EA467. Figures on the right show how R_{xx} and amplitude of the minimum change with temperature.

dependence at $T < 500$ mK. This feature is similar to the result of Rokinson *et al.* [69]. This feature can be explained by the interaction between CFs in the presence of disorder at low temperature [69, 70, 71], which leads to the logarithmic temperature dependence of Altshuler-Aronov type. Generally, the weak localization also gives rise to the logarithmic correction to the conductivity at $B = 0$. However, the weak localization at $\nu = 1/2$ should be suppressed, because the gauge field fluctuations break up the time-reversal symmetry. The electron resistivity can be converted to the CF's conductivity (σ_{xx}^{CF}) by the formula of $\sigma_{xx}^{CF} = 1/\rho_{xx}^{CF} = 1/\rho_{xx}$, according to Equations 2.33 and 2.9. The temperature dependence of σ_{xx}^{CF} can be fitted by the following equation [69]:

$$\sigma_{xx}^{CF} = \sigma_0^{CF} + \lambda \frac{e^2}{h} ln \frac{T}{T_0} \qquad \lambda = 1.06 \quad . \tag{5.1}$$

The fitting value of λ is 1.06. The fitting λ is 1.6 in [69]. These two numbers are reasonably close. Both of them are much larger than the zero-field λ values (0.09 and 0.17 [72, 73]), which indicates that CFs experience significant large-angle scattering due to gauge-field fluctuation, in contrast with electrons at zero magnetic field, which are controlled by small-angle scattering. The short-range interaction between CFs via gauge-field fluctuations may give rise to a large contribution to λ.

In the right lower figure, the amplitude of the one-half minimum keeps going down as T goes up. The dramatic change of the amplitude begins at 500 mK, which is the same temperature that ρ_{xx} at $\nu = 1/2$ turns around. At the higher temperature, the interaction between CFs does not introduce any correction to ρ_{xx} at $\nu = 1/2$ and a normal metal behaviour appears.

The density dependence of ρ_{xx} around $\nu = 1/2$ is shown in Figure 5.5. All traces of different densities are normalized to the trace of density of 3.36 (no gate voltages), and each trace is scaled by its own ρ_{xx} at $\nu = 1/2$. When n_e is increased by the balanced front gate and back gate voltages, ρ_{xx} at $\nu = 1/2$ is lowered down, and the amplitude of one-half minimum is raised up. When $n_e > 4.64$, ρ_{xx} at $\nu = 1/2$ goes up, and the amplitude of one-half minimum is lowered down. This
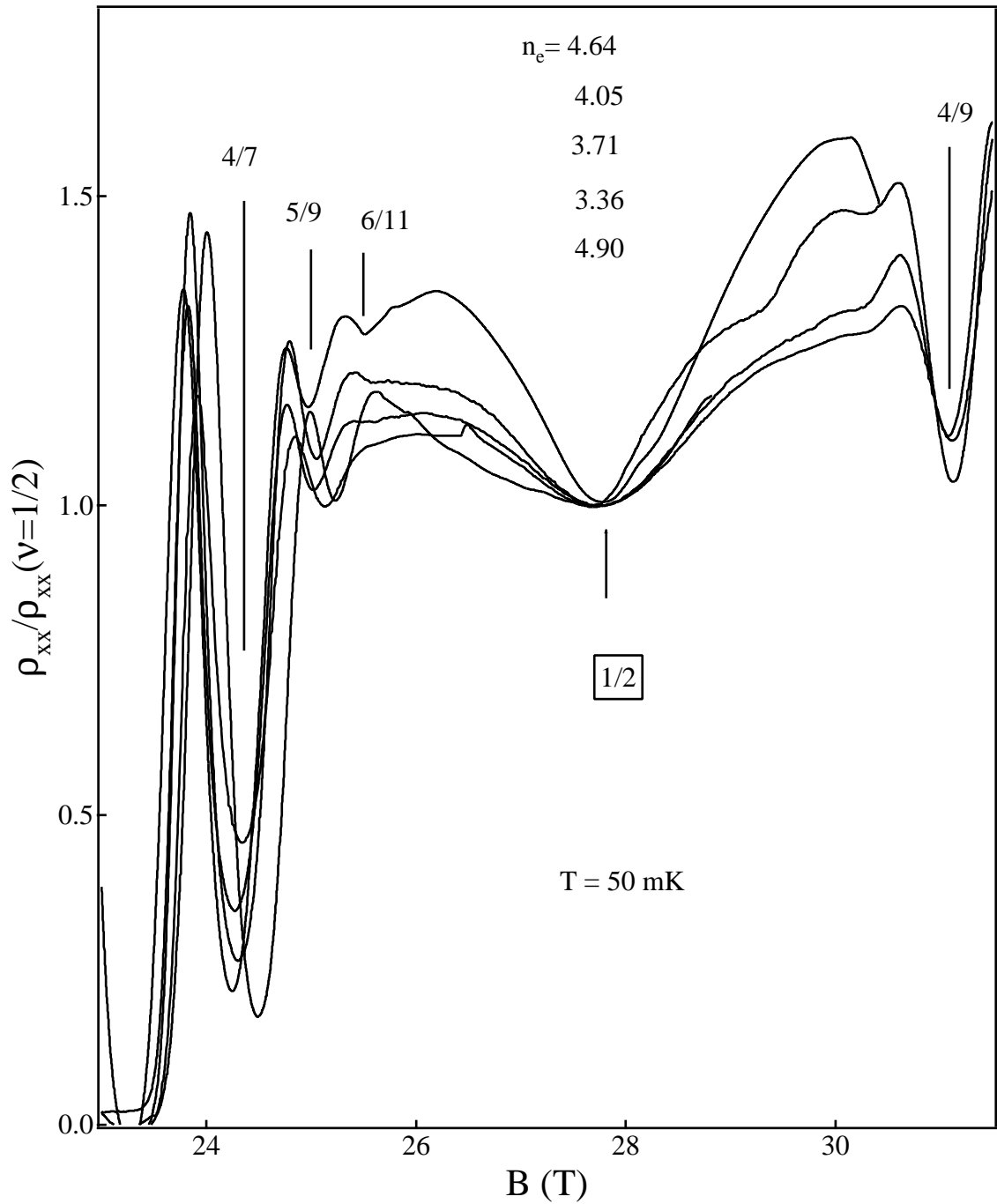
Figure 5.5. Density dependence of ρ_{xx} around $\nu = 1/2$ for EA467. All traces are scaled with the trace having density of 3.36. Each trace is scaled with its own ρ_{xx} at $\nu = 1/2$.

phenomenon is observed in all sets of data and in different runs. As shown in the figure, there are no obvious changes for the FQHE states (2/3,3/5,4/7,5/9). The amplitude of the deepest one-half minimum is increased by two times. However, no indication is shown that Hall resistance begins to be quantized at $\nu = 1/2$.

Increasing the density pushes one-half state up to the higher magnetic field, therefore decreases the l_B. In this way, α can be adjusted to greater than 5, which favors the FQHE state at $\nu = 1/2$ in [16]. Experimentally, there is no indication of the FQHE state at $\nu = 1/2$, although the deep minimum of ρ_{xx} is always observed at $\nu = 1/2$.

There is an alternative way to discuss the experimental data. In CF's language, the one-half minimum of electrons can be interpreted as the positive magnetoresistance (PMR) of CFs. As one-half state is pushed up to the higher magnetic field, PMR of CFs becomes stronger. Khveshchenko explained PMR of CFs as the result of logarithmic correction to Hall conductivity, due to the interference of disorder and interaction effect [74]. After matrix inversion from conductivity to resistivity, he obtained the PMR formula of CF's at $B_{eff} < 1$ T, in which the quadratic B_{eff} dependence is shown:

$$
\begin{aligned}
\Delta\rho_{xx}^{CF}(B_{eff}) &\equiv \rho_{xx}^{CF}(B_{eff}, T) - \rho_{xx}^{CF}(0, T) \\
&\propto -ln(k_F l)[\rho_{xx}^{CF}(0, T)]^2 (\mu^{CF})^2 ln\frac{T}{T_0}(B_{eff})^2 \\
&\propto \frac{1}{n_e^2}(B_{eff})^2 \quad .
\end{aligned}
\tag{5.2}
$$

According to the formula above, the shape of PMR should be the same around $\nu = 1/2$ as the density goes up, because B_{eff} scales with n_e. However, the shape of PMR is observed to become steeper as the density goes up. So the experimental data are not consistent with this model. Rokhinson and Goldman compared this model with their experimental data [75] and found that this model was correct qualitatively, but quantitatively incorrect. They made a different conclusion from ours, which indicates the special features of the samples studied here.

Mirlin *et al.* had another possible explanation for PMR of CF's, based on classical "Memory Effect" due to existence of the random magnetic field [76]. In this model, the governing parameter is α, defined as d/R_0, d is the correlation length (equal to the spacer width in 2DED) and R_0 is the Larmor radius in the field B_0, which characterizes the strength of the random magnetic field in CF's picture. $B_0 = (\hbar/e)(\alpha/d)\sqrt{4\pi n_e}$. Under the conditions of $\alpha << 1$ and $B_{eff} << B_0$, his theory predicted the quadratic B_{eff} dependence for PMR of CF's, expressed as $(B_{eff}/B_0)^2$. Fitting the PMR data of CFs into this model, $B_0 \sim 2.5$ T, which leads to $\alpha \sim 1$. It violates the assumption of $\alpha << 1$. At $\alpha \sim 1$, no analytic formula was available. Between 0.2 and 0.35 of α, his numerical simulation showed PMR of CFs but the shape was too shallow if comparing with our data. This model also predicted a critical effective magnetic field B_{eff}^c (equal to $B_0\alpha^{-1/3}$). Beyond the critical field, ρ_{xx} would dramatically drop down, due to a classical localization caused by the adiabacity of the cyclotron motion in a large B_{eff}. In our data, B_{eff}^c is around 2 T, but the theoretical value of B_{eff}^c is around 0.8 T. So there are some discrepancies between this theory and our data.

Increasing the density possibly decreases the disorder and increases the mobility [77, 78], which may influence the MR behaviour around one-half state. This effect may account for the density dependence of ρ_{xx} at $\nu = 1/2$.

Figure 5.6 shows how the ρ_{xx} changes in tilting the magnetic field. No change is observed up to 36° of the tilted angle, as expected for single layer QW sample.

In conclusion, for QWs having well width of 35nm at low temperature (< 200 mK), ρ_{xx} exhibits a sharp, strongly temperature-dependent minimum centered at $\nu = 1/2$, while concomitant ρ_{xy} does not develop into quantized plateau. As the density increases, the minimum at $\nu = 1/2$ first becomes sharper, and then turns flatter. No current specific theory can adequately explain the experimental data.
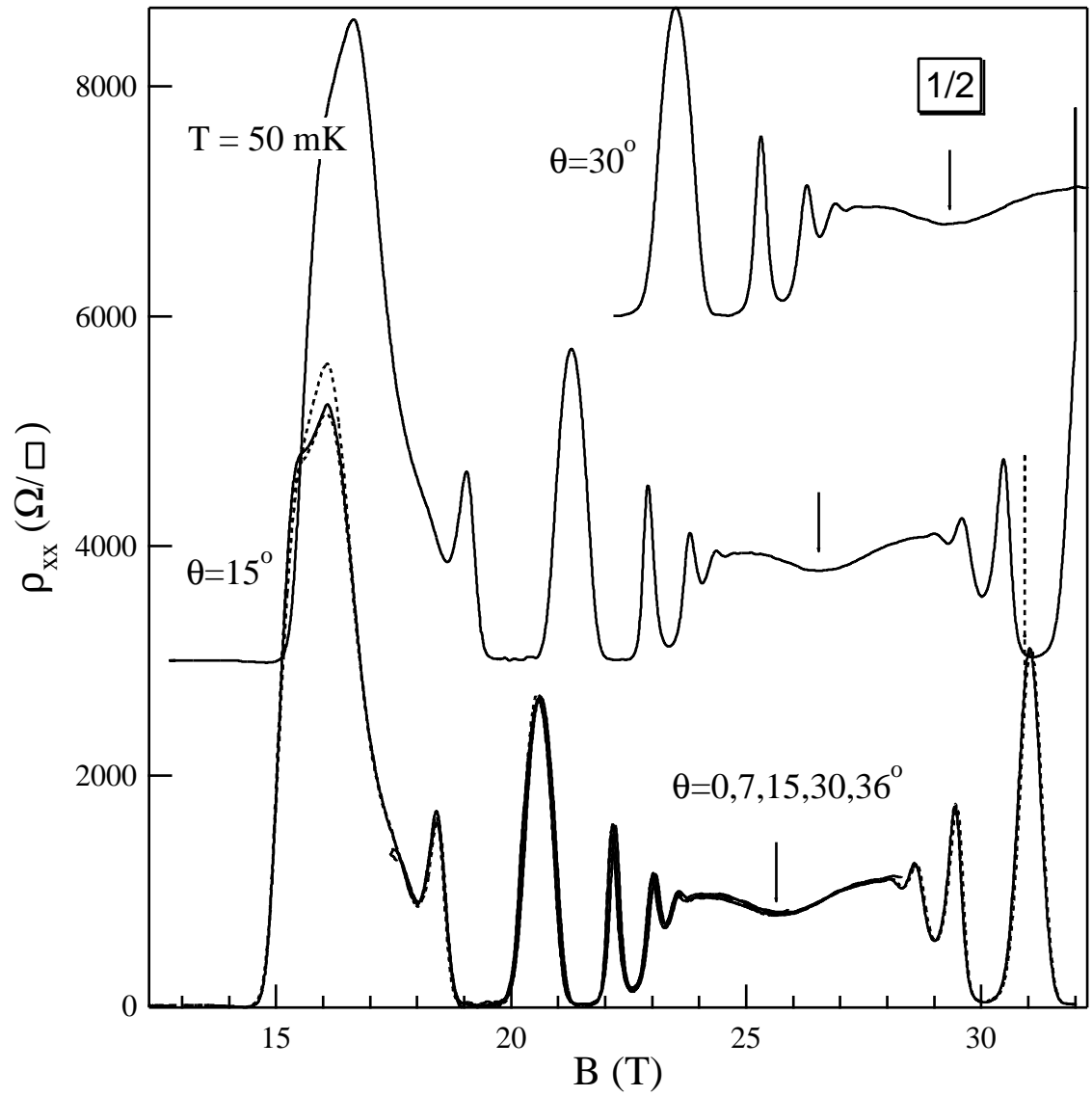
Figure 5.6. Tilted magnetic field effect. The upper two traces are shifted by 3000 and 6000 ohm

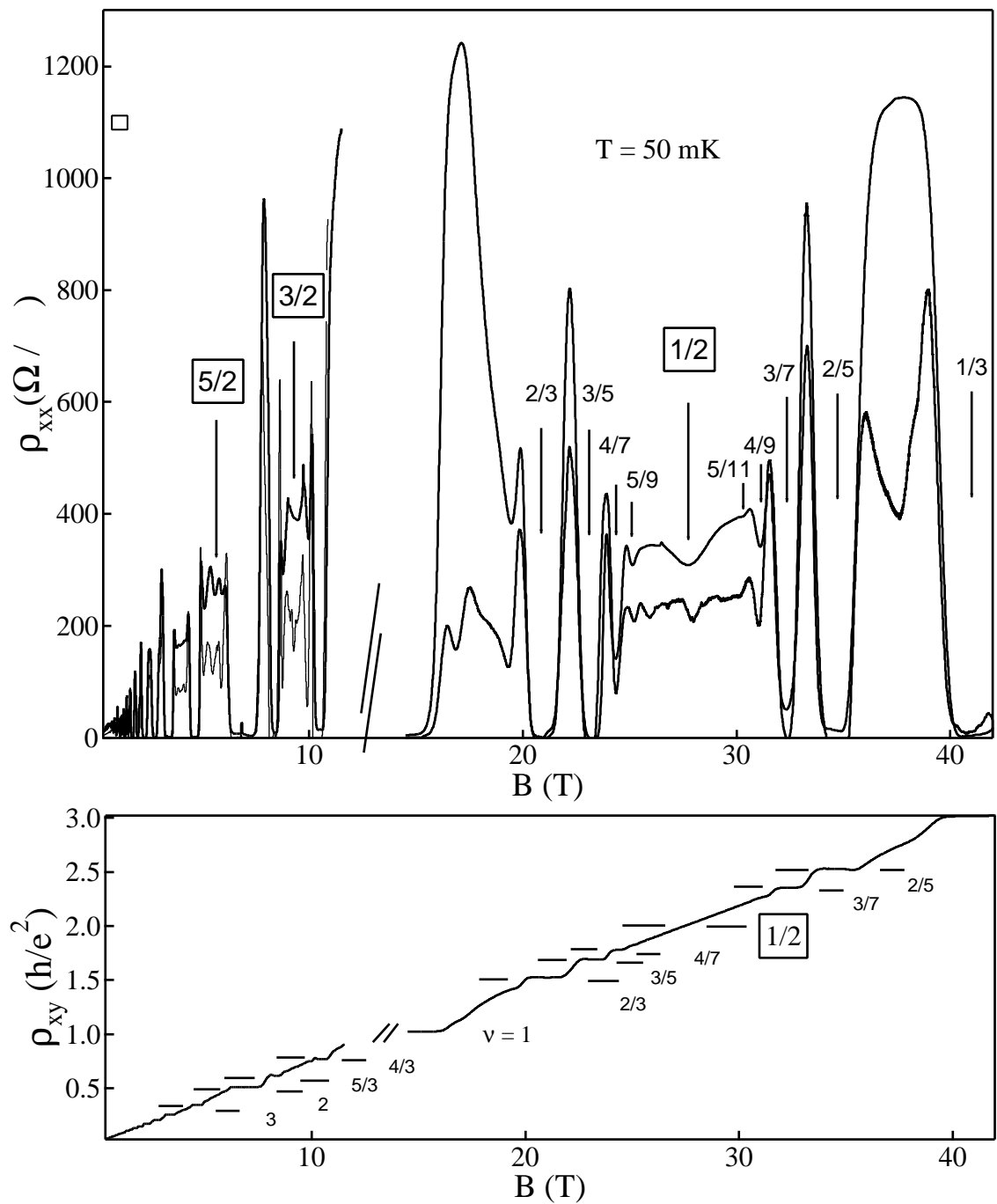## 5.3 The first derivative of Hall resistance around one-half filling factor

Almost 20 years ago, Chang and Tsui observed a striking similarity between ρ_{xx} and the first derivative of ρ_{xy} [79]. Later, Stormer reported the same phenomenon in very high mobility samples [80]. First derivative of ρ_{xy} with respect to the magnetic field faithfully reflects many detailed features of ρ_{xy} related to IQHE and FQHE, and a simple relation can be found:

$$B\frac{d\rho_{xy}}{dB} = \alpha\rho_{xx} \quad .$$

(5.3)

Following the procedure, we have studied the $d\rho_{xy}/dB$ in the 35 nm QW near 1/2 up to 45 T.

Figure 5.7 shows the overview of the resistivity at $T = 50$ mK for 35 nm quantum well sample with Hall bar geometry in the 45 T hybrid magnet. The magnetic field is swept first from 0 to 11.5T by running the outsert superconductor magnet, then from 11.5 T to 42 T by running insert resistive magnet. The data are absent between 11.5 T and 14 T as shown in the figure. In the upper figure, the top trace is ρ_{xx}, and the resistivity of the higher field part is multiplied by 0.5 to show the features of the lower field part. The bottom trace is the first derivative of ρ_{xy} with respect to the magnetic field, multiplied by the magnetic field $(Bd\rho_{xy}/dB)$, then scaled for clarity. In the lower figure, ρ_{xy} is shown. Both ρ_{xx} and ρ_{xy} show the same features as in Figure 5.3.

The first derivative of ρ_{xy} with respect to the magnetic field is done numerically by Igor Pro 3.15 software, then multiplied by the magnetic field. The striking similarity between ρ_{xx} and $Bd\rho_{xy}/dB$ is shown in the upper figure of Figure 5.7. Not only the IQH states and the principle FQHE states are reproduced, but the 5/2, 8/5,7/5, and 6/11 states are also shown clearly in the derivative trace. This phenomenological relationship between ρ_{xx} and ρ_{xy} requires fundamental theoretical explanation.

Figure 5.7. Resistivity overview of EA467. In the upper figure, the lower trace is the first derivative of Hall resistivity with respect to B, then multiplied by B.

The more striking features in our data are the sharp minima at $\nu = 1/2$ and $\nu = 3/2$, shown in the derivative trace (the bottom trace in upper figure) of Figure 5.7. Sajoto *et al.* noticed these two minima in the first derivative traces before [81]. But the minimum at $\nu = 1/2$ in our data is narrower and sharper than these earlier data. Up to now, there is no indication of the FQHE state at $\nu = 1/2$ and $\nu = 3/2$ in a single-layer 2DEG. Even at $\nu = 1/2$ and $\nu = 3/2$, the similarity between ρ_{xx} and $Bd\rho_{xy}/dB$ still exists.

Looking carefully at our data, the minimum at $\nu = 1/2$ in the derivative trace is narrower and sharper than the minimum in ρ_{xx} trace. According to the CF model, ρ_{xy} should be a straight line without slope change; and $Bd\rho_{xy}/dB$ should then be a straight slope around $\nu = 1/2$. However, a sharp minimum of $Bd\rho_{xy}/dB$ at $\nu = 1/2$ is observed. This observation is presently not understood.

The first derivative of ρ_{xy} with respect to the magnetic field and ρ_{xy} are presented in Figure 5.8 for EA467 with a van der Pauw geometry. This is the third sample from the same wafer as the previous two samples. The data in the positive and negative magnetic field are shown while the contacts configuration is not changed. In the lower figure, ρ_{xy} displays the quantized plateau, indicating normal IQHE and FQHE. The inset shows the temperature dependence of the derivative minimum at $\nu = 1/2$.

Comparing the first derivative traces in Figure 5.8 with those in Figure 5.7, they are similar. In the right trace, the sharp minimum at $\nu = 1/2$ is shown. Furthermore, the derivative minimum disappears when temperature is above 200 mK as shown in the inset. Sajoto *et al.* [81] reported a similar temperature dependence, but the temperature was higher when the minimum began to disappear.

Is there any possibility that the derivative minimum comes from the mixture of ρ_{xy} and ρ_{xx}? When the magnetic field is reversed, ρ_{xy} becomes negative while ρ_{xx} is still positive. If any mixture exists, the dip will become a maximum. However, a dip is still shown in left trace in the upper figure. It is clear that the derivative minimum at $\nu = 1/2$ does not come from the mixture of ρ_{xy} and ρ_{xx}, and indicates some subtle physics underlying the one-half state in a thick QW.
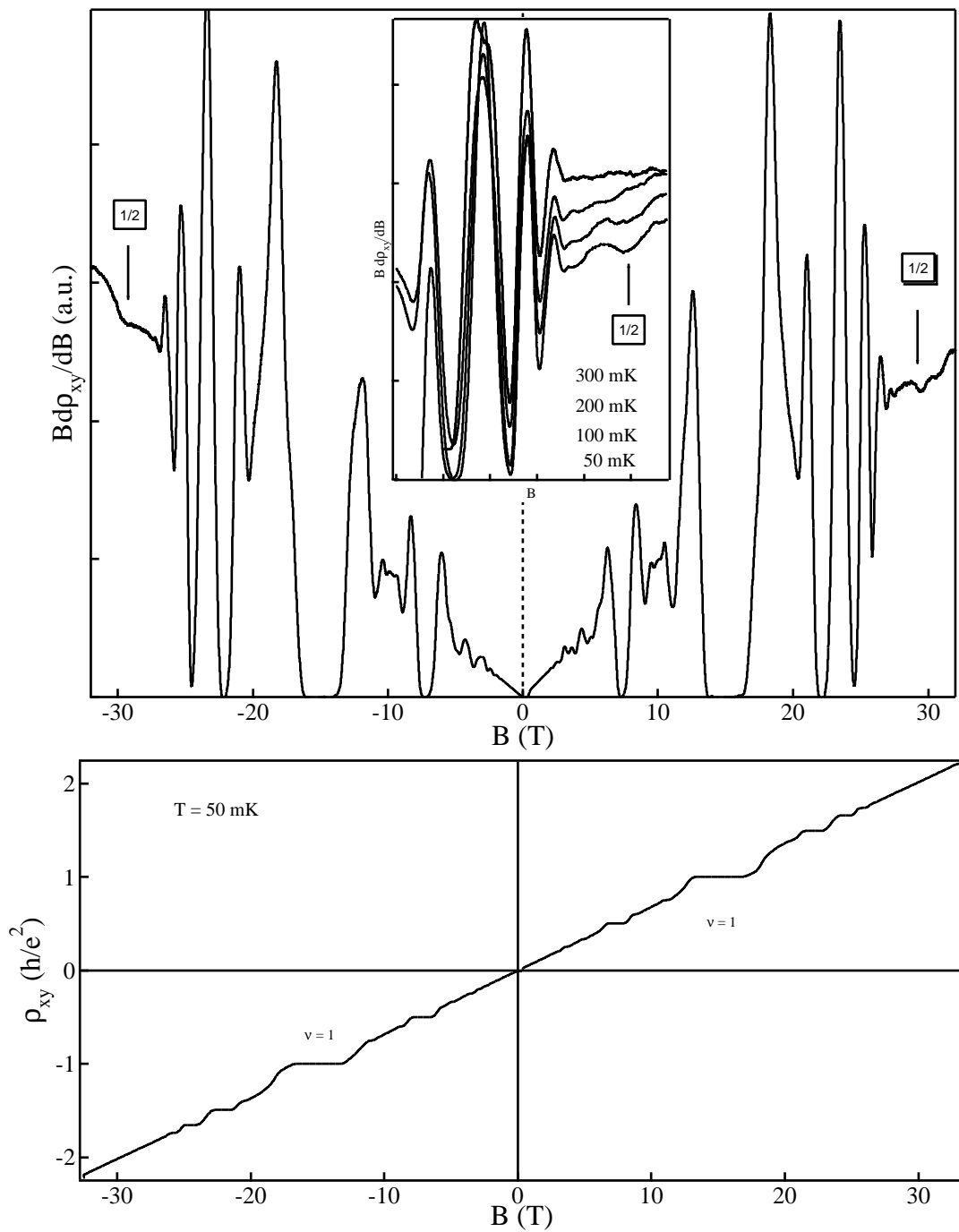
Figure 5.8. The first derivative of ρ_{xy} with respect to $+B$ and $-B$. Temperature dependence is shown in the inset.

These features are observed in all other EA467 samples measured. Concerning with resistivity rules, Simon and Halperin proposed a scenario [82]: R_{xx} is only weakly dependent on ρ_{xx} and is approximately proportional to the magnitude of fluctuations of ρ_{xy}, due to density fluctuations at not very low temperature. If the fluctuations exist on several length scales, this leads to the similarity between R_{xx} and BdR_{xy}/dB.

Experimentally, this resistivity rule appears to be not strictly held in the 1/2 of QW samples: above 200 mK, there is no minimum around $\nu = 1/2$ in the derivative traces, whereas the ρ_{xx} minimum still exists. The similarity is lost in this region. Except the region around $\nu = 1/2$, there is still the similarity [79, 80] between ρ_{xx} and $Bd\rho_{xy}/dB$ for the whole magnetic field even above 200 mK. The fundamental relation between R_{xx} and R_{xy} in the region close to $\nu = 1/2$ is an interesting subject for experimental as well as theoretical work.

As mentioned before, Khveshchenko gave a possible theory about the explanation of PMR of CFs around $\nu = 1/2$ [74]. The interaction between CFs introduces a logarithmic correction to ρ_{xy} apart from the point of $\nu = 1/2$. (The previous theory showed no interaction correction to ρ_{xy} around $\nu = 1/2$). It is the interaction correction to ρ_{xy} that leads to PMR around $\nu = 1/2$ for CFs. Their theory said the Hall slope would increase as $B > B(\nu = 1/2)$ and decrease as $B < B(\nu = 1/2)$, so this theory can explain the minium of first derivative of ρ_{xy} at $\nu = 1/2$. However, a discrepancy still exists concerning the temperature dependence. In the experimental data above 200 mK, the minimum of the first derivative of ρ_{xy} disappears, which means no correction to ρ_{xy}. However, the PMR of CFs still exists above 200 mK. In their theory, the minimum of first derivative of ρ_{xy} and PMR of CFs should exist together in the same temperature range. It appears the theory cannot explain the data at this point.

In conclusion, for EA467 with well width d = 35 nm at low temperature, ρ_{xx} exhibits a sharp, strongly temperature-dependent minimum centered at $\nu = 1/2$, while concomitant ρ_{xy} does not develop into quantized plateau and its slope in the vicinity of $\nu = 1/2$ shows sharp structure. These data deviate significantly from

the characteristic transport for single heterostructures. The Hall resistance close to $\nu = 1/2$ is not classical. This issue needs further theoretical understanding and experimental study.

CHAPTER 6

CONCLUSIONS

This thesis work consists of three parts: 1) Thermopower measurement in a low magnetic field ($B < 0.5$ T); 2) Thermopower measurement in a high field (Lowest Landau level regime); 3) Magnetoresistance measurement around one-half state. A TEP measurement technique has been developed in this thesis work. TEP of 2DEG has been measured successfully in a wide range of low temperatures (250 mK - 1 K) and magnetic fields (up to 45 T).

At zero magnetic field, the TEP of high-mobility 2DEG samples shows a power law temperature dependence (T^{3-4}), which indicates that the phonon-drag TEP is dominant at $T > 300$ mK and the diffusive TEP is negligible. Under this condition, TEP measurement can be applied to investigate the electron-phonon interaction directly because impurity scattering is not directly relevant.

In a weak magnetic field (higher LL regime), a new type of oscillation of TEP has been discovered in the high-mobility GaAs-AlGaAs 2DEG. This oscillation results from the inter-LL resonance of acoustic phonons carrying a momentum equal to twice the Fermi wave number at $B = 0$. Numerical calculations show that both 3D and 2D phonons can contribute to this effect. Our experimental data cannot determine which one has the dominant contribution to this low field oscillation.

The second part of thesis concerns thermopower in a high magnetic field (Lowest LL regime). Two anomalous peaks of TEP have been observed in a temperature range (1 K - 2 K) at $\nu = 2/3, 3/5$. These peaks evolve from the TEP minima of the incompressible quantum liquid states at $\nu = 2/3, 3/5$. The TEP at $\nu = 2/3, 3/5$ shows activation behavior in the temperature range of 250 mK - 1.6 K. Currently, there exists no specific theory that can explain these interesting observations.

The third part of the thesis focuses on magnetoresistance measurement around $\nu = 1/2$. In a quantum well (35 nm) sample, low temperature transport features of one-half state have been studied in ultrahigh magnetic field (up to 45 T). Comparing with heterojunction samples, ρ_{xx} in this QW sample exhibits a sharp, strongly temperature-dependent minimum centered at $\nu = 1/2$. The concomitant ρ_{xy} does not develop into quantized plateau, its slope in the vicinity of $\nu = 1/2$ shows a sharp structure. The first derivative of ρ_{xy} with respect to magnetic field shows a steep temperature-dependent minimum at $\nu = 1/2$. These data deviate significantly from the characteristic transport typical of single heterojunctions and are indicative of fluctuation of composite Fermion states at $\nu = 1/2$ in a 2DEG when the layer thickness far exceeds the magnetic length.

REFERENCES

[1] K. von Klitzing, G. Dorda, and M. Pepper, Phys. Rev. Lett. **45**, 494 (1980).

[2] D. C. Tsui, H. L. Stormer, and A. C. Gossard, Phys. Rev. Lett. **48**, 1559 (1982).

[3] R. B. Laughlin, Phys. Rev. Lett. **50**, 1395 (1983).

[4] R. L. Willet *et al.*, Phys. Rev. Lett. **59**, 1779 (1987).

[5] J. P. Eisenstein *et al.*, Phys. Rev. Lett. **68**, 1383 (1992).

[6] Y. W. Suen *et al.*, Phys. Rev. Lett. **68**, 1379 (1992); **69**, 3551 (1992); **72**, 3405 (1994).

[7] B. I. Halperin, Helv. Phys. Acta **56**, 75 (1983).

[8] E. H. Rezayi and F. D. M. Haldane, Bull. Am. Phys. Soc. **32**, 892 (1987).

[9] S. He *et al.*, Phys. Rev. B **43**, 9339 (1991).

[10] J. K. Jain, Phys. Rev. Lett. **63**, 199 (1989); Phys. Rev. B **40**, 8079 (1989); **41**,7653 (1990).

[11] B. I. Halperin, P. A. Lee, and N. Read, Phys. Rev. B **47**, 7312 (1993).

[12] V. Kalmeyer and S. -C. Zhang, Phys. Rev. B **46**, 9889 (1992).

[13] E. H. Rezayi and N. Read, Phys. Rev. Lett. **72**, 900 (1994).

[14] G. Moore and N. Read, Nucl. Phys. B **360**, 362 (1991).

[15] R. L. Willet *et al.*, Phys. Rev. Lett. **65**, 112 (1990).

[16] K. Park, Melik - Alaverdian, N. E. Bonesteel, and J. K. Jain, Phys. Rev. B **58**, R10167 (1998).

[17] John H. Davies, *The Physics of Low-Dimensional Semiconductors* (Cambridge University Press, Cambridge, 1998).

[18] G. Landwehr and E. I. Rashba, *Landau Level Spectroscopy* (Elsevier Science Publishers, North-Holland, 1991).

[19] Daijiro Yoshioka, *The Quantum Hall Effect* (Springer, New York, 2002).

[20] Steven M. Girvin, Cond-mat/9907002, 1, Jul, 1999.

[21] T. Chakraborty and P. Pietilainen, *The Quantum Hall Effects*, (Springer-Verlag, Berlin, 1995).

[22] S. Das Sarma and A. Pinczuk, *Perspectives in Quantum Hall Effects* (Wiley and Sons, New York, 1997).

[23] R. B. Laughlin, Phys. Rev. B **23**, 5632 (1981).

[24] B. I. Halperin, Phys. Rev. Lett. **52**, 1583 (1984).

[25] V. J. Goldman and B. Su, Science **267**, 1010 (1995).

[26] R. de-Picciotto *et al.*, Nature, **389**, 162 (1997).

[27] J. H. Smet, *et al.*, Phys. Rev. Lett. **77**, 2272 (1996).

[28] R. R. Du, H. L. Stormer, D. C. Tsui, L. N. Pfeiffer, and K. W. West, Phys. Rev. Lett. **70**, 2944 (1993).

[29] O. Heinonen, *Composite Fermions* (World Scientific, Singapore, 2002).

[30] W. Pan *et al.*, Phys. Rev. Lett. **83**, 3530 (1999).

[31] P. N. Butcher, Norman H. March, and Mario P. Tosi, *Physics of Low-Dimensional Semiconductor Structures* (Plenum Press, New York, 1993).

[32] M. J. Smith and P. N. Butcher, J. Phys.: Condens. Matter. **2**, 2375 (1990).

[33] D. G. Cantrell and P. N. Butcher, J. Phys. C. **20**, 1985 (1987).

[34] B. Tieke, R. Fletcher, U. Zeitler, M. Henini, and J. C. Maan, Phys. Rev. B **58**, 2017 (1998).

[35] S. K. Lyo, Phys. Rev. B **38**, 6345 (1988).

[36] S. S. Kubakaddi, P. N. Butcher, and B. G. Mulimani, Phys. Rev. B **40**, 1377 (1989).

[37] S. K. Lyo, Phys. Rev. B **40**, 6458 (1989).

[38] H. Obloh, K. von Klitzing, and K. Ploog, Surf. Sci. **142**, 234 (1984).

[39] J. S. Davidson, E. D. Dahlberg, A. J. Valois and G. Y. Robinson, Phys. Rev. B **33**, 2941 (1986).

[40] R. Fletcher, J. C. Maan, and G. Weimann, Phys. Rev. B **32**, 8477 (1985).

[41] R. Fletcher, J. C. Maan, K. Ploog and G. Weimann, Phys. Rev. B **33**, 7122 (1986).

[42] R. Fletcher, M. D'Iorio, A. S. Sachrajda, R. Stoner, C. T. Foxon, and J. J. Harris, Phys. Rev. B **37**, 3137 (1988).

[43] R. J. Nicholas, J. Phys. C : Solid State Phys. **18**, L695 (1985).

[44] X. Ying, V. Bayot, M. B. Santos and M. Shayegan, Phys. Rev. B **50**, 4969 (1994).

[45] V. Bayot, E. Grivei, H. C. Manoharan, X. Ying, and M. Shayegan, Phys. Rev. B **52**, R8621 (1995).

[46] B. Tieke, U. Zeitler, R. Fletcher, S. A. J. Wiegers, A. K. Geim, J. C. Maan, and M. Henini, Phys. Rev. Lett. **76**, 3630 (1996).

[47] C. Ruf, H. Obloh, B. Junge, E. Gmelin, K. Ploog, and G. Weimann, Phys. Rev. B **37**, 6377 (1988).

[48] U. Zeitler, R. Fletcher, J. C. Maan, C. T. Foxon, J. J. Harris, and P. Wyder, Surf. Sci., **305**, 91 (1994).

[49] Frank Pobell, *Matter and Methods at Low Temperature* (Springer, Berlin, 1996).

[50] Stycast 1266 A/B, Emerson and Cuming Inc., Lexington, MA.

[51] Ruthenium oxide sensor, Lakeshore Cryotronics, Inc., Westerville, OH.

[52] Stycast 2850FT, Emerson and Cuming Inc., Lexington, MA.

[53] Strain gauge, Hottinger Baldin Measurement, Inc., Marlboro, MA.

[54] Silver paint, Structure Probe, Inc., Westchester, PA.

[55] M. A. Zudov, I. V. Ponomarev, A. L. Efros, R. R. Du, J. A. Simmons, and J. L. Reno, Phys. Rev. Lett. **86**, 3614 (2001).

[56] T. Ando, A. B. Fowler, and F. Stern, Rev. Mod. Phys. **54**, 437 (1982).

[57] H. Scher and T. Holstein, Phys. Rev. **148**, 598 (1966).

[58] I. V. Ponomarev and A. L. Efros, Phys. Rev. B **63**, 165305 (2001).

[59] U. Zeitler, J. C. Maan, P. Wyder, R. Fletcher, C. T. Foxon, and J. J. Harris, Phys. Rev. B **47**, 16008 (1993).

[60] D. V. Khveshchenko and M. Yu. Reizer, Phys. Rev. Lett. **78**, 3531 (1997).

[61] M. Tsaousidou, P. N. Butcher, and S. S. Kubakaddi, Phys. Rev. Lett. **83**, 4820 (1999).

[62] R. R. Du, H. L. Stormer, D. C. Tsui, A. S. Yeh, L. N. Pfeiffer, and K. W. West, Phys. Rev. Lett. **73**, 3274 (1994).

[63] C. J. Mellor *et al.*, Phys. Rev. Lett. **74**, 2339 (1995).

[64] W. Pan, H. L. Stormer, D. C. Tsui, L. N. Pfeiffer, K. W. Baldwin, and K. W. West, Phys. Rev. Lett. **90**, 016801-1 (2003).

[65] F. D. M. Haldane, Phys. Rev. Lett. **51**, 605 (1983).

[66] F. D. M. Haldane and E. H. Rezayi, Phys. Rev. Lett. **54**, 237 (1985).

[67] R. E. Prange and S. M. Girvin, *The Quantum Hall Effect* (Springer-Verlag, Berlin, 1987).

[68] H. W. Jiang, H. L. Stormer, D. C. Tsui, L. N. Pfeiffer, and K. W. West, Phys. Rev. B **40**, 12013 (1989).

[69] L. P. Rokhinson, B. Su, and V. J. Goldman, Phys. Rev. B **52**, R11588 (1995).

[70] B. L. Altshuler, A. G. Aronov, and P. A. Lee, Phys. Rev. Lett. **44**, 1288 (1980).

[71] P. A. Lee and T. V. Ramakrishnan, Rev. Mod. Phys. **57**, 287 (1985).

[72] M. A. Paalanen, D. C. Tsui, and J. C. M. Huang, Phys. Rev. Lett. **51**, 2226 (1983).

[73] K. K. Choi, D. C. Tsui, and S. C. Palmateer, Phys. Rev. B **32**, 5540 (1985).

[74] D. V. Khveshchenko, Phys. Rev. B **55**, 13817 (1997).

[75] L. P. Rokhinson and V. J. Goldman, Phys. Rev. B **56**, R1672 (1997).

[76] F. Evers, A. D. Mirlin, D. G. Polyakov and P. Wlfe, Phys. Rev. B **60**, 8951 (1999);A.D. Mirlin *et al.*, Phys. Rev. Lett. **83**, 2801 (1999).

[77] C. -T. Liang *et al.*, Solid State Commun. **102**,327 (1997).

[78] W. Pan *et al.*, Solid State Commun. **119**,641 (2001).

[79] A. M. Chang and D. C. Tsui, Solid State Commun. **56**, 153 (1983).

[80] H. L. Stormer, K. W. Baldwin, L. N. Pfeiffer, and K. W. West, Solid state Commun. **84**, 95 (1992).

[81] T. Sajoto *et al.*, Phys. Rev. B **41**, 8449 (1990).

[82] S. H. Simon and B. I. Halperin, Phys. Rev. Lett. **73**, 3278 (1994).